

Spatially Distributed Wind Measurements in the Atmospheric Boundary Layer with a Fleet of Quadrotors

Examination of the Homogeneity Assumption and
the Applicability of Taylor's Hypothesis

MASTER'S THESIS

in Atmospheric Sciences

Submitted to the
FACULTY OF GEO- AND ATMOSPHERIC SCIENCES
of the
UNIVERSITY OF INNSBRUCK

in Partial Fulfillment of the Requirements for the Degree of
MASTER OF SCIENCE

by
JOSEF ZINK

Advisor
Manuela Lehner, PhD

Innsbruck, January 2022

Abstract

Spatially distributed wind measurements were conducted in the atmospheric boundary layer with a fleet of quadrotor UAVs (Unmanned Aerial Vehicle) at the Grenzschichtmessfeld (GM) Falkenberg during the FESSTVaL (Field Experiment on Sub-Mesoscale Spatio-Temporal Variability in Lindenberg) campaign in summer 2021. The big advantage of deploying the UAV fleet is the possibility to record the wind field at different spatial points simultaneously with a high temporal resolution.

A particular flight pattern was performed to calibrate the UAV wind measures using reference data of the 99 m mast at GM Falkenberg. The results show that not only the mean wind but also the turbulence can be reasonably resolved up to 1 Hz.

In a second pattern, ten UAVs were placed in a horizontal plane in both the streamwise and lateral directions of the flow. To align the pattern along the wind direction, easily adaptable flight plans were created and the last available wind measurements of the mast were used for the orientation.

Varying spatial distances between neighbouring UAVs in this horizontal measurement pattern allow turbulence analyses as a function of distance. In this work, the spatially distributed measurements are used to examine the homogeneity assumption and Taylor's hypothesis in atmospheric boundary layer flows. The measurement strategy was repeated for a near neutral, a convective and a stable atmospheric boundary layer to identify possible dependencies of these assumptions on different atmospheric conditions.

Considering the measurement accuracy of the UAVs, the results show no significant violation of the homogeneity assumption within the microscale with a maximum separation distance of 205 m. Calculated cross-correlations and coherences between pairs of UAVs aligned in streamwise direction reveal a decrease with distance, however. This indicates that Taylor's frozen turbulence hypothesis is not unrestrictedly valid for all scales. The strongest decrease with distance is observed for the stably stratified case, followed by the unstably one. The lowest decrease is found for the near neutral stratification. The measurement accuracies of the UAVs and a slight misalignment of the measurement pattern with the actual prevailing wind direction during the flight have to be considered, however, which are partly responsible for the decline.

For the investigated separation distances from 5 m to 205 m, the achieved measurement duration of about 14 min is sufficient for the analyses of cross-correlations and coherences. This duration is determined by the battery runtime. However, the potential to resolve larger scales has already been demonstrated in the field by replacing the UAVs with charged ones during the flight.

Contents

Abstract	i
Contents	iii
1 Introduction	1
2 Turbulence in the Atmospheric Boundary Layer	4
2.1 Idealized Atmospheric Boundary Layer over Homogeneous, Flat Terrain	4
2.2 Ensemble Average and Ergodicity	7
2.3 Energy Cascade and Kolmogorov Hypotheses	8
2.4 Taylor Hypothesis	9
3 Data and Methods	13
3.1 UAV Fleet	13
3.1.1 System Description	13
3.1.2 Fleet Communication	13
3.2 Wind Algorithm	15
3.3 Field Campaign and Reference Instrumentation	17
3.4 Flight Patterns	19
3.5 Data Processing	21
3.5.1 Interpolation, Filtering and Coordinate Rotation	21
3.5.2 (Co-)variances and Spectra	22
3.5.3 Stationarity and Homogeneity Tests	23
3.5.4 Treatment of Pattern Misalignment	24
3.5.5 Data for Atmospheric Conditions	25
4 Results	26
4.1 Calibration Results	26
4.2 Near Neutral Boundary Layer	30
4.2.1 Atmospheric Conditions	30
4.2.2 Spatially Distributed Measurements in the Horizontal Pattern	33
4.2.3 Power Spectra	36

4.2.4	Cross-correlation and Coherence	37
4.3	Convective Boundary Layer	42
4.3.1	Atmospheric Conditions	42
4.3.2	Spatially Distributed Measurements in the Horizontal Pattern	43
4.3.3	Power Spectra	44
4.3.4	Cross-correlation and Coherence	45
4.4	Stable Boundary Layer	46
4.4.1	Atmospheric Conditions	46
4.4.2	Spatially Distributed Measurements in the Horizontal Pattern	47
4.4.3	Power Spectra	49
4.4.4	Cross-correlation and Coherence	50
5	Discussion	51
5.1	Applicability of UAV Measurements for Studying Turbulence in the Atmospheric Boundary Layer	51
5.2	Determining Correlation and Coherence with the Horizontal Pattern .	52
5.3	Spatial Correlation and Coherence for Different Atmospheric Conditions	53
5.4	Homogeneity in the Microscale	56
6	Conclusions and Outlook	59
A	Near Neutral	61
B	Convective	62
C	Stable	70
	Bibliography	78
	Acknowledgments	83

Chapter 1

Introduction

In general, high Reynolds number flows can be described mathematically by the deterministic Navier-Stokes equations and thus, in theory, the evolution of a system could be predicted exactly. However, such flows have a high sensitivity to initial and boundary conditions ([Pope 2000](#)). This means that experiments with the same nominal conditions but with tiny perturbations can lead to a very distinct evolution known as the deterministic chaotic nature of turbulent flows. Therefore, a general approach is to treat turbulent flows as random fields and describe them statistically. Thereby, one is interested in ensemble averages defined as the mean over all possible realizations of the turbulent flow under the same nominal conditions ([Wyngaard 2009](#)). Clearly, this requires a high or even infinite number of repetitions of the same experiment, which is already challenging in laboratory environments but impossible in the atmosphere since exact identical weather events do not exist in nature.

This issue is commonly treated with the ergodic hypothesis, which states that for stationary and homogeneous conditions, a temporal and a spatial mean converges towards the ensemble mean, respectively ([Wyngaard 2009](#)). Measurements in the atmospheric boundary layer are often based on single instruments like a sonic anemometer at a fixed point. Under the assumption of the ergodic hypothesis, measured temporal averages are then interpreted as ensemble averages and with the premise of homogeneity also as spatial averages. However, turbulence is never really stationary and even more critical is the assumption of homogeneity since such conditions are never really met in natural environments. Therefore, further assumptions like quasi-stationarity ([Foken and Wichura 1996](#)) and local homogeneity ([Pope 2000](#)) are made frequently. It is questionable whether these assumptions are always appropriate and if a temporal average at a single measurement point is representative for the upstream spatial region in heterogeneous or complex terrain.

The absence of ergodicity can lead to systematic errors when calculating turbulent fluxes with the eddy covariance method using a single instrument: If temporal and spatial mean values are not equal, so-called dispersive fluxes arise as an ad-

ditional term in the covariances (Margairaz et al. 2020), which cannot be resolved with a single instrument. Neglecting these dispersive fluxes, which can be caused by organised convective cells in the convective boundary layer, may be the main reason for systematic underestimation of fluxes (Mauder et al. 2020).

The Taylor hypothesis (Taylor 1938; Stull 1988) is a second commonly used hypothesis for studying spatial structures of turbulent eddies with a single measurement device. It states that the turbulence can be assumed to be frozen and advected by the mean wind. Hence, one can convert a time difference into a spatial distance. The hypothesis has been studied theoretically (Lumley 1965; Wyngaard and Clifford 1977), with simulations (Horst et al. 2004; Dosio et al. 2005; Bahraminasab et al. 2008) and there have been experiments conducted with lidar measurements (Schlipf et al. 2011; Higgins et al. 2012) to test the hypothesis. Still, concerning its numerous use in atmospheric boundary layer research, it is worth doing further investigations on this subject.

Spatially distributed wind measurements have been performed during the HATS field campaign (Horst et al. 2004) with crosswind arrays of sonic anemometers to investigate spatially filtered and unfiltered turbulence as an experimental analogy to large-eddy-simulations (LES). Such an experiment with many sonic anemometers is logistically demanding and therefore tricky to repeat routinely. Moreover, it is hard to measure up to high altitudes or in complex terrain straightforwardly.

Remote sensing instruments (Radar, Sodar, Lidar) provide somewhat more flexibility since they can measure wind at multiple distances along the line-of-sight (LOS) up to several kilometres using the doppler shift between the transmitted and received signals. Lidar measurements in staring mode (e.g., O'Connor et al. 2010) have the disadvantage that they can only measure the wind component in the line-of-sight direction. Therefore, often scanning methods like velocity-azimuth-display (VAD) scans (e.g., Smalikho and Banakh 2017), range-height-indicator (RHI) scans (e.g., Wildmann et al. 2019) or plan-position-indicator (PPI) scans (e.g., Krishnamurthy et al. 2011) are applied. However, such methods introduce time lags between different scanning directions, and thus, the atmosphere is not explored simultaneously. Three-dimensional wind vectors can also be obtained by using at least three linear, independent lidar beams intersecting at the measurement point (Wildmann et al. 2018). But with this approach, the 3D wind is only measured at a single location and the repetition for different ones again is only possible with time delays.

The use of UAVs (Unmanned Aerial Vehicle) offers an easy and flexible method for atmospheric measurements. Thermodynamic quantities and turbulent wind fields have been recorded both with fixed-wing vehicles (Wildmann et al. 2015; Kral et al. 2021) and multicopters. The latter are easier to operate because of their possibility to start and land vertically. Wind measurements with multicopters have been

performed with attached external sensors like sonic anemometers (Nolan et al. 2018; Shimura et al. 2018; Thielicke et al. 2020; Reuter et al. 2020) or hot wire/element probes (Cuxart et al. 2019; Molter and Cheng 2020). A second method is the use of only onboard sensors (Palomaki et al. 2017; Brosy et al. 2017; Wang et al. 2018; Bell et al. 2020) from which the wind is retrieved by an appropriate algorithm.

Although a single UAV can fly to many measurement points sequentially, it is impossible to measure at different locations simultaneously. Therefore, Wetz et al. (2021) used a fleet of ten quadrotor UAVs for wind measurements at spatially distributed points within the project SWUF-3D (Simultaneous Wind measurement with Unmanned Flight Systems in 3D swarms). They found reasonable results for both horizontal wind speed and direction using a simple, but robust wind retrieving algorithm. Due to this success, they extended the UAV fleet by 25 new quadrotors. Further steps in this project are the extension of the wind algorithm and in addition to the calculation of mean variables, also the investigation of turbulence quantities. The master thesis is embedded in this project, and tries to answer the following questions:

- (1) How well can the mean horizontal wind be measured by the UAVs using an advanced algorithm?
- (2) How well can the UAVs capture turbulence? Which scales can they resolve and what is the dependency on atmospheric conditions?
- (3) What advantage brings the possibility to measure the wind at different spatial points simultaneously with the accuracy answered in (1) and (2)? Can significant conclusions be drawn about the homogeneity assumption, and what can be said about the applicability of the Taylor hypothesis?

After this introduction, the thesis starts with a short theoretical part about turbulence in the atmospheric boundary layer (chap. 2): It introduces the idealized atmospheric boundary layer, the ergodic hypothesis, the energy cascade theory and the Taylor hypothesis. Chapter 3 describes the UAV fleet, the wind algorithm, the field campaign, the performed flight patterns and the data processing. After the presentation of the calibration performance, three case studies are provided in chapter 4. The findings of chapter 4 are discussed in more detail in chapter 5. The thesis ends with the statement of the main conclusions and an outlook (chap. 6).

Chapter 2

Turbulence in the Atmospheric Boundary Layer

2.1 Idealized Atmospheric Boundary Layer over Homogeneous, Flat Terrain

The atmospheric boundary layer (ABL) is the lowest part of the atmosphere which is directly influenced by the earth's surface ([Stull 1988](#)). In this region, atmospheric motions are affected by surface friction and energy exchange with the surface, resulting in strong vertical gradients in wind speed and temperature. These processes lead to instabilities making the flow turbulent. Turbulence is responsible for the effective exchange of momentum, energy, moisture and other trace constituents between the surface and ABL, mixing within the ABL and entrainment of free tropospheric air into the ABL ([Markowski and Richardson 2010](#)).

While mechanically induced turbulence caused by surface friction and corresponding wind shear is always a source of turbulence, thermally induced buoyancy effects can be an amplifying or a dampening factor. Dependent on the sign of the surface sensible heat flux, cooling or warming of the adjacent air occurs influencing the (static) stability. A common measure for this static stability is the vertical gradient of potential temperature Θ . This potential temperature is given through ([Stull 1988](#))

$$\Theta = T \left(\frac{p_0}{p} \right)^{R/c_p} \quad (2.1)$$

with the temperature T , the pressure p , the standard reference pressure $p_0 = 1000 \text{ hPa}$, the gas constant of dry air R and the specific heat at constant pressure c_p . The potential temperature Θ is the temperature an air parcel would attain if it is adiabatically brought from pressure p to standard reference pressure p_0 . For adiabatic motions, Θ is a conserved quantity. In unstably stratified air, the mean

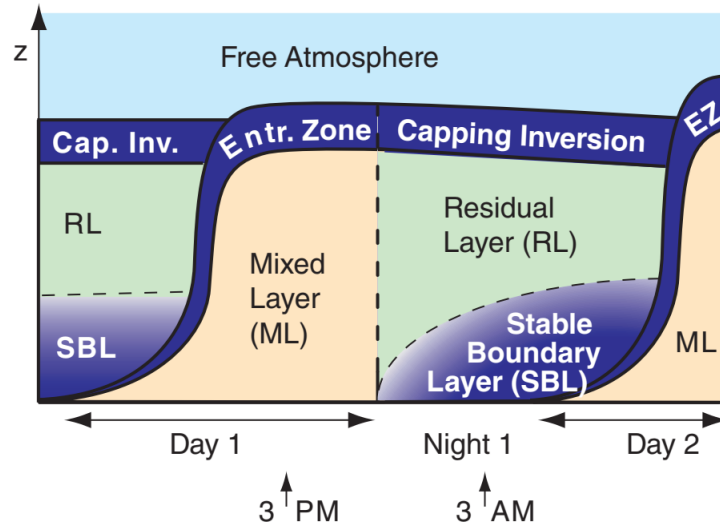


Figure 2.1: Daily evolution of the ABL during fair weather conditions. Tan means nonlocally statically unstable air, light green indicates neutral stratification and darker blues means stronger static stability. Taken from [Stull \(2017\)](#).

vertical potential temperature decreases with height ($d\bar{\Theta}/dz < 0$), in stably stratified air it increases with height ($d\bar{\Theta}/dz > 0$) and for neutral conditions it is constant ($d\bar{\Theta}/dz = 0$) ([Stull 2017](#)).

Because of the diurnal cycle of the net radiation balance, the static stability and thus the structure and depth of the ABL have a daily evolution. Figure 2.1 shows an idealised diurnal evolution of the ABL over homogeneous, flat terrain for fair weather situations associated with anticyclonic conditions: The development of the convective boundary layer (CBL) starts after sunrise, when the net radiation balance becomes positive and the ground starts to heat up leading to a positive sensible heat flux. This upward flux warms the ambient air and buoyancy effects lead to vertical mixing (thermally induced turbulence). In the fully developed CBL, the potential temperature decreases strongly near the surface (Fig. 2.2a). This lowest layer (approx. 10% of the CBL) is called the surface layer (SL) and is characterized through nearly constant fluxes with height ([Stull 2017](#)). Above the surface layer, the mechanically and thermally induced turbulence leads to strong vertical mixing resulting in the mixed layer (ML). In this layer, which covers around 80% of the CBL, mean profiles are approximately constant with height (Fig. 2.2a). The mixed layer is topped by the entrainment zone (EZ) often characterized by a strong inversion. Here, mixing with potentially warm air from the free atmosphere (FA) may occur due to overshooting turbulent thermals. Due to this entrainment, the mixing layer grows in height and further the CBL is warmed from above. If the lifting condensation level is reached for some ascending thermals, the CBL is topped by fair weather cumulus clouds. Typical boundary layer heights are 1–2 km during daytime.

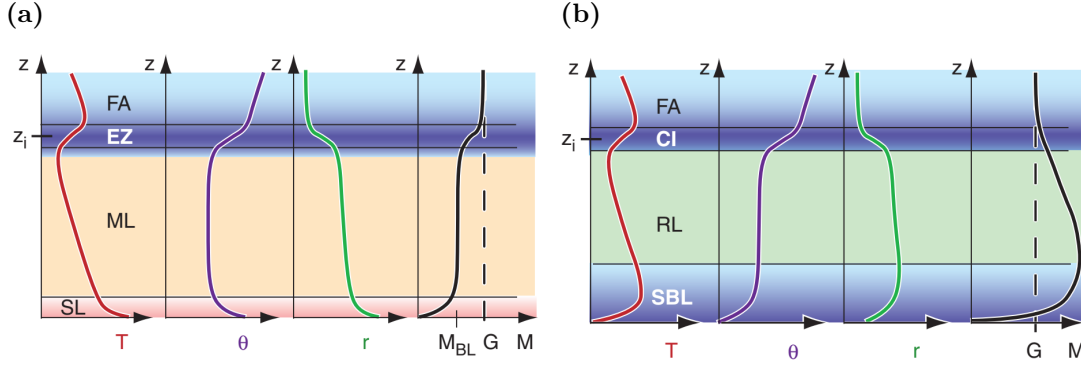


Figure 2.2: Idealized mean vertical profiles of temperature T , potential temperature Θ , mixing ratio r and wind speed M for (a) day-time and (b) night-time ABL. The dashed line G indicates geostrophic wind and M_{BL} is the average wind speed in the atmospheric boundary layer. Tan indicates statically unstable air, green means neutral stratification and blue is statically stable air, where darker blue indicate higher stability. Taken from [Stull \(2017\)](#).

Slightly before sunset the surface net radiation balance becomes negative and thermals stop to form. Consequently turbulence intensity decays in the well-mixed layer, but the layer remains neutrally stratified, called the residual layer (RL) (Fig. 2.2b). Below the residual layer a stably stratified boundary layer (SBL) starts to grow from the bottom. The stably stratified air near the surface suppresses thermally induced turbulence and only shear in the mean wind induced by surface friction (mechanically induced turbulence) tends to generate turbulence. Hence, turbulence in the SBL is in general weaker and more sporadic ([Stull 1988](#)). As a consequence less mixing occurs, especially for weak wind conditions. Therefore effective turbulent mixing is mainly confined to the surface layer (SL) and upper portions of the boundary layer are basically decoupled from the surface. This decoupling process may lead to supergeostrophic wind speeds aloft the SL (Fig. 2.2b) due to inertial forces, a so-called low level jet ([Markowski and Richardson 2010](#)). Typical heights of the SBL are 100–200 m.

In some cases, where less surface cooling or warming occurs and strong winds prevail, a (near) neutral boundary layer can form with almost constant potential temperature with height ([Stull 2017](#)). In the idealized case of a neutrally stratified boundary layer, the wind profile takes the logarithmic form ([Stull 2017](#))

$$u(z) = \frac{u_*}{\kappa} \ln \left(\frac{z}{z_0} \right) \quad (2.2)$$

with the height above ground level (AGL) z , the friction velocity u_* , the von Kármán constant $\kappa \approx 0.4$ and the roughness length z_0 .

2.2 Ensemble Average and Ergodicity

As outlined in chapter 1, the chaotic nature of turbulent flows demands a statistical treatment. Reynolds (1895) first had the idea to separate the flow into a mean and fluctuating part. Accordingly, a space and time dependent turbulent flow variable $a(\mathbf{x}, t)$ can be decomposed

$$a(\mathbf{x}, t) = \langle a(\mathbf{x}, t) \rangle + a'(\mathbf{x}, t) , \quad (2.3)$$

where $\langle a(\mathbf{x}, t) \rangle$ is the ensemble average and $a'(\mathbf{x}, t)$ its fluctuating part.

The ensemble average of a turbulent quantity $a(\mathbf{x}, t)$ is defined as the expected value over all possible realizations of the turbulent flow under the same nominal conditions, mathematically expressed through (Wyngaard 2009)

$$\langle a(\mathbf{x}, t) \rangle := A^E(\mathbf{x}, t) := \lim_{N \rightarrow \infty} \frac{1}{N} \sum_{\alpha=1}^{\alpha=N} a(\mathbf{x}, t; \alpha) . \quad (2.4)$$

Here, α denotes the realization number. Equation (2.4) implies that the ensemble average is in general a function of both space and time.

Clearly, it is impossible to determine the ensemble average with equation (2.4) in real flow scenarios within the atmospheric boundary layer, as no repetition of an experiment is possible under exactly the same conditions. Instead one can measure the time average at position \mathbf{x} over a period T for a single realization n via

$$\overline{a(\mathbf{x}, t)} := A^T(\mathbf{x}, t, T; n) := \frac{1}{T} \int_0^T a(\mathbf{x}, t + t'; n) dt' \quad (2.5)$$

or (theoretical) a horizontal spatial average over an area S for a specific time t and realization m with

$$[a(\mathbf{x}, t)] := A^S(\mathbf{x}, t, S; m) := \frac{1}{S} \iint_S a(\mathbf{x} + \mathbf{x}', t; m) dS . \quad (2.6)$$

For a stationary process, which means that the turbulence statistics are independent of absolute time t , the ensemble average is only a function of space ($A^E = A^E(\mathbf{x})$). Furthermore, one expects that the entire turbulence information is contained in the time series as the averaging time T increases. Hence, the time average over the single realization n should converge towards the ensemble mean, i.e.,

$$\lim_{T \rightarrow \infty} A^T(\mathbf{x}, t, T; n) = A^E(\mathbf{x}) . \quad (2.7)$$

Further, for homogeneous conditions, which means that the turbulence statistics are independent of space, the ensemble average is only a function of time ($A^E = A^E(t)$) and with increasing horizontal area S one expects that the spatial average for a single realization m converges towards the ensemble mean, i.e.,

$$\lim_{S \rightarrow \infty} A^S(\mathbf{x}, t, S; m) = A^E(t) . \quad (2.8)$$

Thus, equations (2.7) and (2.8) imply that for both stationary and homogeneous conditions, the time average and the spatial average converge towards the space and time independent ensemble mean. The equivalence of time, space and ensemble averages under the specified conditions is called ergodicity (Wyngaard 2009).

In the subsequent sections, a time average indicated by " $\bar{}$ " is treated as ensemble average in the sense of equation (2.7) and " \prime " indicates its fluctuating part.

2.3 Energy Cascade and Kolmogorov Hypotheses

One basic concept in turbulence theory is to describe turbulent flows as a composition of eddies with different sizes (Stull 1988). Each of these eddies is characterized by a wavelength λ and corresponding wavenumber $k = 2\pi/\lambda$. Hence, turbulent signals can be written as Fourier decompositions. Corresponding (co-)spectra provide information on how much eddies of a certain size contribute to the total (co-)variance of the turbulence variable (e.g., Lumley and Panofsky 1964).

Richardson (1922) introduced the idea of the energy cascade: Most of the turbulent kinetic energy is contained in large eddies, which are created by instabilities of the mean flow. These eddies are again affected by instabilities and therefore they break up. This process continues and so the energy is successively transferred to smaller and smaller scales. That energy cascade ends with the dissipation of turbulent kinetic energy into heat by viscous forces.

This picture of the energy cascade leads to an idealized energy spectrum (Fig. 2.3), which can be separated into three regions: Energy input from the mean flow occurs in the energy containing range. Eddies in this range are highly anisotropic and are affected by the boundary conditions of the flow. Therefore, the magnitude of the spectral density depends on external parameters.

The second region in the spectrum is called the inertial subrange. In this region, the turbulent kinetic energy is neither generated nor dissipated, but only transported through. Kolmogorov (1941b) claimed the existence of the inertial subrange by the hypothesis that there has to be a range in the spectrum, where the turbulence is locally isotropic. Here, the term "local" refers to the specific range in the spectrum and the term "isotropic", which means directional independence, has to be considered statistically. A direct consequence of this hypothesis is that the spectral density can neither depend on external parameters nor on the molecular viscosity. Hence, the spectral density is only a function of wavenumber k and dissipation rate ϵ . Although dissipation is no important process in the inertial subrange, the dissipation rate ϵ has to be considered as a variable since it determines at which rate the energy finally dissipates and therefore also characterises the cascade through the inertial

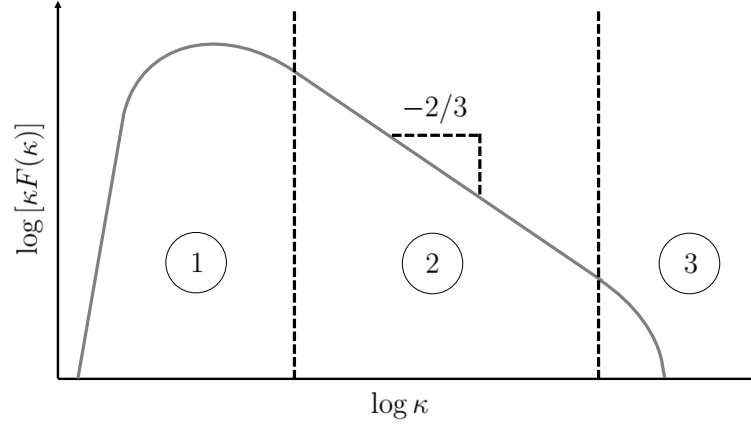


Figure 2.3: Idealized energy spectrum with ① energy containing range, ② inertial sub-range and ③ dissipation range. Note the logarithmic axes scales.

subrange. Dimensional analysis leads to the spectral density (Pope 2000)

$$F(k) = \alpha \epsilon^{2/3} k^{-5/3} \quad (2.9)$$

with the Kolmogorov constant α .

Finally the turbulent kinetic energy is dissipated into heat in the dissipation range. Kolmogorov's theory suggests that in this range only the dissipation rate ϵ and viscosity ν determine the spectral density. From this hypothesis and dimensional analysis Kolmogorov time scale, micro scale and velocity scale can be obtained (Pope 2000) characterising the dissipation range.

2.4 Taylor Hypothesis

As already stated in chapter 1, it is often of interest to have information on the eddies' size and spatial structure of turbulence. However, it is nearly impossible to have multiple instruments employed in the field to generate a snapshot picture of the ABL. Instead, spatial information is often retrieved from a single time series with the help of Taylor's frozen turbulence hypothesis. It states, that the turbulence can be assumed to be frozen when it passes the sensor and the unchanged pattern is solely advected by the mean wind (Taylor 1938; Stull 1988).

Thus -formulated in 1D- a time difference Δt can be converted to a spatial distance Δx with

$$\Delta x = \bar{u} \Delta t, \quad (2.10)$$

where \bar{u} denotes the mean wind speed in streamwise direction.

Further, when the turbulent field is treated as a composition of eddies, a measured frequency f can be converted to an eddie's size λ via

$$\lambda = \frac{\bar{u}}{f} . \quad (2.11)$$

Of course, turbulence is not really frozen, and thus the hypothesis is only applicable when the time scale of the evolution of turbulent eddies is longer than it takes to pass the sensor (Stull 1988). In practice, the applicability of the hypothesis is routinely estimated with a simple rule-of-thumb relating the standard deviation $\sigma_u = \sqrt{u'^2}$ as a measure of the activity of turbulence and the mean advection velocity \bar{u} . The ratio σ_u/\bar{u} is known as turbulence intensity. The hypothesis is said to be valid, whenever (Willis and Deardorff 1976)

$$\frac{\sigma_u}{\bar{u}} < 0.5 . \quad (2.12)$$

A more general test for the applicability of the hypothesis can be achieved, when more than one measurement device is available. For that, we start with the covariance function of a turbulent variable a for two time series measured at points separated by a longitudinal distance Δx . For abbreviation, the notation $a := a(x, t)$ and $a_{\Delta x} := a(x - \Delta x, t)$ is used. That covariance function has the form (Lumley and Panofsky 1964)

$$R_{aa_{\Delta x}}(\tau) = \overline{a'(t)a'_{\Delta x}(t - \tau)} , \quad (2.13)$$

where τ denotes the time lag. Normalization of the covariance function by the standard deviations leads to the cross-correlation function

$$\rho_{aa_{\Delta x}}(\tau) = \frac{R_{aa_{\Delta x}}(\tau)}{\sqrt{\overline{a'^2(t)}}\sqrt{\overline{a'^2_{\Delta x}(t - \tau)}}} = \frac{\overline{a'(t)a'_{\Delta x}(t - \tau)}}{\sqrt{\overline{a'^2(t)}}\sqrt{\overline{a'^2_{\Delta x}(t - \tau)}}} \quad (2.14)$$

taking values in the interval $[-1:1]$. In an ideal case, where Taylor's frozen turbulence hypothesis is perfectly valid, equation (2.14) would be one whenever $\Delta x/\tau = \bar{u}$. This is illustrated in Figure 2.4 for a simple theoretical signal of the form

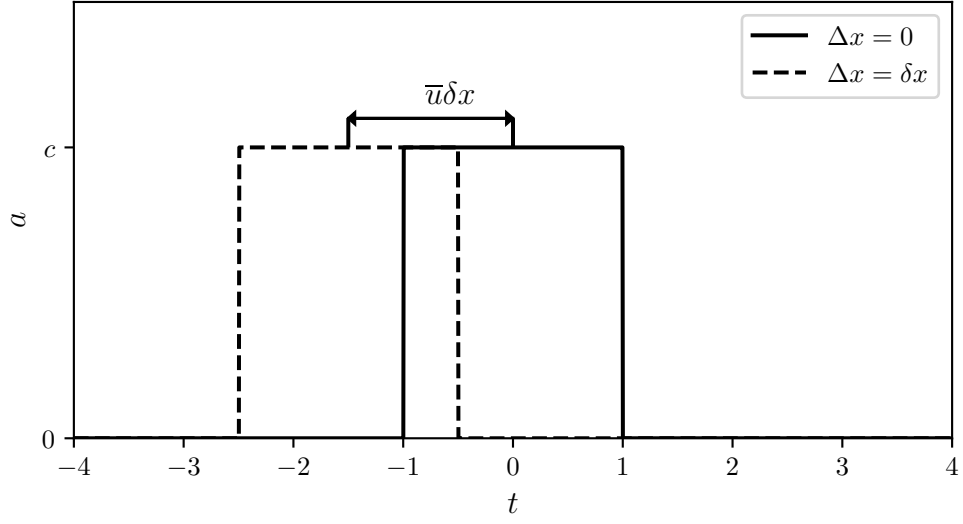
$$a(t) = \begin{cases} c, & \text{if } -1 < t < 1 \\ 0, & \text{else} \end{cases} \quad (2.15)$$

measured by a sensor at position x . The same pattern previously passed an upstream sensor at position $x - \delta x$ with a time shift of $\bar{u}\delta x$.

The cross-correlation $\rho_{aa_{\Delta x}}(\Delta x = \delta x, \tau)$ has the same shape as the autocorrelation function $\rho_{aa_{\Delta x}}(\Delta x = 0, \tau)$, but is shifted by $\bar{u}\delta x$.

Note, that $\rho_{aa_{\Delta x}}(\Delta x = \delta x, \tau = 0) = \rho_{aa_{\Delta x}}(\Delta x = 0, \tau = \bar{u}\delta x)$. This fact is often used to calculate turbulent length scales from the autocorrelation function under the assumptions of Taylor's frozen turbulence hypothesis.

(a)



(b)

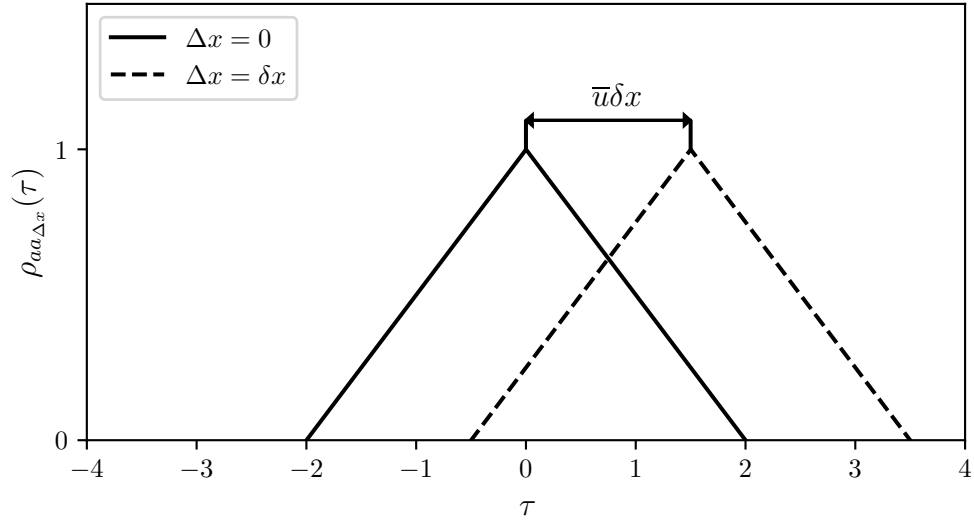


Figure 2.4: (a) Theoretical signal as function of time t for two sensors separated by a distance δx . The frozen signal is advected by the mean wind \bar{u} . (b) Corresponding cross-correlation functions $\rho_{aa\Delta x}$ as function of time lag τ .

Testing the validity of the Taylor hypothesis dependent on the eddies' scales can be achieved in terms of spectral analysis when calculating the Fourier transform of the cross-covariance function leading to the cross spectral density ([Lumley and Panofsky 1964](#))

$$S_{aa_{\Delta x}}(f) = \int_{-\infty}^{+\infty} R_{aa_{\Delta x}}(\tau) e^{-i2\pi f\tau} d\tau . \quad (2.16)$$

The cross spectral density is in general complex valued and can be decomposed into real and imaginary part

$$S_{aa_{\Delta x}}(f) = Co_{aa_{\Delta x}}(f) - iQ_{aa_{\Delta x}}(f) \quad (2.17)$$

with the so called cospectrum $Co_{aa_{\Delta x}}(f)$ and quadrature spectrum $Q_{aa_{\Delta x}}(f)$. From that, one can calculate the coherence

$$\gamma_{aa_{\Delta x}}^2(f) = \frac{|S_{aa_{\Delta x}}(f)|^2}{S_{aa}(f)S_{aa_{\Delta x}}(f)} , \quad (2.18)$$

which is the square of the absolute value of the cross spectral density normalized by the power spectral densities of the two time series. The form of equation (2.18) resembles a frequency-dependent squared correlation coefficient and thus the coherence $\gamma_{aa_{\Delta x}}^2(f)$ can take values between zero and one. It takes the value one, whenever the Fourier components at the frequency f of the two timeseries have proportional amplitudes throughout the ensemble ([Lumley and Panofsky 1964](#)). Thus, if the Taylor hypothesis is perfectly valid for all scales, the coherence should be one for all frequencies.

Chapter 3

Data and Methods

3.1 UAV Fleet

3.1.1 System Description

The UAV fleet consists of 34 Holybro QAV250 quadrotors. Figure 3.1 shows a labelled image of such a UAV and Table 3.1 provides more detailed information on the hardware and the sensors. Each quadrotor has a labelling between 2 and 35.

The individual UAVs contain the Pixhawk[®] 4 Mini flight controller with an integrated Internal Measurement Unit (IMU) consisting of gyroscope, accelerometer, magnetometer, barometer and a GNSS system. The PX4 software processes the measured sensor data. Since these are noisy, the software includes a Kalman filter that estimates the system's state.

The processed data are used to stabilise the vehicle at a specific position or fly predefined trajectories. Further, the data are logged to a SD card, and therefore, they are also available after the flights. Flight times up to 17 min are possible with the used battery. The temperature and humidity sensor IST HYT271 is the only payload of the system.

3.1.2 Fleet Communication

Installed on a ground station laptop, the open-source software © QGroundControl (QGC) developed by the Dronecode Foundation (Gagne et al. 2020) ensures the control of the UAV fleet (Fig. 3.2). The communication between the vehicles and the QGC relies on a 2.4 GHz WLAN-connection with Standard 802.11.g/n. All UAVs and the ground station have fixed IPs and are connected via a local network provided by a router (LANCOM OAP-822). Datagrams are exchanged via UDP ports and the communication is based on the MAVLink v2 protocol.

The software QGC allows to upload a priori generated flight plans to the ve-

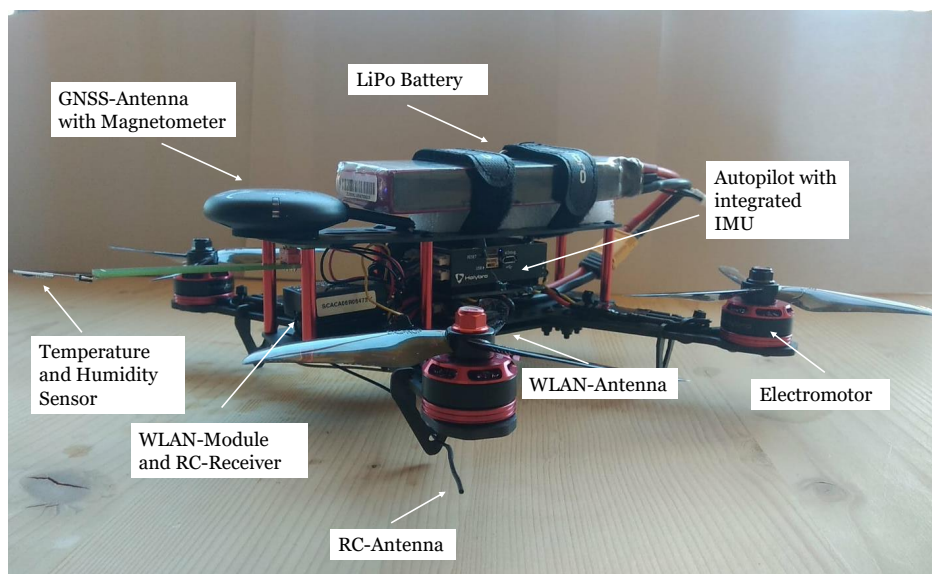


Figure 3.1: Holybro QAV250 quadrotor.

Table 3.1: Hardware of Holybro QAV250 quadrotor.

Mass	0.66 kg (incl. battery)
Dimension (length, width, height)	0.25 m x 0.2 m x 0.2 m
Frame	Carbon fibre
Rotors	4 x 3-blade T5040C, \varnothing 127 mm, Poly-carbonat
Motors	4 x Electromotors DR2205 KV2300
Battery	LiPo, 3500 mAh
Accelerometer and gyroscope	Two redundant sensors: Invensense ICM-20689 and Bosch BMI055
Magnetometer	iSentek IST8310
Barometer	Amsys MS5611
GNSS	ublox Neo-M8N GPS/GLONASS
Voltage and current sensor for battery supervision	Holybro Power Module PM07
Temperature and humidity sensor	IST HYT271 (weight: 2 g)

hicles. When creating these flight plans, it has to be taken care that the paths of the individual vehicles do not cross and that collisions are avoided. Further, the software monitors the fleet during the flight and different commands can be given to a single vehicle or the whole fleet. This includes instructions like 'Start-all', 'Return-to-launch' or 'land-all'.

As an additional backup, the vehicles are connected to a Graupner MZ-12 remote control (RC). A pilot can navigate a single UAV manually with this control.

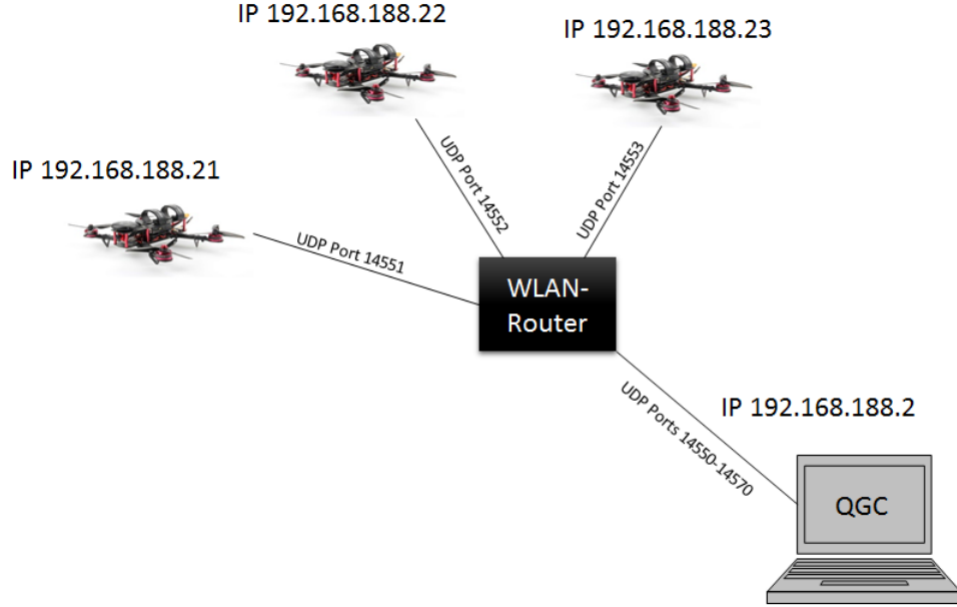


Figure 3.2: Schematic depiction of fleet communication. *Credits:* Norman Wildmann.

3.2 Wind Algorithm

The algorithm for retrieving the wind vector from quadrotor measurements is still in the development phase. In the following, an intermediate state is shortly summarized, which resolves the horizontal wind vector. This state is an extension of the algorithm presented in [Wetz et al. \(2021\)](#) and is the basis for all calculations within this work.

The underlying idea is to treat a quadrotor as a rigid body and solve the equations of motions in a reference system that moves with the vehicle (body system) using only internal sensor data. Resulting wind forces are then transformed to wind speeds with an appropriate calibration relation.

Introducing the mass m of the vehicle, the gravity constant g , the position vector in the body system

$$\mathbf{X}_b = \begin{bmatrix} x & y & z \end{bmatrix}^T, \quad (3.1)$$

the angular velocity vector in body frame

$$\omega_b = \begin{bmatrix} p & q & r \end{bmatrix}^T, \quad (3.2)$$

and the Euler angles in a fixed inertial frame

$$\Phi_i = \begin{bmatrix} \phi & \theta & \psi \end{bmatrix}^T, \quad (3.3)$$

the linear two-dimensional equations of motion in the body system read

$$m(\ddot{x} + q\dot{z} - r\dot{y}) = -mg[\sin(\theta)] + F_{w,x} \quad (3.4a)$$

$$m(\ddot{y} + p\dot{z} - r\dot{x}) = -mg[\cos(\theta)\sin(\phi)] + F_{w,y} . \quad (3.4b)$$

Here, the first terms on the left side are the accelerations, the second and third terms on the left side are the gyroscopic terms, the first terms on the right side are the gravitational forces and the last terms are the wind drag.

In a stable hover state, one can assume that the terms on the left hand side of equations (3.4a) and (3.4b) can be neglected, leading to

$$F_{w,x} = mg[\sin(\theta)] \quad (3.5a)$$

$$F_{w,y} = mg[\cos(\theta)\sin(\phi)] . \quad (3.5b)$$

Further, the vehicles are operated in the weather vane mode meaning that the yaw angle ψ is used to minimize the amplitude of the roll angle ϕ , such that the quadrotor always tries to yaw into the wind direction. [Wetz et al. \(2021\)](#) assumed that this adjustment occurs instantaneously and thus neglected equation (3.5b), such that only the pitch angle θ determines the dynamics. Here, this assumption is not made and both equations are considered.

[Wetz et al. \(2021\)](#) used the Rayleigh drag equation for the conversion of wind forces to wind speed. In the approach presented here, this relationship is more generalised in the form of

$$V_{w,j} = c_j(F_{w,j})^{b_j} , \quad (3.6)$$

with $j = x, y$, the wind vector component $V_{w,j}$ and the calibration constants c_j, b_j . For the determination of these calibration constants, reference measurements are needed (sec. 3.3). A detailed description of how these constants are obtained for each individual vehicle will be outlined in the publication [Wetz and Wildmann \(2022\)](#).

The fitted wind components in body system are then used to calculate the wind speed

$$ff = \sqrt{V_{w,x}^2 + V_{w,y}^2} . \quad (3.7)$$

The wind direction is determined by the orientation of the vehicle via the yaw angle ψ . However, a yaw offset $\Delta\psi$ is determined for each quadrotor by calibrating the mean values against a reference device ([Wetz and Wildmann 2022](#)), yielding the total yaw angle

$$\Psi = \psi + \Delta\psi . \quad (3.8)$$

Due to the response time of the weather vane mode, the instantaneous values are further corrected accordingly, leading to the wind direction ([Wetz and Wildmann 2022](#))

$$dd = \Psi + \tan\left(\frac{V_{w,y}}{V_{w,x}}\right) . \quad (3.9)$$

From the obtained wind speed and wind direction, zonal velocity

$$U = -f f \sin(dd) \quad (3.10)$$

and meridional velocity

$$V = -f f \cos(dd) \quad (3.11)$$

are calculated.

3.3 Field Campaign and Reference Instrumentation

The measurement campaign FESSTVaL (Field Experiment on Sub-Mesoscale Spatio-Temporal Variability in Lindenberg) initiated by the Hans-Ertel-Zentrum für Wetterforschung (HErZ) took place at the Meteorologisches Observatorium Lindenberg-Richard-Aßmann-Observatorium (MOL-RAO) in summer 2021. The campaign had the goal to investigate submesoscale phenomena like cold pools and wind gusts associated with thunderstorms. As part of this campaign, measurements have been conducted with the UAV fleet at the Grenzschichtmessfeld (GM) Falkenberg between June 21 and July 2.

GM Falkenberg (52° 10' N, 14° 07' E, 73 m above sea level) is located about 80 km south-east of Berlin. Typical differences in surface elevation are less than 100 m over a distance of 10 km around the site. The surface is dominated by grassland and cropland, but there are also some larger pine forest areas to the west ([Tab. 3.2](#) and [Fig. 3.3](#)).

At the site, the German Weather Service (DWD) maintains operational micrometeorological and boundary layer measurements. The main object is a 99 m high mast with various sensors attached. [Table 3.3](#) gives an overview of all sensors whose data are used in this work. The two sonic anemometers at 50 m and 90 m AGL serve as the main reference devices for the UAV measurements.

Table 3.2: Land use of GM Falkenberg.

Scale (radius around tower)	Land use
100 m	grassland
500 m	grass- and cropland
10 km	grass- and cropland (60%), pine forests (30%), lakes (5%) and settlements (5%)

**Figure 3.3:** Satellite image of GM Falkenberg and surrounding area.

Table 3.3: Reference instrumentation of 99 m mast.

Instrumentation	Levels (m)	Sensor type
Cup anemometers	10, 20, 40, 60, 80, 98	Thies cup anemometer 4.33303.22.000
Wind vanes	40, 90	Thies wind vane 4.3121.32.000
Sonic anemometers	2, 50, 90	METEK-1 USA
Temperature and humidity sensors	10, 20, 40, 60, 80, 98	Vaisala HMP-45 aspirated radiation shield Young model 43408
H ₂ O gas analyzer	2, 50, 90	LI75000RS
Barometer	1	Vaisala PTB220A
Precipitation sensor	1	OTT Hydromet GmbH: Pluvio (DWD version)
Sensor for shortwave radiation	2	Kipp&Zonen CM24
Sensor for longwave radiation	2	Kipp&Zonen CG4R

3.4 Flight Patterns

Different flight patterns have been performed during the field campaign, including calibration flights, vertical "drone tower" flights, validation flights for lidar VAD scans and horizontal flight patterns. In this section, only the calibration and horizontal flight patterns are described as they are relevant for this work.

For the calibration flights, five UAVs were placed 20 m west of the tower at 50 m and 90 m AGL in a north-south orientated line with a spacing of 5 m (Fig. 3.4a). Data from these flights were used for calibration (sec. 3.2) using sonic data as a reference. This thesis does not show the entire calibration procedure; that can be found in [Wetz et al. \(2021\)](#) and [Wetz and Wildmann \(2022\)](#). Instead, the performance of the calibration is presented. Section 3.5 gives detailed information about the corresponding data processing.

Figure 3.4b shows a schematic representation of the horizontal flight pattern. The mean wind direction of the last 10 min measured by the tower was used as a reference for determining the orientation of the pattern. Flexibly adjustable flight plans were created to align in total ten UAVs in a horizontal plane in both the streamwise x - and lateral y -direction. Here, the spacings between neighbouring UAVs were varied in a way such that as many different distances as possible are represented between 5 m and 205 m in x -direction and between 10 m and 70 m in

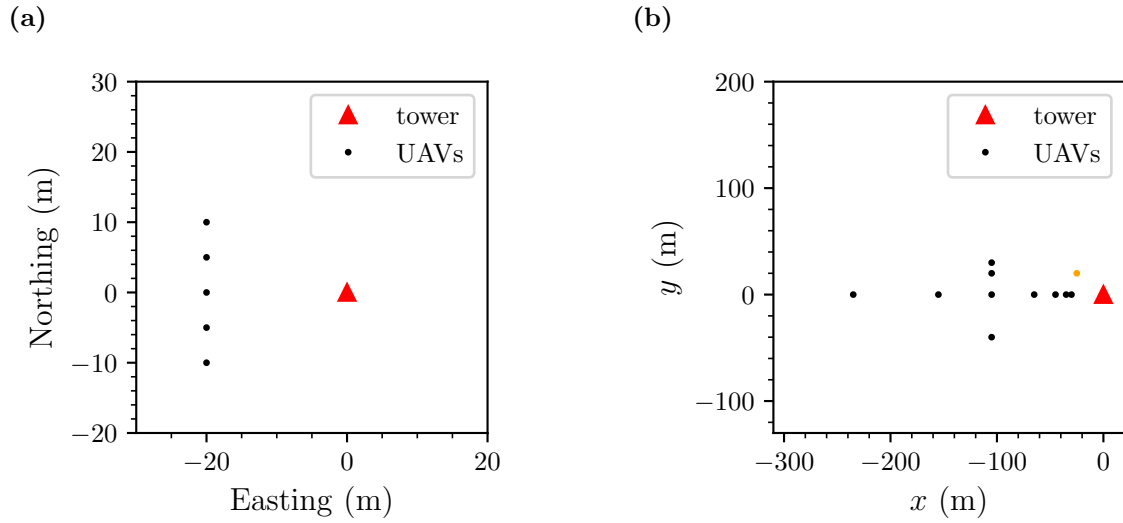


Figure 3.4: (a) Calibration pattern (b) Horizontal pattern with differing distances between neighbouring vehicles. Here, x denotes streamwise and y lateral direction. The orange dot indicates the position of the vertical profiling UAV.

y -direction when the UAVs are combined pairwise in the corresponding direction. This gives the possibility to calculate turbulence quantities as a function of the separation distance. Besides this horizontal pattern, in most of the cases one quadrotor additionally acted as a vertical background profiler by ascending with a constant speed of 1 m s^{-1} .

This horizontal pattern offers different evaluation possibilities: First, it allows the comparison of the different time averages of the spatially separated UAV measures. An assessment of the validity of equation (2.7) is given when an independent test for (quasi-)stationarity after Foken and Wichura (1996) is applied. The idea of this test is outlined in section 3.5.3. If stationarity is fulfilled, the spatially separated recordings can then provide an examination of the homogeneity assumption within the microscale with a maximum separation distance of 205 m. A proposed (quasi-)homogeneity test is also presented in section 3.5.3.

Besides the check of the homogeneity assumption, the varying distances between the UAVs in the horizontal pattern allow the calculation of cross-correlation functions (eq. (2.14)) and coherences (eq. (2.18)) for different spatial distances and thus can give an assessment of Taylor’s frozen turbulence hypothesis as outlined in section 2.4.

This measurement strategy was repeated at various heights and for different atmospheric conditions (neutral, convective and stable boundary layer), but the separation distances were always exactly the same as indicated in Figure 3.4b. Moreover, the UAVs were replaced such that longer measurement periods have been achieved. In this thesis, however, data are mainly evaluated for single horizontal patterns

without replacement. Only at some parts, results for longer measurement periods are outlined.

3.5 Data Processing

3.5.1 Interpolation, Filtering and Coordinate Rotation

The raw data from a single vehicle's sensors all have different time stamps and sampling resolutions. Therefore, the first step in processing was to bring them to a common time stamp. Hence, the data of each UAV were interpolated to a single time series with a resolution of 20 Hz. This resolution corresponds to the sampling rate of the sonic anemometer's raw data.

Afterwards, the ascent and descent were removed from the time series and only the period was selected during which the vehicle was hovering. This was done by looking where the three translational velocities of the quadrotor remained below a threshold for a certain time. Here, a limit of 0.5 m s^{-1} was used. Obviously, the effective measurement time is reduced when eliminating the time needed to fly to and from the measurement position.

For the hover state, zonal and meridional wind components were then computed with the algorithm presented in section 3.2. After that, a FFT low pass filter with a cut-off frequency of 1 Hz was applied to filter out high-frequency sensors noise. The choice of the cut-off frequency seems arbitrary at first, but we will see in chapter 4 that it is reasonable when examining power spectra.

For each vehicle the wind components were then rotated into a streamwise coordinate system. Since the current algorithm resolves only the horizontal wind components, a 'single rotation' instead of the standard double or triple rotation (e.g., [Golzio et al. 2019](#)) was applied. This rotation involves

$$\alpha = \arctan \left(\frac{\overline{U}}{\overline{V}} \right) \quad (3.12a)$$

$$u = U \cos(\alpha) + V \sin(\alpha) \quad (3.12b)$$

$$v = -U \sin(\alpha) + V \cos(\alpha) . \quad (3.12c)$$

Here, U is the zonal, V the meridional, u the streamwise and v the lateral velocity component. This rotation nullifies the mean lateral wind component ($\overline{v} = 0$).

The selection of the averaging period for this rotation and the subsequent analysis slightly differs for the calibration and horizontal pattern flights. Therefore, they are presented separately.

Calibration Flights

For the calibration flights, the entire period in hover state (approx. 14 min) for every quadrotor was used as an averaging time to lose as few data as possible. Since the calibration flights are used to compare UAV and sonic anemometer measures, the time interval for the corresponding sonic data was separately determined for each vehicle, ensuring exact matching. Further, the sonic data were also filtered with a cut-off frequency of 1 Hz and a single rotation was applied for a meaningful comparison. A double rotation had also been applied to the sonic data for randomly selected examples, but this did not result in significant differences compared to the single rotation.

Further two quality controls were applied to avoid erroneous data: Pairs of UAV and sonic measures were discarded from the comparison, where the mean wind direction measured by the UAV was between 330° and 50° via north, since here the tower's configuration leads to a disturbance of the flow. Further, only data are compared, where the mean wind speed measured by the sonic anemometer was higher than 3 m s^{-1} . This ensures that the weather vane mode worked adequately and the UAV faced in wind direction.

Horizontal Flight Patterns

For the horizontal pattern, it is advantageous to have a matching time interval for all UAVs involved. Therefore, the interval was set to the time when the last vehicle in the pattern started hovering until the first quadrotor started its return flight. Since the vehicles did not start simultaneously and had different paths to fly to their measurement position, the effective averaging period is reduced (approx. 13.5 min). After this processing step, the various vehicles still had slightly different time stamps, since the initial interpolation to 20 Hz was individually done for each UAV. But for computing cross-correlation functions (eq. (2.14)) and coherences (eq. (2.18)), it is useful to have a common one. Hence, all other vehicles were interpolated to a reference quadrotor. Analogously, the previously filtered sonic data were interpolated to the same time stamp as all UAVs involved.

In this work, only horizontal patterns are evaluated, which do fulfil the two quality controls (wind direction not between 330° and 50° via north and mean wind speeds higher than 3 m s^{-1}). Thus, the findings can be compared with the calibration results.

3.5.2 (Co-)variances and Spectra

The variances $\overline{u'^2}$ and $\overline{v'^2}$ and the covariance $\overline{u'v'}$ were calculated applying a linear detrending beforehand. Cross spectral densities and power spectral densities were

computed using Welch's average periodogram method (Welch 1967). Hereby, a Hanning window was used as a window function. Furthermore, the spectra were scaled by a scaling frequency, such that the densities are given in units of Hz^{-1} and integration over the frequency range is possible. For visualizations, the spectral densities were further averaged over logarithmically spaced bins.

3.5.3 Stationarity and Homogeneity Tests

The idea of the (quasi-)stationarity test after Foken and Wichura (1996) is outlined for the covariance $\overline{a'b'}$ of two turbulence variables a and b measured by a single device: The recorded time series is split into M shorter intervals and for each subinterval the covariance $\overline{a'b'}_i$ is calculated. The averaged value of this covariances

$$\overline{a'b'}_{\text{SI}} = \frac{1}{M} \sum_{i=1}^M \overline{a'b'}_i \quad (3.13)$$

is then compared with the covariance calculated over the whole interval $\overline{a'b'}_{\text{WI}}$ in the form of

$$ST = \left| \frac{\overline{a'b'}_{\text{SI}} - \overline{a'b'}_{\text{WI}}}{\overline{a'b'}_{\text{WI}}} \right| \cdot 100\% . \quad (3.14)$$

Stationarity is assumed, when $ST < 30\%$. Within this work, $M = 5$ subintervals were used.

Performing a test for (quasi-)homogeneity analogous to equation (3.14) would require many more spatially distributed measurements for a single time point than available. Therefore, a comparable test for (quasi-)homogeneity for a turbulence quantity q is proposed using the spatial mean of the time averaged quantity

$$[\bar{q}] = \frac{1}{N} \sum_{i=1}^N \bar{q}_i \quad (3.15)$$

as a reference. Here, N is the total number of UAVs involved and the index i runs over all vehicles in the horizontal pattern. The proposed test then reads

$$HT = \left| \frac{\sqrt{\frac{1}{N} \sum_{i=1}^N (\bar{q}_i - [\bar{q}])^2}}{[\bar{q}]} \right| \cdot 100\% , \quad (3.16)$$

which relates the standard deviation as a measure of spatial variability to the spatial mean of the time averaged quantity. Clearly, the question arises what threshold one should use for HT below which one can assume homogeneity. In analogy to the stationarity test, the author proposes a threshold value of 30%.

3.5.4 Treatment of Pattern Misalignment

When calculating cross-correlation functions (eq. (2.14)) and coherences (eq. (2.18)) in streamwise direction, it has to be taken into account that the mean wind direction over one flight can differ from the direction in which the horizontal pattern was aligned. As mentioned in section 3.4, this direction of the pattern was determined by tower measurements and often the last available values had quite a delay to the start of the UAV flights. Therefore, the orientation of the pattern was sometimes also estimated from previous UAV flights. This often led to a misalignment of the pattern and measured wind direction in the order of 10° . This misalignment is expressed through

$$\beta = dd_{\text{pattern}} - \overline{dd} , \quad (3.17)$$

with the alignment of the pattern dd_{pattern} and the measured mean wind direction \overline{dd} .

This misalignment has mainly two effects (Fig. 3.5): First, the turbulence signal is not advected exactly through both measurement devices in x -direction, instead it is displaced by

$$\Delta = \Delta x \sin(\beta) . \quad (3.18)$$

Second, the theoretical time delay according to the Taylor Hypothesis, where one expects maximal correlation between two time series, has to be reduced by $\cos(\beta)$, i.e.,

$$\Delta t = \frac{\Delta x \cos(\beta)}{\bar{u}} . \quad (3.19)$$

This corresponds to the time difference after which a turbulent structure is closest to the second sensor when it has previously passed through the first sensor. For the calculation of the displacement (eq. (3.18)) and the theoretical time delay (eq. (3.19)), the mean values for \overline{dd} and \bar{u} of the two individual measurements were used.

The influence of the displacement on the maximum value of the cross-correlation function can be examined when the cross-correlation function is calculated between quadrotors aligned in x -direction with those aligned in y -direction. For a fixed Δx , cross-correlation functions can be calculated as a function of total displacement (Fig. 3.5)

$$\Delta_{\text{Total}} = \Delta x \sin(\beta) + \Delta y \cos(\beta) . \quad (3.20)$$

Dependent on the signs of β and Δy , the two terms can sum up or partly cancel each other.

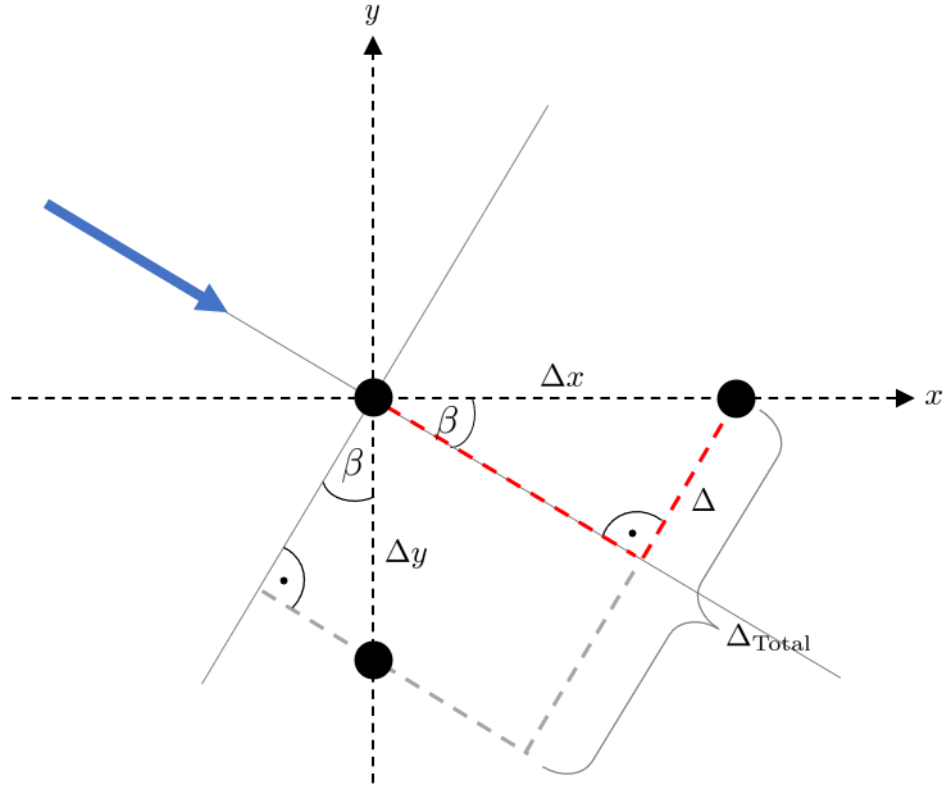


Figure 3.5: Schematic representation of the situation when the wind direction does not match with the pattern alignment. The blue arrow shows the wind direction and the dark dots indicate the measurement points. The turbulence pattern does not travel exactly through the two points in x -direction, but with a displacement Δ (eq. (3.18)). Further, the definition of the the total displacement Δ_{Total} (eq. (3.20)) is illustrated.

3.5.5 Data for Atmospheric Conditions

Pre-processed data from the tower are used to assess the atmospheric boundary conditions during the evaluated horizontal flight patterns. Only temperature measures at different levels were converted to potential temperatures. The necessary values for pressure were obtained from the surface value by integrating the hydrostatic equation over an assumed isothermal layer.

Vertical temperature profiles of the UAVs are employed to judge the atmospheric conditions as well. At the time of writing this thesis, corrections for possible biases in the temperature data had not been conducted yet. To better compare the measured vertical gradients with the tower measurements, however, a constant offset was added to the temperature data at some points based on a subjective comparison of the datasets. This is pointed out in the corresponding parts in chapter 4.

Chapter 4

Results

This chapter starts with the presentation of the calibration performance (sec. 4.1). The purpose of that section is to estimate the measurement accuracy of the UAVs to be able to interpret the subsequent findings adequately. Afterwards, three case studies are presented. The main objective is to investigate the homogeneity assumption and the Taylor hypothesis for a neutral (sec. 4.2), a convective (sec. 4.3) and a stable (sec. 4.4) atmospheric boundary layer with respect to the accuracy of the UAV measures and the horizontal measurement strategy.

4.1 Calibration Results

The calibration flights were conducted throughout the two-week long measurement campaign to encompass as many different atmospheric conditions as possible. This should ensure that the measurement accuracies found here can be transferred to all case studies investigated subsequently.

The performance of the calibration is evaluated in the form of scatter plots comparing sonic and UAV measurements (Fig. 4.1). Shown are 14 min averages of low-pass filtered data with a cut-off frequency of 1 Hz. As mentioned in section 3.5.1, data have been discarded where the wind direction was between 330° and 50° over north or where the mean wind speed was less than 3 m s^{-1} .

Table 4.1 summarises the performance of the calibration in terms of root mean square error σ_{RMS} and correlation coefficient r . Further, linear regression models $y = ax + b$ are fitted to the data. The p-values for the null hypothesis that the slope a of the linear fits is zero, are very small ($< 10^{-20}$) for all variables. This is also reflected in high to very high correlation coefficients (Tab. 4.1).

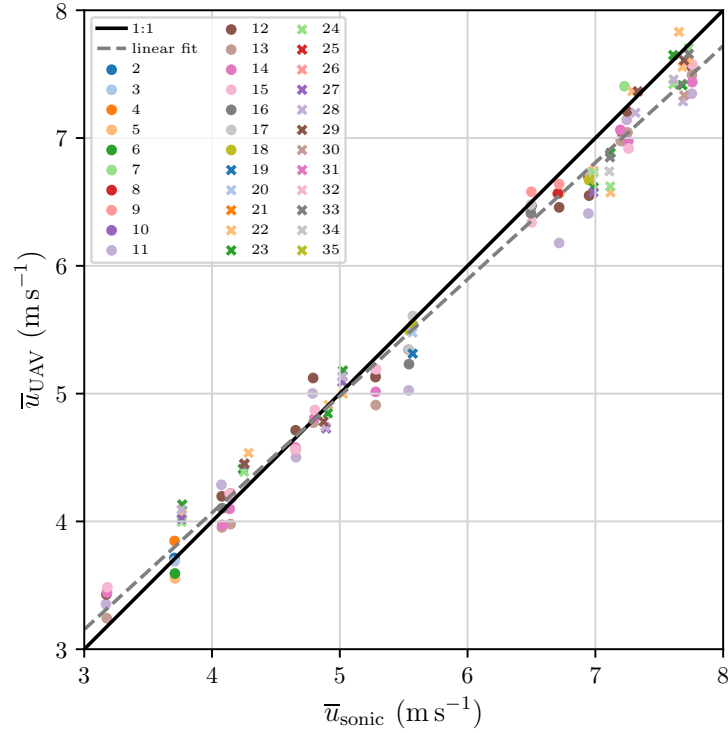
The linear fit for the mean wind speed (Fig 4.1a) indicates that the UAV measurements are systematically slightly too low for the higher depicted values. The linear fits for the mean wind direction (Fig. 4.1b) and streamwise variance (Fig. 4.1c)

Table 4.1: Root mean square error σ_{RMS} and correlation coefficient r between sonic anemometer and UAV measures calculated from the data of the calibration flights.

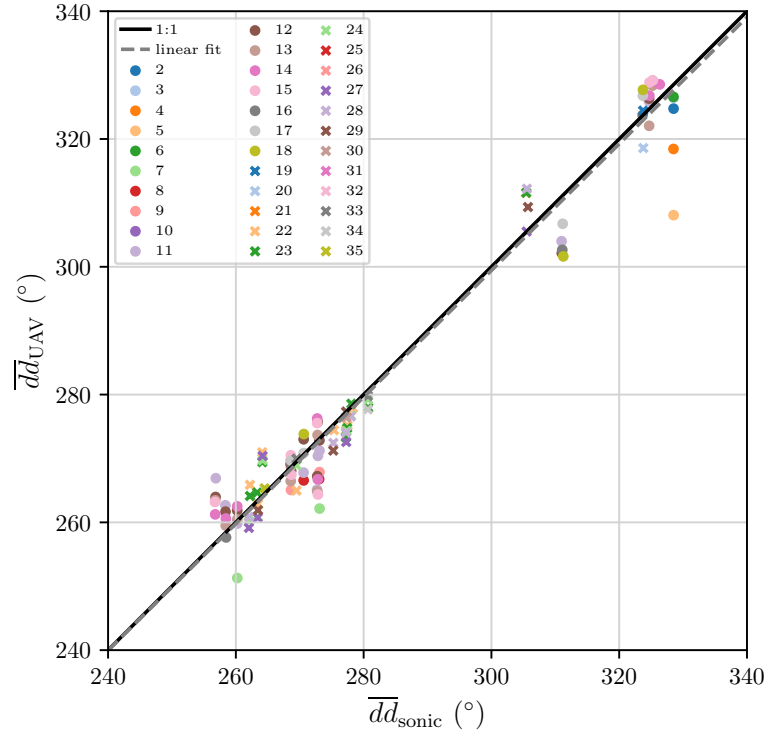
Variable	σ_{RMS}	r
\bar{u}	0.21 m s^{-1}	0.99
\overline{dd}	4.6°	0.98
$\overline{u'^2}$	$0.15 \text{ m}^2 \text{ s}^{-2}$	0.95
$\overline{v'^2}$	$0.13 \text{ m}^2 \text{ s}^{-2}$	0.96
$\overline{u'v'}$	$0.08 \text{ m}^2 \text{ s}^{-2}$	0.90

almost coincide with the identity lines. Thus, deviations between UAV and sonic measurements can be treated mainly statistically. The slope of the fit for the lateral variance is slightly lower than one (Fig. 4.1d). But the fit almost lies on the identity line in the range where most of the data have been recorded. The fit for the horizontal covariance shows that the absolute values of the UAV measurements are underestimated for the negative values (Figure 4.1e). Furthermore, given the small magnitude of the measurements and the calculated root mean square error, high relative errors are present.

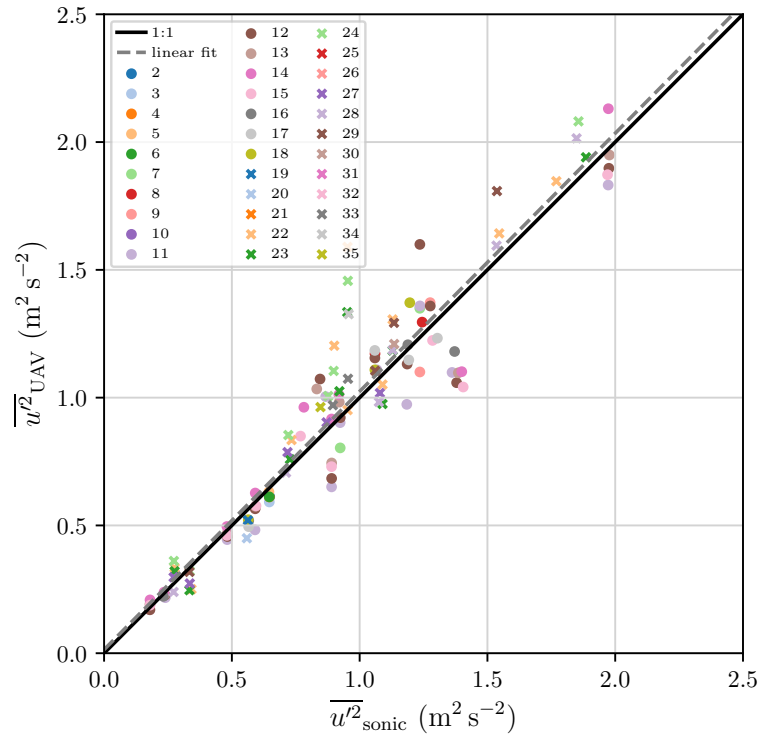
(a)



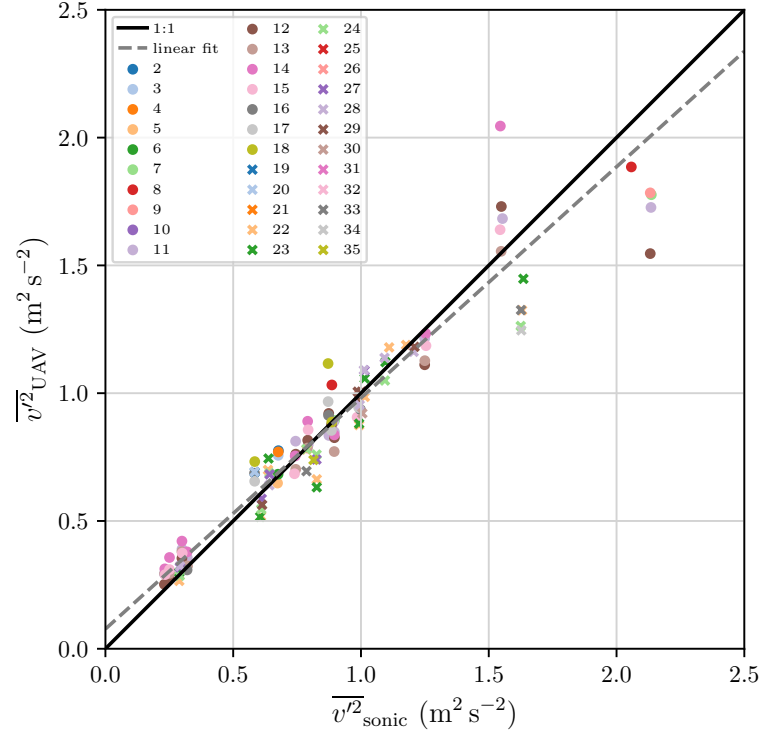
(b)



(c)



(d)



(e)

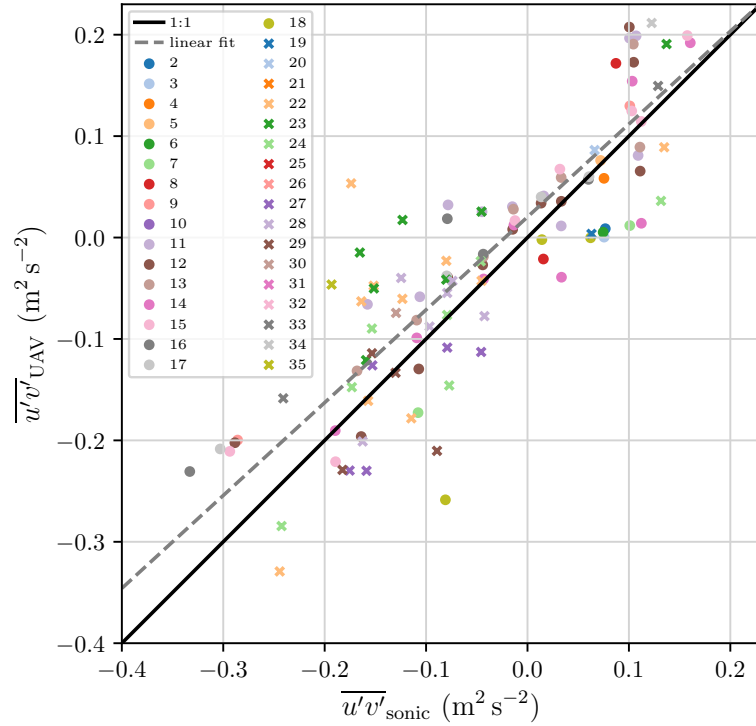


Figure 4.1: Calibration results for (a) mean wind speed, (b) mean wind direction, (c) variance of streamwise velocity, (d) variance of lateral velocity and (e) covariance of horizontal velocities. 14 min mean values of UAV and sonic measurements are compared. All data have been low pass filtered with a cut-off frequency of 1 Hz.

4.2 Near Neutral Boundary Layer

4.2.1 Atmospheric Conditions

An upper level trough and corresponding surface low with center over West Poland influenced the weather at the site on 2021-06-30. A cold front slowly moving over Brandenburg led to precipitation from the morning to early afternoon (Fig. 4.3e). Overcast sky with very low cloud base (approx. 200 m) from the morning till afternoon dampened the incoming solar radiation, such that no pronounced daily cycle of net radiation, sensible heat flux (Fig. 4.3a), turbulent kinetic energy (Fig. 4.3b) and potential temperature (Fig. 4.3c) developed. Instead the air temperature decreased during the rain period. In addition, more available energy was converted into latent heat than into sensible heat due to the wet soil after the rainy phase (Fig. 4.3a).

These conditions led to suppressed convectively driven turbulence. Instead, turbulence was mainly driven by shear in a westerly flow with moderate wind speeds (Fig. 4.3d). Hence, the atmosphere near the ground was near neutral stratified (Fig. 4.2a and 4.3c) with an almost logarithmic wind profile (Fig. 4.2b).

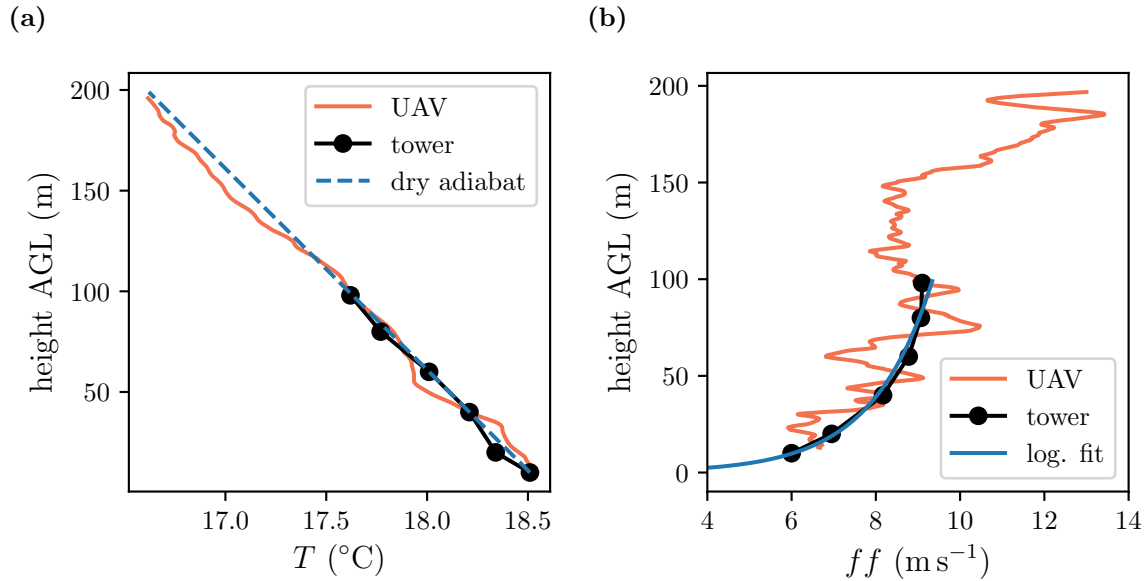
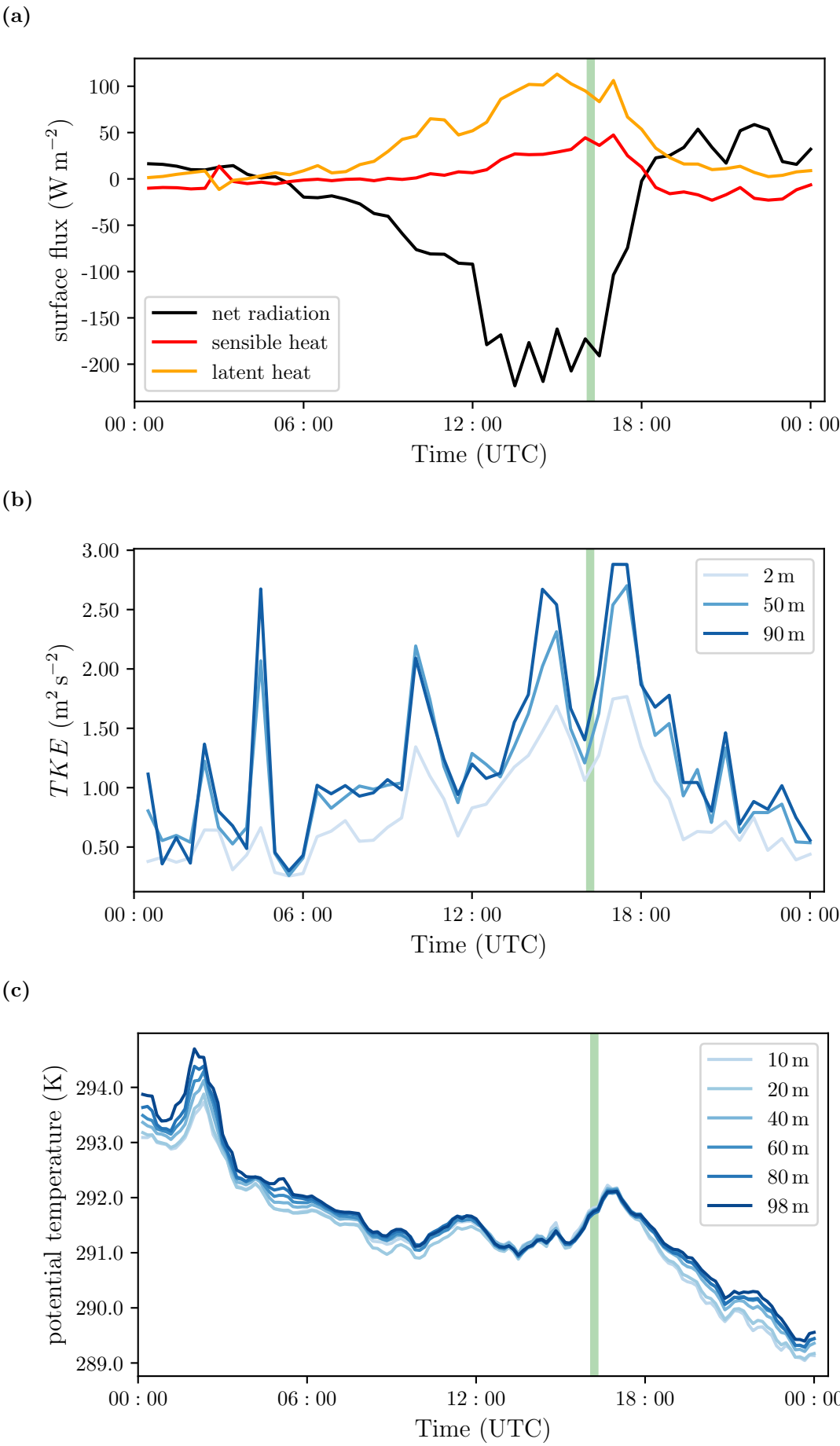
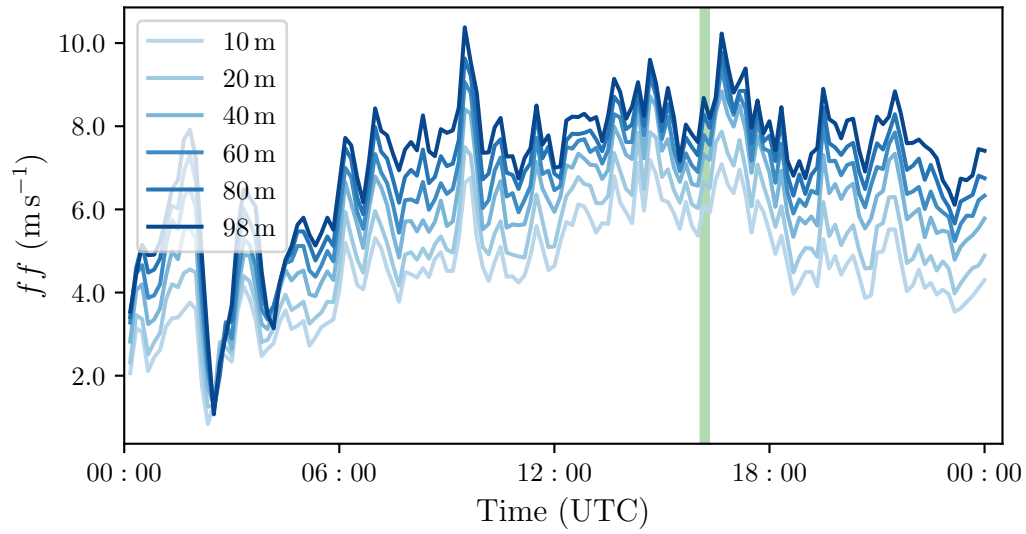


Figure 4.2: Vertical profiles of (a) temperature and (b) wind speed for the near neutral case on 2021-06-30 during the horizontal flight pattern. Tower measurements are 1 min averages with start of the averaging time at 16:09:00 UTC and UAV values are moving averages of 5 s with start of the profile at 16:09:36 UTC. A constant value of 0.4°C has been subtracted from the UAV temperature measures for a better comparison of the gradients. In (b) a logarithmic fit after equation (2.2) with $u_* = 0.56 \text{ ms}$ and $z_0 = 0.14 \text{ m}$ is additionally depicted.



(d)



(e)

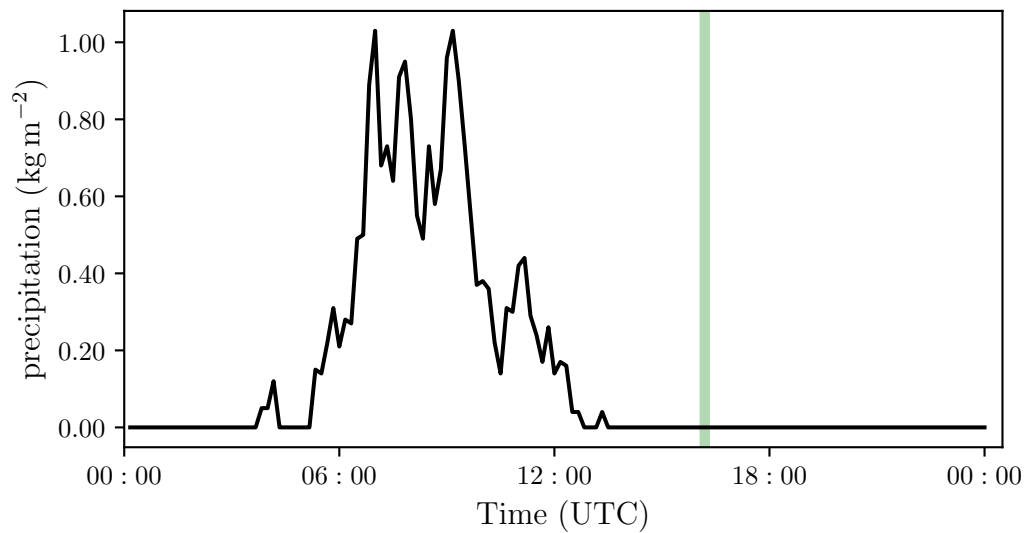


Figure 4.3: Tower measurements of daily cycle of (a) surface fluxes, (b) turbulent kinetic energy at different heights, (c) potential temperature at various levels, (d) wind speed at several heights and (e) precipitation for the near neutral case on 2021-06-30. The surface fluxes and turbulent kinetic energy have been processed with an averaging time of 30 min, the temperature and wind speed values are 10 min averages and the precipitation is the sum over 10 min. The time labels are at the end of the averaging interval. The green rectangle indicates the time of the horizontal flight pattern.

4.2.2 Spatially Distributed Measurements in the Horizontal Pattern

The horizontal pattern for the near neutral case took place at 90 m AGL between 2021-06-30 16:05:00 and 2021-06-30 16:18:30 UTC with an orientation of the x -axis towards 260° (Fig. 4.4a). Figure 4.5 shows the filtered timeseries of streamwise velocity for the sonic and the two nearest UAVs #11 and #12. For a better comparison, the series of the sonic and of UAV #12 are shifted by the advection time with the mean wind speed (eq. (3.19)). Qualitatively, the time series give the impression that the quadrotors can resolve the turbulence in a meaningful way. (Quasi-)stationarity tests after Foken and Wichura (1996) indicate that we can assume stationary conditions during the flight period (Tab. 4.2).

Spatially separated measurements of mean wind speed (Fig. 4.4b) indicate that all quadrotors except UAV #18 underestimate the speed by $0.1\text{--}0.4\text{ m s}^{-1}$. This is in accordance with the findings in section 4.1 for the given magnitude of mean wind speed (Fig. 4.1a). The measured wind direction is slightly higher than the alignment angle of the pattern of 260° for all quadrotors and the sonic except for UAV #7. Thus, small displacements (eq. (3.18)) of a measured turbulent structure are present.

All quantities of interest (mean wind speed, mean wind direction, streamwise variance, lateral variance and horizontal covariance) show deviations from the sonic (Fig. 4.4) in the order found for the calibration flights (Tab. 4.1). There are some larger deviations, but these are not attributed to a single UAV for all variables. There are neither significant differences between quadrotors aligned in x -direction and those aligned in y -direction nor is there a discernible trend along one direction.

Except for the horizontal covariance, calculated standard deviations of the spatially distributed UAV measurements (Tab. 4.3) are lower than the measurement accuracies inferred from Table 4.1. This means that possible inhomogeneities are masked by the measurement uncertainty. Despite the influence of the measurement uncertainty on the variability, the flow for these variables would be considered homogeneous (Tab. 4.3) according to the proposed (quasi-)homogeneity test (eq. (3.16)). The (quasi-)homogeneity test for the horizontal covariance yields exact the proposed threshold value of 30% (Tab. 4.3).

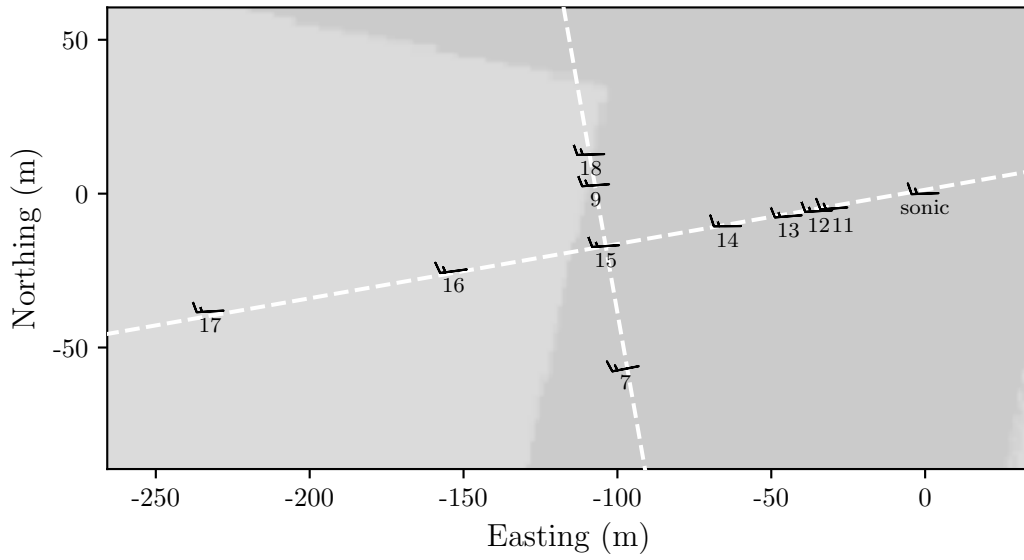
Table 4.2: (Quasi-)stationarity test after equation (3.14) for the near neutral case on 2021-06-30. Stationarity is assumed for values below 30%.

Variable	sonic	UAV #11
$\overline{u'^2}$	7%	5%
$\overline{v'^2}$	7%	5%
$\overline{u'v'}$	20%	12%

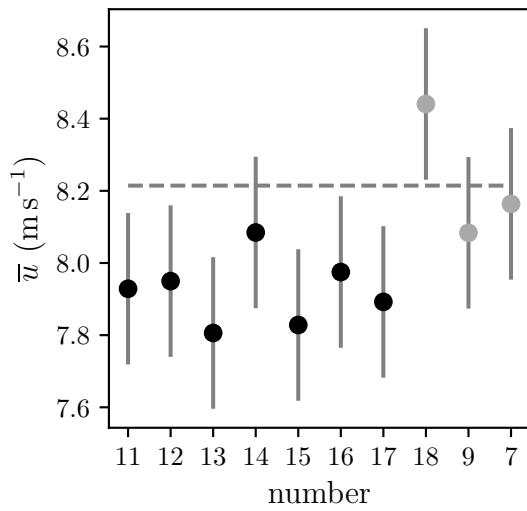
Table 4.3: Standard deviation σ_{UAV} of spatially distributed UAV measurements and (quasi-)homogeneity test HT after equation (3.16) for the near neutral case on 2021-06-30.

Variable	σ_{UAV}	HT
\bar{u}	0.18 m s^{-1}	2%
\overline{dd}	2.8°	—
$\overline{u'^2}$	$0.11 \text{ m}^2 \text{ s}^{-2}$	6%
$\overline{v'^2}$	$0.09 \text{ m}^2 \text{ s}^{-2}$	6%
$\overline{u'v'}$	$0.11 \text{ m}^2 \text{ s}^{-2}$	30%

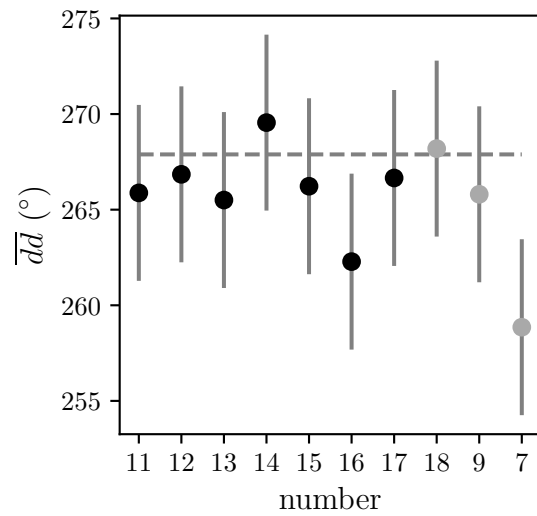
(a)



(b)



(c)



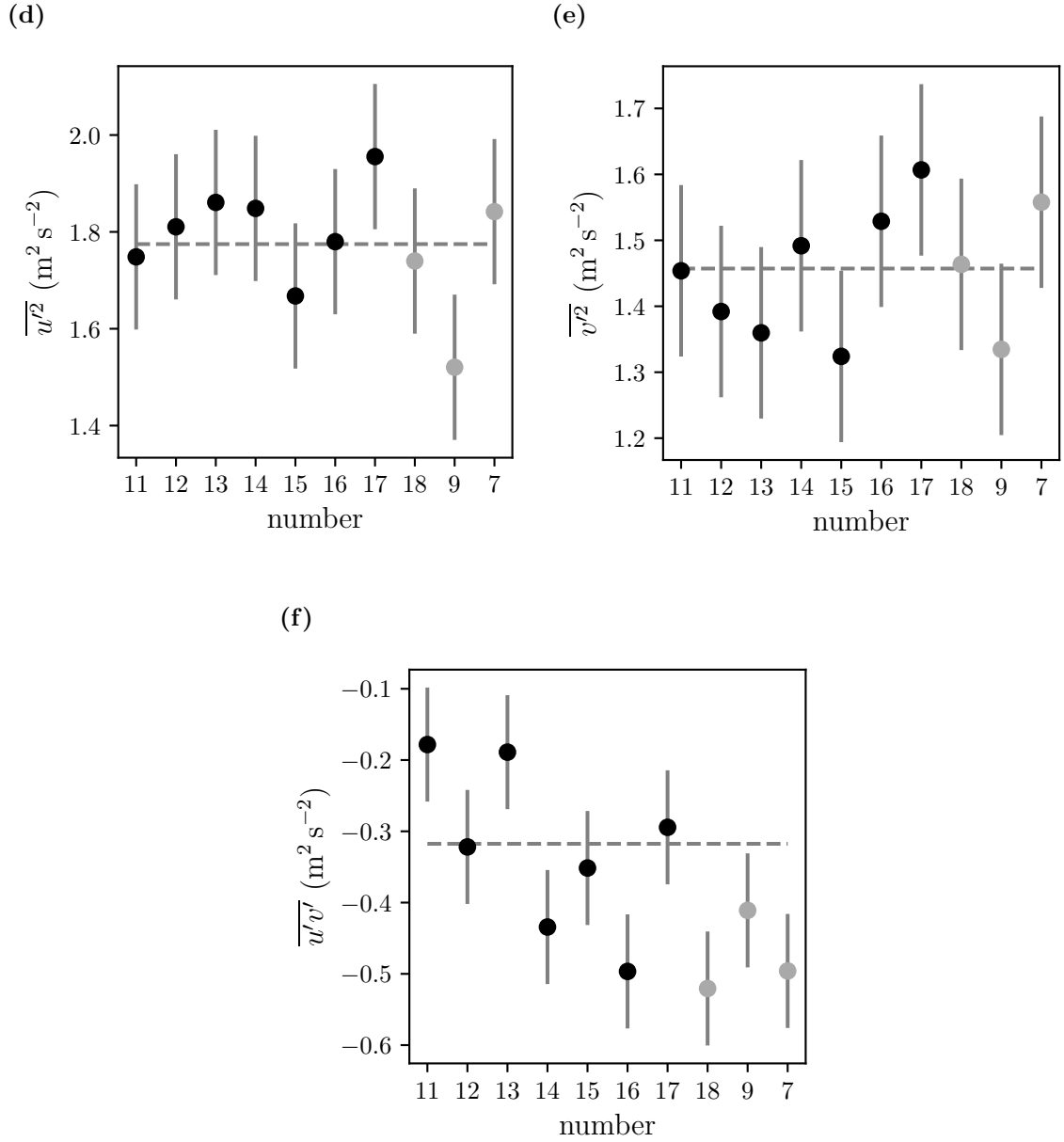


Figure 4.4: (a) Horizontal pattern with wind barbs in knots and UAV labelling for the near neutral case on 2021-06-30. The light gray in the background indicates corn field and the dark gray grassland. Spatially distributed measurements of (b) mean wind speed, (c) mean wind direction, (d) variance of streamwise velocity, (e) variance of lateral velocity and (f) covariance of horizontal velocity components. Black dots are measurements of quadrotors in x -direction of the flight pattern and gray dots are measurements of quadrotors in y -direction. The gray dotted lines are sonic measurements. The root mean square errors after Table 4.1 are shown as error bars.

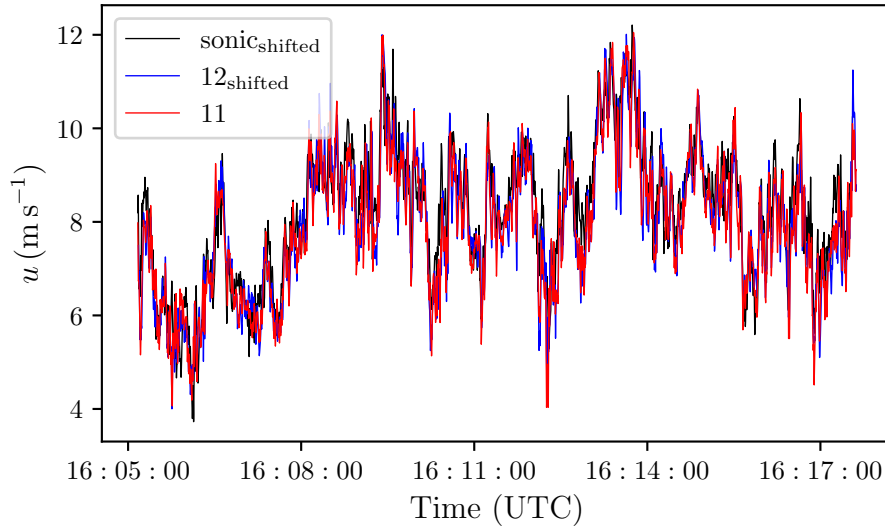


Figure 4.5: Time series of streamwise velocity for the near neutral case on 2021-06-30. Shown are series for the sonic anemometer and the two nearest UAVs #11 and #12. The timeseries of the sonic and of UAV #12 are shifted according to equation (3.19).

4.2.3 Power Spectra

Figure 4.6 shows filtered and unfiltered power spectral densities for the sonic anemometer and the two nearest UAVs #11 and #12. Kolmogorov’s law (eq. (2.9)) for the inertial subrange is additionally drawn as reference.

The spectra match reasonably for the lower frequency range, and they start to follow Kolmogorov’s law. Around $f = 1$ Hz, however, the unfiltered UAV spectra start to deviate from the sonic spectrum and the theoretical line. Internal sensor noise causes this behaviour. After a peak at around $f = 2$ Hz, the unfiltered UAV spectra drop. This decrease is caused by the integrated Kalman filter.

The shown spectra demonstrate that the choice of the cut-off frequency of 1 Hz is appropriate for this particular case. However, the (co-)variances are systematically underestimated when higher frequencies are neglected. This error can be estimated when the variances for filtered and unfiltered sonic data are compared. That calculation reveals a relative error for the streamwise variance of about 3%. However, one has to consider that the unfiltered sonic spectrum deviates from Kolmogorov’s law in the high-frequency range (Fig. 4.6). Therefore, the systematic relative error for the streamwise variance may be smaller in reality.

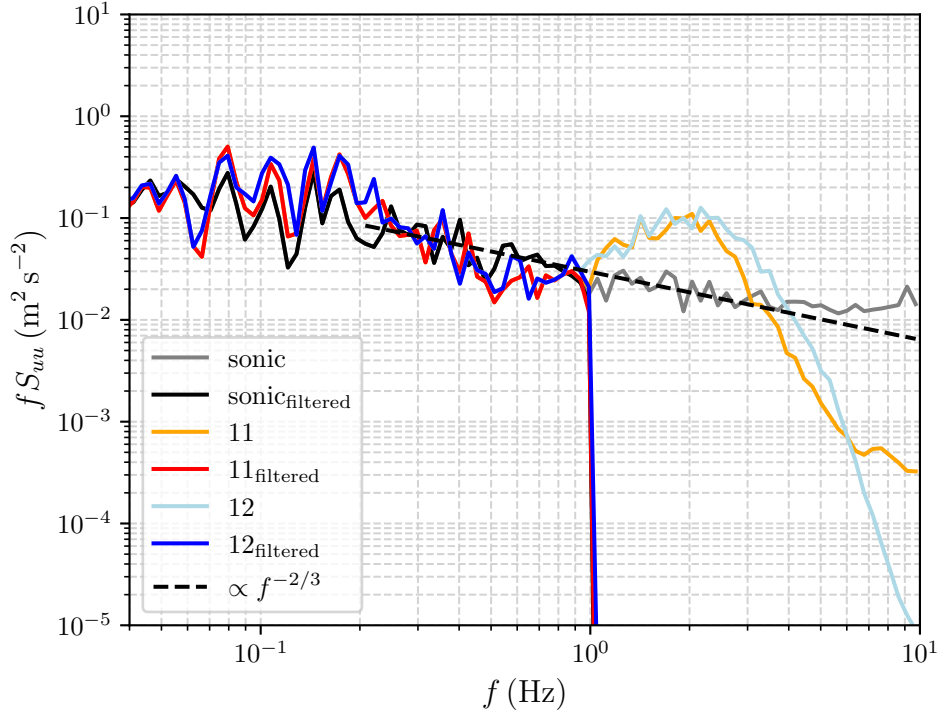


Figure 4.6: Power spectral densities multiplied by frequency of streamwise velocity for the near neutral case on 2021-06-30. Shown are unfiltered and filtered spectra for the sonic and the two nearest UAVs #11 and #12.

4.2.4 Cross-correlation and Coherence

Figure 4.7a shows cross-correlation functions calculated between vehicle #11 and all other quadrotors in the x -direction. Further, vertical lines are depicted indicating the theoretical expected positions of the peaks after equation (3.19). Differences between the locations of the maxima and the theoretical expected ones, named lag error, are plotted in Figure 4.7b. In this plot, however, x is not seen as the fixed position of UAV #11. Instead, results are considered for all possible combinations of the vehicles in x -direction.

The absolute value of the lag error grows with increasing distance Δx . This may partly be explained by the fact that the mean wind speed is calculated as the average of the measured values for each combined pair. Since the UAVs slightly underestimate the mean wind speed for this specific case (Fig. 4.4b), the theoretical time lag (eq. (3.19)) is slightly overestimated. Therefore, the lag errors were additionally calculated using sonic data, which leads to smaller deviations from zero (Fig. 4.7b). Thus, considering this systematic uncertainty, the maxima occur at time lags that are compatible with the Taylor hypothesis.

Further, the magnitude of the peaks decreases with increasing distance Δx (Fig. 4.7a). This is shown in more detail in Figure 4.8a, where the maxima of

all pairwise correlation functions are depicted. That decrease with distance Δx or equivalent evolution time Δt (eq. (3.19)) gives a hint that Taylor's frozen turbulence hypothesis is not totally valid or at least not for all scales. The turbulent eddies evolve during the travel time leading to cross-correlation maxima smaller than one. At this point, it should be mentioned that the turbulence intensity calculated with sonic data was 0.16 during the flight, after which the Taylor hypothesis is considered applicable (eq. (2.12)).

It should be noted, however, that even if Taylor's frozen turbulence hypothesis were perfectly valid, the cross-correlation would only be exactly one if the instruments were free of measurement uncertainty. Moreover, as discussed in section 3.5, a non-perfect alignment of the pattern's x -axis with the mean wind direction leads to displacements of the turbulent structures.

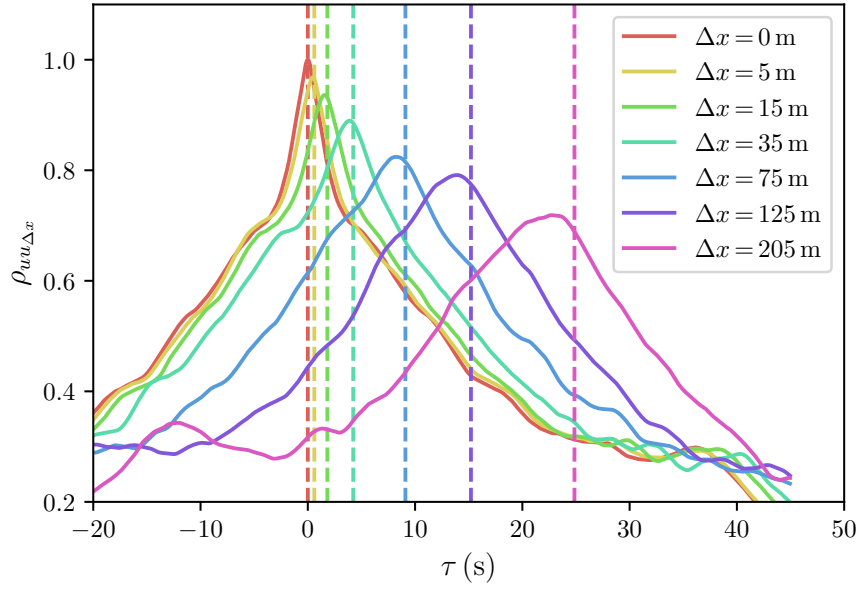
The influence of these displacements is investigated in Figure 4.8b. There, maxima of cross-correlation functions are plotted for fixed Δx , but for different total displacements (eq. (3.20)). The values were obtained by combining the UAVs #11, #12, #13 and #14 aligned in the x -direction with the quadrotors #18, #9, #15 and #7 in the y -direction. For a fixed Δx , a clear dependence of the cross-correlation maxima on the total displacement can be seen. Therefore, the displacements (eq. (3.18)) are plotted as an additional axis in Figure 4.8a. Unfortunately, there is no obvious approach - or at least the author is not aware of it - to find a universal relation distinguishing between the exact magnitudes of the decrease caused by the evolution of the eddies during the advection time and the decline caused by the displacement. However, the displacements must be taken into account when interpreting the results.

The dependence of Taylor's hypothesis on the eddies' scales is shown in Figure 4.9 through calculated coherences. Two main results can be deduced: First, the coherence decreases with decreasing eddy size for a fixed separation distance Δx . Second, coherence decreases with increasing separation distance Δx (evolution time Δt) for a fixed scale. Taken together, this means that the smaller eddies evolve relatively quickly and thus, the idea of treating them as frozen becomes questionable. However, larger eddies change their shape more slowly, and Taylor's hypothesis is applicable for a longer time. This finding is discussed in more detail in chapter 5.

The UAVs in the measurement pattern were replaced so that a longer measurement duration of about 25 min was achieved and larger scales could be resolved. The appendix shows the corresponding coherence plot (Fig. A.1). Since vehicle #21, which replaced vehicle #11, had problems during the flight, x is the fixed position of the combined quadrotors #12_22 in this plot. The coherence for the larger resolved scales is almost one for the investigated distances (evolution times). These eddy sizes are much larger than the dimensions of the measurement pattern and the

results show that they almost not evolve while moving from one sensor to the next. This means that the shorter measurement period without exchanging the UAVs is sufficient for the scale of the measurement pattern to investigate the decrease of coherence. Longer measurement times would only be necessary if larger distances between the UAVs were also considered.

(a)



(b)

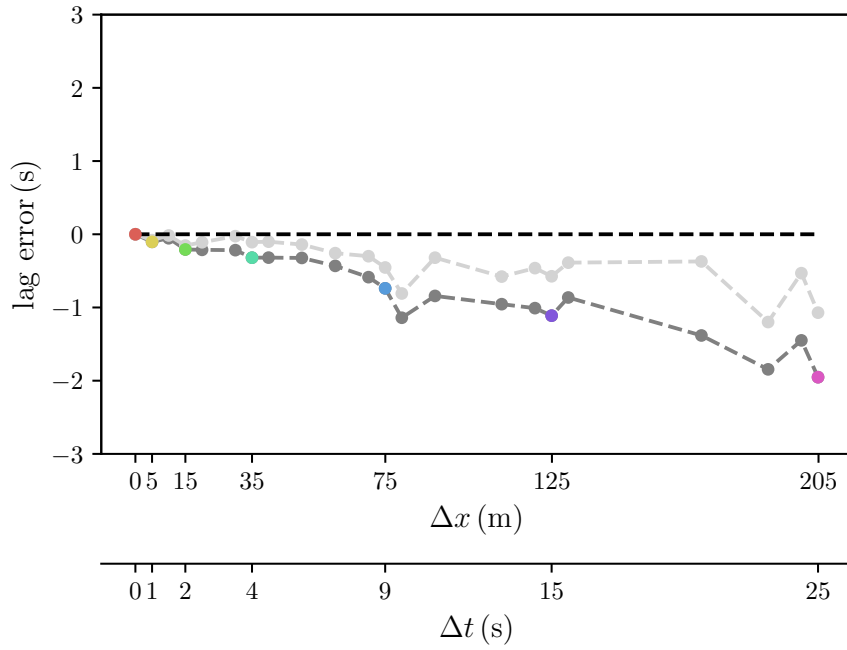
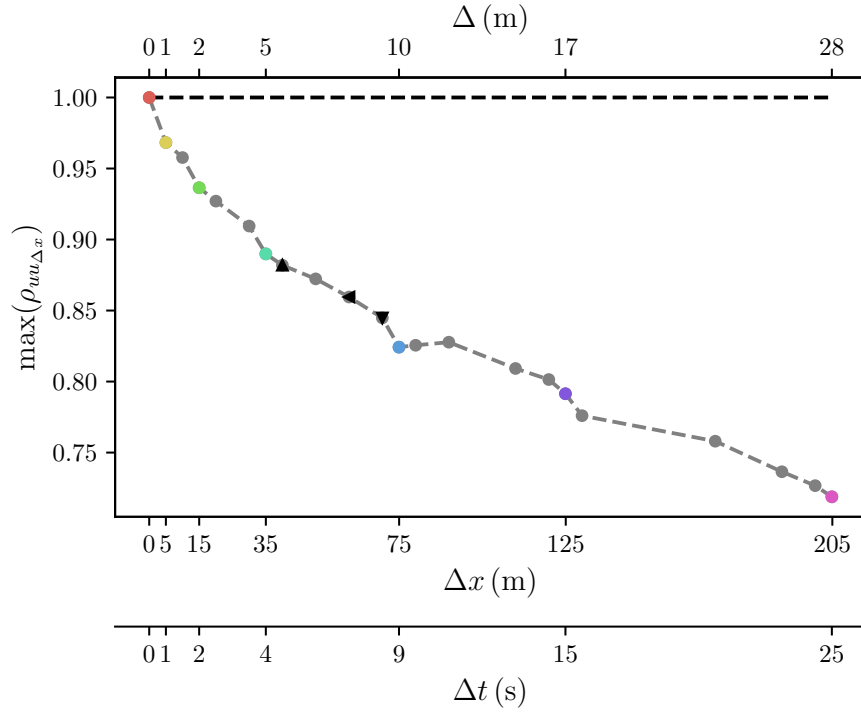


Figure 4.7: (a) Cross-correlation function of streamwise velocity for different Δx as function of time lag τ for the near neutral case on 2021-06-30. Here, x is the fixed position of vehicle #11. The vertical lines show the theoretically expected locations of the maxima according to equation (3.19). (b) Difference between the locations of the peaks and the theoretical ones (lag error) calculated with sonic data (light gray) and with mean values of corresponding UAV pairs (dark gray). In contrast to (a) x is not fixed, instead all possible combinations of the vehicles are shown, with the coloured dots matching the combinations in (a). A second axis has been added, where the distances Δx have been converted to time differences Δt after equation (3.19).

(a)



(b)

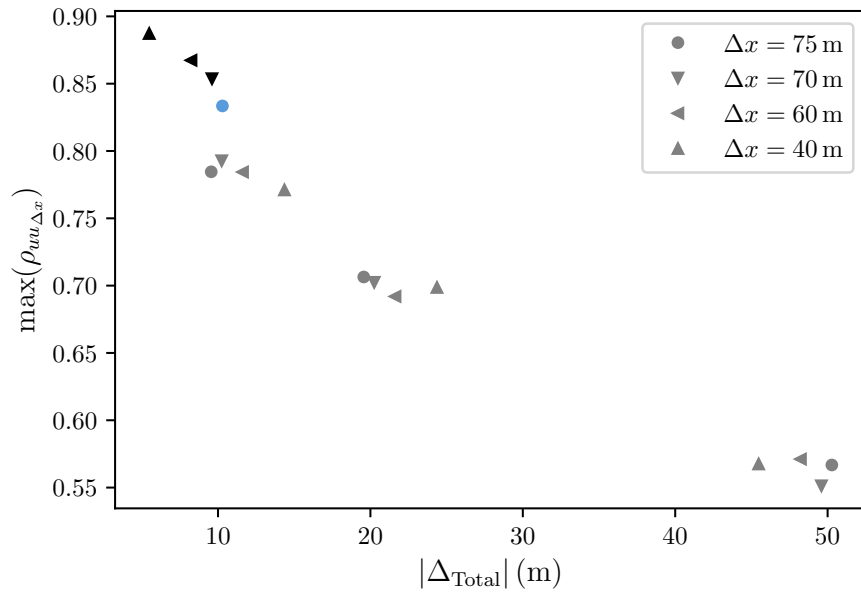


Figure 4.8: (a) Maxima of cross-correlation function of streamwise velocity depending on distance Δx . In contrast to Figure 4.7a, x is not fixed, instead all possible combinations of the vehicles in x -direction are considered. Coloured values correspond to the peaks in Figure 4.7a. The axis on the top is the displacement after equation (3.18). A second axis on the bottom has been added where the distances Δx have been converted to time differences Δt after equation (3.19). (b) Maxima of cross-correlation functions as a function of the absolute value of total displacement (eq. (3.20)). For that, UAVs in x -direction have been combined with vehicles in y -direction. The values depicted with black triangles and the blue dot are also shown in (a).

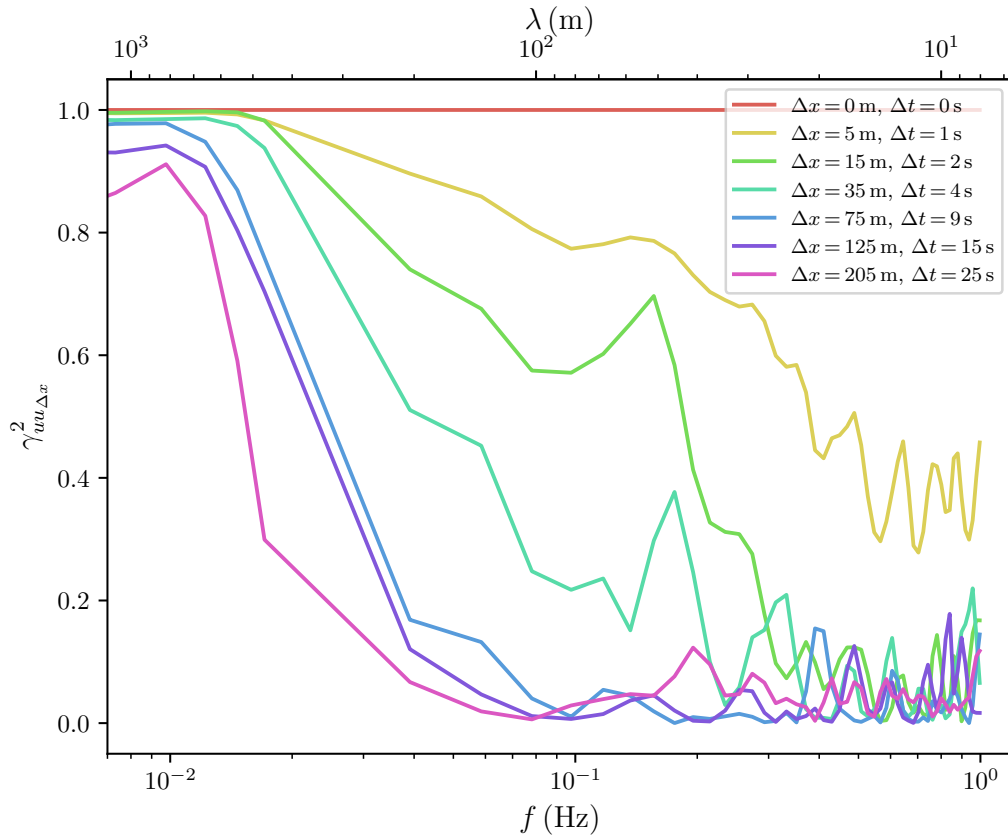


Figure 4.9: Coherence of streamwise velocity for different spatial distances Δx or equivalent evolution time Δt (eq. (3.19)) for the near neutral case on 2021-06-30. Here, x is the fixed position of vehicle #11. Frequencies have been converted to wavelengths after equation (2.11) (top axis).

4.3 Convective Boundary Layer

4.3.1 Atmospheric Conditions

An upper level low over the North Sea and a weak ridge over the Iberian Peninsula and western France determined the synoptic weather situation over Europe on 2021-07-02. A frontal system over Central Europe was not present. After an overcast night, the sky cleared up in the morning hours leading to a pronounced diurnal cycle of net radiation with a significant part of the energy being converted into sensible heat (Fig. B.1a). This led to a convectively driven daily cycle of turbulent kinetic energy (Fig. B.1b) and potential temperature (Fig. B.1c). The horizontal flight pattern took place around the maxima of these quantities.

Unfortunately, no vertical profile was performed at exactly the time the horizontal pattern was conducted. Therefore, the last available vertical profile is depicted in Figure 4.10, which was performed around 43 min before. The author checked

also tower profiles during the flight, but they do not show large deviations from the displayed profiles. Inferred from the tower profile, a superadiabatically stratified surface layer up to slightly above 50 m (Fig. 4.10a) with a weak wind speed gradient (Fig. 4.10b) was present.

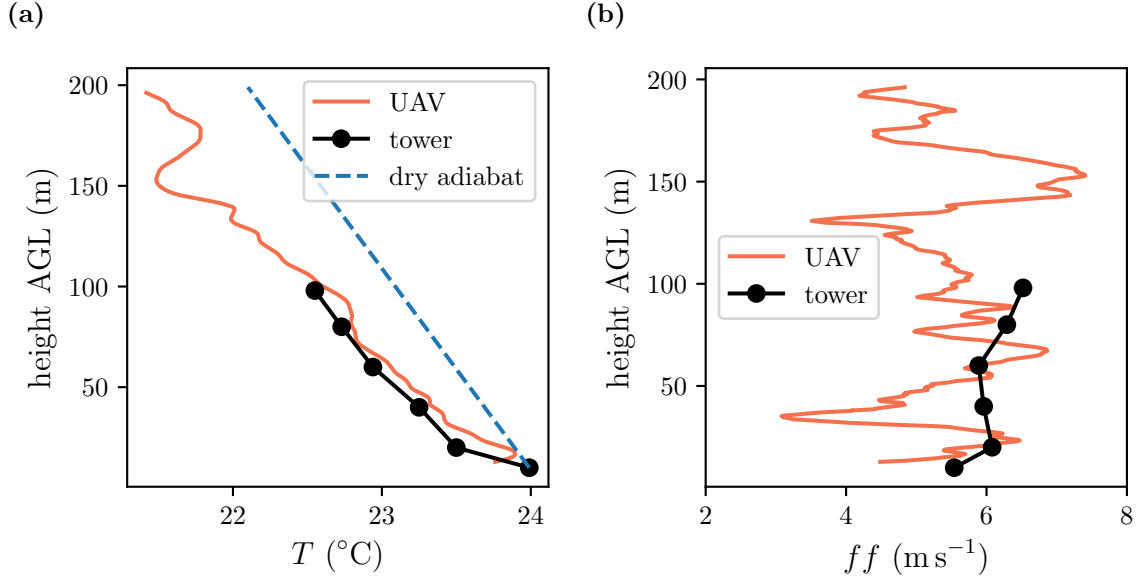


Figure 4.10: Vertical profiles of (a) temperature and (b) wind speed for the convective case on 2021-07-02 conducted around 43 min before the horizontal flight pattern. Tower measurements are 1 min averages with start of the averaging time at 14:31:00 UTC and UAV values are moving averages of 5 s with start of the profile at 14:30:44 UTC. A constant value of 1 °C has been subtracted from the UAV temperature measures for a better comparison of the gradients.

4.3.2 Spatially Distributed Measurements in the Horizontal Pattern

The horizontal pattern for the convective case took place at 50 m AGL between 2021-07-02 15:13:45 and 2021-07-02 15:27:15 UTC with an orientation of the x -axis towards 290° (Fig. B.2a). Timeseries of the sonic and the two nearest UAVs can be found in the Appendix (Fig. B.3). Stationarity can be assumed during the flight (Tab. 4.4).

Excluding UAV #7, the interpretation of the results is analogous to the neutral case (sec. 4.2.2): Without UAV #7, all variables fulfil the (quasi-)homogeneity test (Tab. 4.5) and standard deviations of the spatially distributed UAV measures are below the measurement accuracy (Tab. 4.1). However, UAV #7 shows deviations from the other quadrotors for all variables (Fig. B.2) resulting in higher values of

the standard deviations (Tab. 4.5). Furthermore, the (quasi-)homogeneity test for the horizontal covariance fails at a threshold of 30%.

Of course, this may be due to exceptional behaviour of this specific UAV under the prevailing conditions. But on the other hand, UAV #7 has a special position in the pattern, namely it is at the border where the underlying surface changes from corn- to grassland (Fig. B.2a), which may have an influence. That finding will be discussed in more detail in chapter 5.

Table 4.4: (Quasi-)stationarity test after equation (3.14) for the convective case on 2021-07-02. Stationarity is assumed for values below 30%.

Variable	sonic	UAV #11
$\overline{u'^2}$	11%	6%
$\overline{v'^2}$	3%	2%
$\overline{u'v'}$	15%	11%

Table 4.5: Standard deviation σ_{UAV} of the spatially distributed UAV measurements and (quasi-)homogeneity test HT after equation (3.16) for the convective case on 2021-07-02. Shown are values including UAV #7 and values without that vehicle.

Variable	σ_{UAV}	HT	$\sigma_{\text{UAV}} \setminus \#7$	$HT \setminus \#7$
\bar{u}	0.17 m s^{-1}	3%	0.14 m s^{-1}	2%
\bar{dd}	3.6°	–	2.1°	–
$\overline{u'^2}$	$0.12 \text{ m}^2 \text{ s}^{-2}$	12%	$0.11 \text{ m}^2 \text{ s}^{-2}$	10%
$\overline{v'^2}$	$0.15 \text{ m}^2 \text{ s}^{-2}$	14%	$0.11 \text{ m}^2 \text{ s}^{-2}$	11%
$\overline{u'v'}$	$0.09 \text{ m}^2 \text{ s}^{-2}$	53%	$0.04 \text{ m}^2 \text{ s}^{-2}$	26%

4.3.3 Power Spectra

Figure 4.11 shows filtered and unfiltered power spectral densities for the convective case. As for the neutral case (sec. 4.2.3), the unfiltered UAV spectra start to deviate from Kolmogorov's law at a certain frequency attributed to internal sensor noise. Here, this deviation starts at around 0.8 Hz. Thus, when using filtered 1 Hz data, the contribution from 0.8 Hz to 1 Hz leads to an overestimation of the variance. However, the relative deviations of variances calculated with cut-off frequencies of 0.8 Hz and 1 Hz are less than 0.5%. Therefore, the used cut-off frequency of 1 Hz is appropriate and causes no great systematic error.

A greater systematic error results from neglecting the contribution between 1 Hz and 20 Hz. Estimated by comparing filtered and unfiltered sonic data, this leads to an underestimation of around 2% for the streamwise variance.

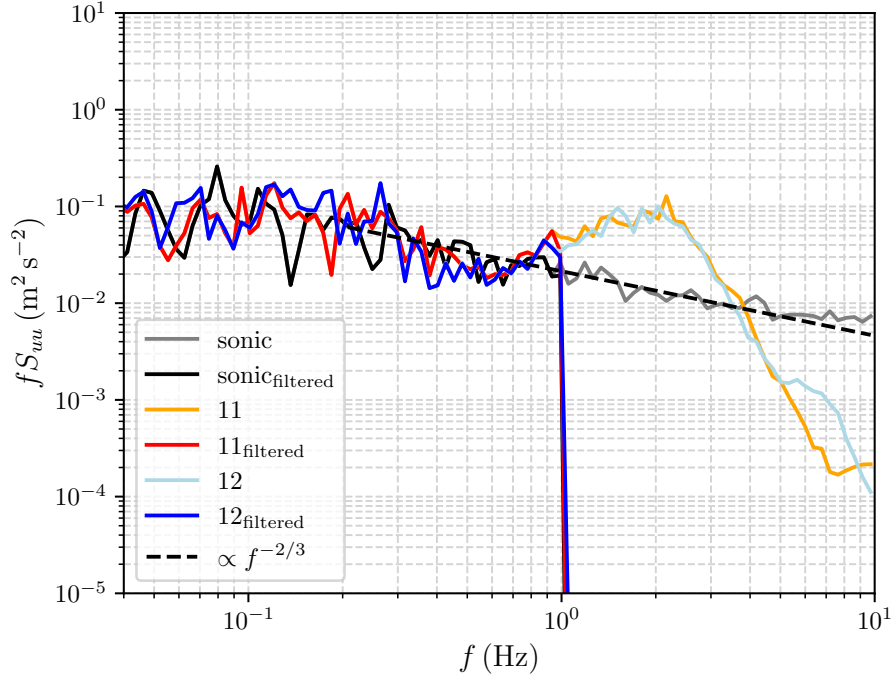


Figure 4.11: Power spectral densities multiplied by frequency of streamwise velocity for the convective case on 2021-07-02. Shown are unfiltered and filtered spectra for the sonic and the two nearest UAVs #11 and #12.

4.3.4 Cross-correlation and Coherence

For this case, no clear global correlation maximum can be identified for large separation distances Δx (e.g., $\Delta x = 205$ m in Fig. B.4a). Therefore, the local correlation maxima in the range ± 5 s around the expected time lag (eq. (3.19)) have been used to derive the maxima shown in Figure B.5a. These maxima of the cross-correlation function (Fig. B.5a) decrease with distance much faster than for the neutral case, e.g., the correlation maximum for the neutral case was 0.79 for $\Delta x = 125$ m, whereas here it is only 0.51 for the same distance.

One reason for this may be the fact that the deviation between the pattern alignment and the measured mean wind direction was around 15° . Therefore, the displacements (eq. (3.18)) for this case are much larger than for the neutral case, which have a significant influence (Fig. B.5b). On the other hand, the stability, the average wind speed, and the height above the ground also differ between the two cases. But the turbulence intensities are comparable. For this case, it is 0.18.

Further, the coherence values are lower (Fig. B.6) than for the neutral case (Fig. 4.9) for a fixed frequency. Note, however, that for the resolved frequencies, the corresponding eddy sizes are smaller than for the neutral case due to the smaller mean wind speed.

4.4 Stable Boundary Layer

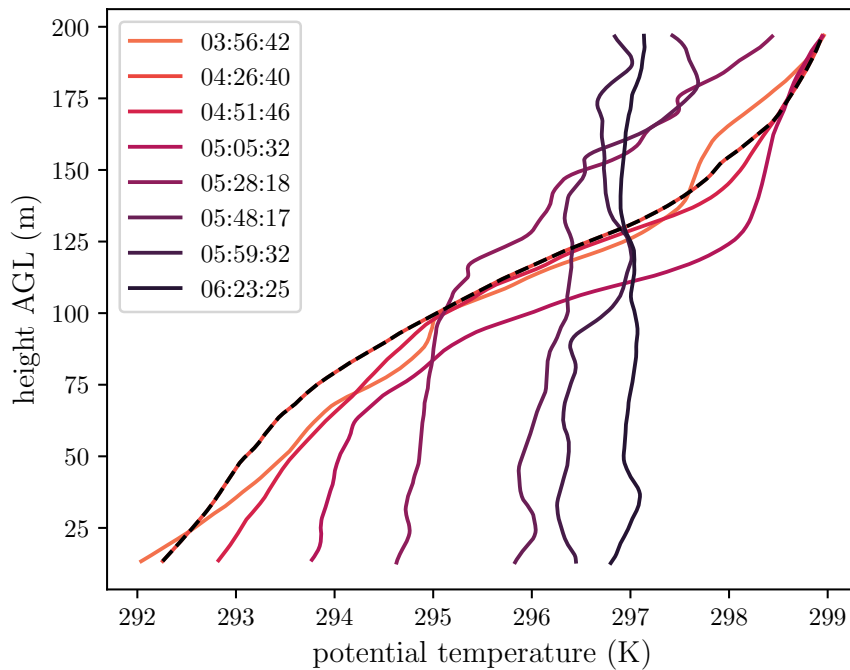
4.4.1 Atmospheric Conditions

On 2021-06-29, the measurement site was located downstream of the weather system that was responsible for the situation on 2021-06-30 (sec. 4.2.1). No low level clouds were present during the night, so the surface cooled down and a stable layer formed with a strong potential temperature gradient near the surface (Fig. C.1c and 4.12a). Further a low-level jet formed with a strong vertical wind speed gradient (Fig. C.1d and 4.12b).

In the afternoon, a convergence line caused the formation of a convective system. Although the main part of the system did not directly cross the site, the associated gust front reached it and caused a significant drop in temperature (Fig. C.1c), strong increase in turbulent kinetic energy (Fig. C.1b) and wind speed (Fig. C.1d) and some light rain (Fig. C.1e).

The analysed horizontal flight pattern was performed during the stable phase in the morning. Several vertical profiles have been conducted during and after this flight (Fig. 4.12). Figure 4.12a illustrates the warming from the ground and the transition from the stable boundary layer into the daytime convective boundary layer. During this transition, vertical mixing causes the decay of the low-level jet (Fig. 4.12b). Despite the strong vertical wind shear during the flight, the strong thermal stratification suppressed the turbulence and thus the turbulence intensity was only 0.04.

(a)



(b)

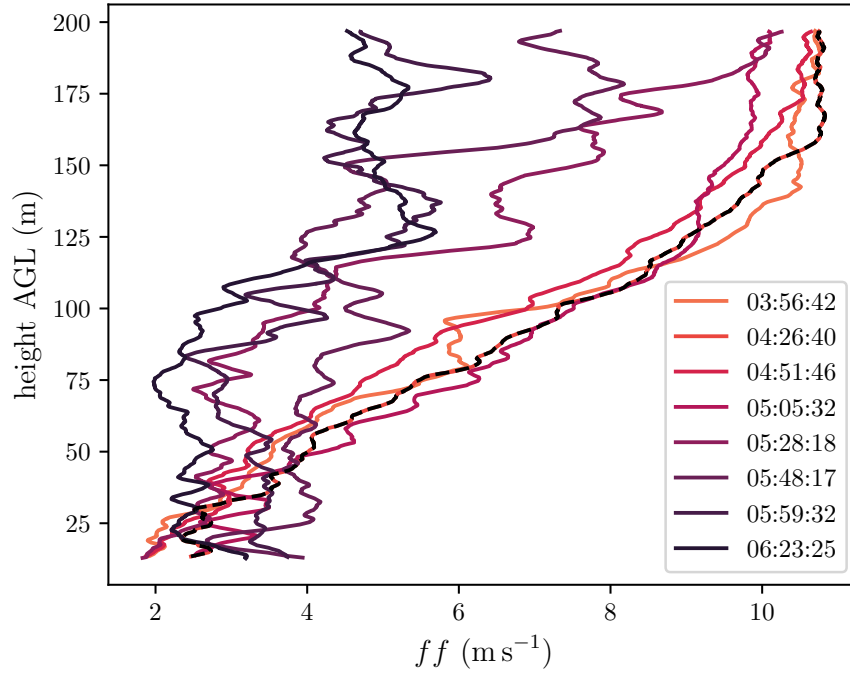


Figure 4.12: UAV vertical profiles of (a) potential temperature and (b) wind speed for the stable case on 2021-06-29. Shown are moving averages of 5 s. The labels indicate the beginning of the vertical profiles. The dotted black curves with start time at 04:26:40 UTC correspond to the profile during the horizontal pattern.

4.4.2 Spatially Distributed Measurements in the Horizontal Pattern

During the morning transition, the horizontal pattern was operated in a continuous mode at 90 m AGL with the orientation of the x -axis towards 150° . For that, the UAVs were replaced twice so that continuous measurements of 40 min were realised (Fig. 4.13). For a better comparison, however, only one of the three individual flights is evaluated. Chosen is the last one, because here almost the same UAVs were used as for the other two case studies. This is also true for the first one, but there the stationarity test failed, while stationarity can be assumed for the last one (Tab. 4.6). During the selected flight, UAV #9 had some problems and therefore it does not appear in the analysis. The selected flight started at 04:22:44 UTC and ended at 04:36:22 UTC.

Inspection of the calibration results show that the deviations of the variances for low values are smaller than the overall root mean square errors (Tab. 4.1). Therefore, the root mean square errors were recalculated for ranges with small variances (Tab. 4.7) to achieve a meaningful estimate of the measurement uncertainties

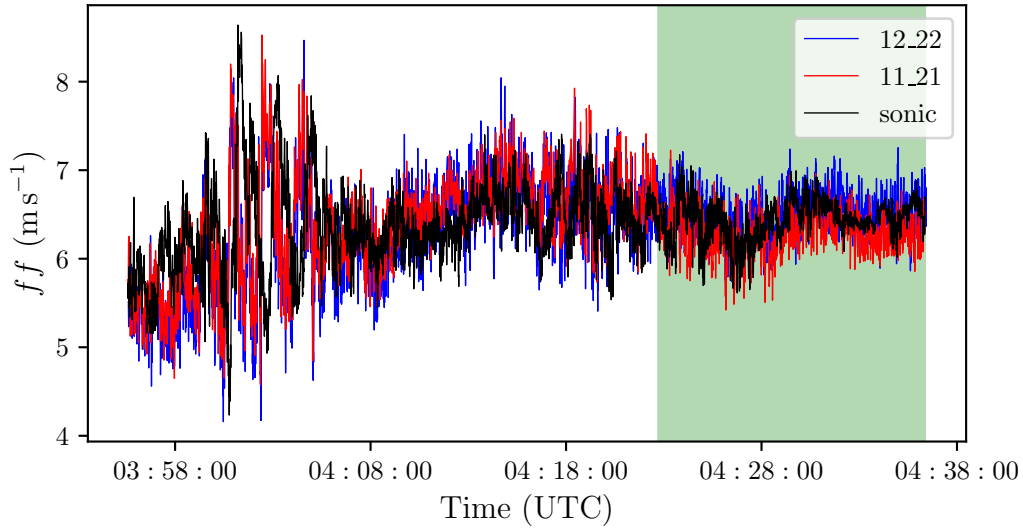


Figure 4.13: Time series of wind speed for the stable case on 2021-06-29. Shown are series of the sonic and the combined series of the UAVs #11_21 and #12_22. The green rectangle indicates the evaluated flight.

for cases with low turbulence. A similar calculation of root mean square errors for selected ranges around the measured values for the neutral and convective case showed that these errors are very similar to the deviations listed in Table 4.1. This means that, apart from cases with low turbulence, the values listed in Table 4.1 are a good estimate of the measurement uncertainties.

Mean wind speed and mean wind direction are well captured by the UAVs (Fig. C.2). However, the magnitudes of the (co-)variances (Fig. C.2) are smaller than the measurement accuracies inferred from Table 4.7 and thus the (co-)variances are not resolvable by the UAVs in a meaningful way for this case. The UAVs overestimate the very low variances (Fig. C.2d and C.2e) with relative deviations from the sonic up to more than 100%. At a threshold value of 30%, the homogeneity test (eq. (3.16)) fails for the streamwise variance and the horizontal covariance (Tab. 4.8). But the calculated standard deviations (Tab. 4.8) lie below the measurement accuracies (Tab. 4.7). Thus, possible inhomogeneities are masked by the measurement accuracies and the failure of the homogeneity tests might be attributed to the variability caused by measurement noise.

Table 4.6: (Quasi-)stationarity test after equation (3.14) for the stable case on 2021-06-29. Stationarity is assumed for values below 30%.

Variable	sonic	UAV #11
$\overline{u'^2}$	14%	15%
$\overline{v'^2}$	16%	16%
$\overline{u'v'}$	21%	28%

Table 4.7: Recalculation of root mean square errors for the calibration flights for low (co-)variance values. The limits refer to sonic data.

Variable	σ_{RMS}
$\overline{u'^2} < 0.5 \text{ m}^2 \text{ s}^{-2}$	$0.05 \text{ m}^2 \text{ s}^{-2}$
$\overline{v'^2} < 0.5 \text{ m}^2 \text{ s}^{-2}$	$0.06 \text{ m}^2 \text{ s}^{-2}$
$-0.05 \text{ m}^2 \text{ s}^{-2} < \overline{u'v'} < 0.05 \text{ m}^2 \text{ s}^{-2}$	$0.07 \text{ m}^2 \text{ s}^{-2}$

Table 4.8: Standard deviation σ_{UAV} of spatially distributed UAV measurements and (quasi-)homogeneity test HT after equation (3.16) for the stable case on 2021-06-29.

Variable	σ_{UAV}	HT
\overline{u}	0.21 m s^{-1}	3%
\overline{dd}	3.3°	—
$\overline{u'^2}$	$0.03 \text{ m}^2 \text{ s}^{-2}$	44%
$\overline{v'^2}$	$0.02 \text{ m}^2 \text{ s}^{-2}$	26%
$\overline{u'v'}$	$0.01 \text{ m}^2 \text{ s}^{-2}$	35%

4.4.3 Power Spectra

Compared to the spectra of the other two cases (Fig. 4.6 and 4.11), the absolute height of the spectra in Figure 4.14 is significantly lower, reflecting the low turbulence during this flight. Furthermore, to the left of about 0.1 Hz, both the spectra of the sonic and the UAVs drop. This indicates that the largest energy-carrying eddies are on the order of 0.1 Hz, which corresponds to a wavelength of about 60 m.

The spectra clearly show the overestimation of the UAVs for the lower frequencies (Fig 4.14). There is only a small frequency range, where the spectra match reasonably well (0.3-0.8 Hz).

Comparing filtered and unfiltered sonic data, the underestimation of the stream-wise variance is around 10% if a cut-off frequency of 1 Hz is used. Note, however, that the sonic deviates strongly from the theoretical Kolmogorov law for the higher frequencies.

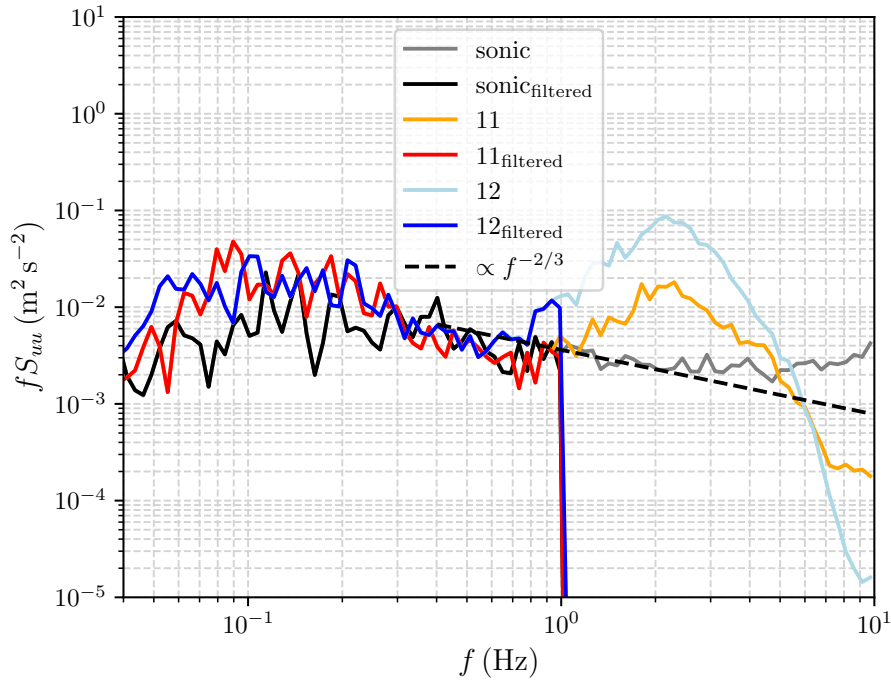


Figure 4.14: Power spectral densities multiplied by frequency of streamwise velocity for the stable case on 2021-06-29. Shown are unfiltered and filtered spectra of the sonic and the two UAVs #11 and #12.

4.4.4 Cross-correlation and Coherence

For distances more than 15 m no global maximum can be identified in the cross-correlations (Fig. C.3). Therefore, as for the convective case (sec. 4.3.4), local correlation maxima in the range ± 5 s around the expected time lag (eq. (3.19)) have been inferred to derive Figure C.4a. In contrast to the convective case, however, where no clear peak but a broad maximum around the theoretical time delay was observed (Fig. B.4a), the curves here are pretty much flat for large distances (Fig. C.3). Therefore, it is difficult to determine a correlation maximum at all, and it is questionable how meaningful the used approach is.

The correlation maxima determined by this approach show a rapid decay with distance. Similarly, the coherence strongly decreases with distance and scale (Fig. C.5). On the one hand, these observations are likely due to the strong measurement noise. On the other hand, it seems reasonable that the eddies exhibit weak coherence since they contain low energy.

Chapter 5

Discussion

In chapter 4 three case studies have been presented separately. The most important results are compared and discussed in more detail in this chapter. Furthermore, the chapter will serve to comment on the potential and limitations of the UAV fleet and the applied methods for atmospheric boundary layer research.

5.1 Applicability of UAV Measurements for Studying Turbulence in the Atmospheric Boundary Layer

The results of chapter 4 show that the measurement system consisting of 34 UAVs can not only reasonably capture the mean wind field but also turbulence with the overall estimated accuracies summarized in Table 4.1. But the fleet reaches its limitations due to sensor noise when dealing with low turbulence flows (sec. 4.4).

A joint representation of the power spectra (Fig. 5.1) illustrates the low energy contained in the turbulent flow of the stable case. Furthermore, it becomes clear again that the frequency filter of 1 Hz is appropriate since the UAV spectra for all three cases deviate from Kolmogorov's law at the higher frequencies attributed to sensor noise. Neglecting the range between 1–20 Hz leads only to small systematic errors for the neutral (sec. 4.2.3) and convective case (sec. 4.3.3). In stable boundary layer flows with low turbulence and small eddies, the small-scale turbulence is of much more importance. These, however, cannot be resolved with the UAVs due to the measurement noise.

For stable situations with small eddies, the runtime of the battery would be sufficient to resolve all relevant scales (sec. 4.4.3). For the neutral and convective case, it is questionable whether the measurement duration of around 13.5 min was sufficient to capture all relevant scales of the turbulent flow and if the time average

reflects the ensemble mean (eq. (2.7)). The neglect of larger scales due to the limited measurement duration did not pose a problem for the analysis of coherence and cross-correlation in the studied microscale (sec. 4.2.4 and Fig. A.1). But for larger measuring distances or other applications, this may have an impact. Although more extended measuring periods have been achieved by replacing the UAVs, this shows another limitation of the UAV fleet: It is helpful for case studies, but it is not suitable for long-term observations.

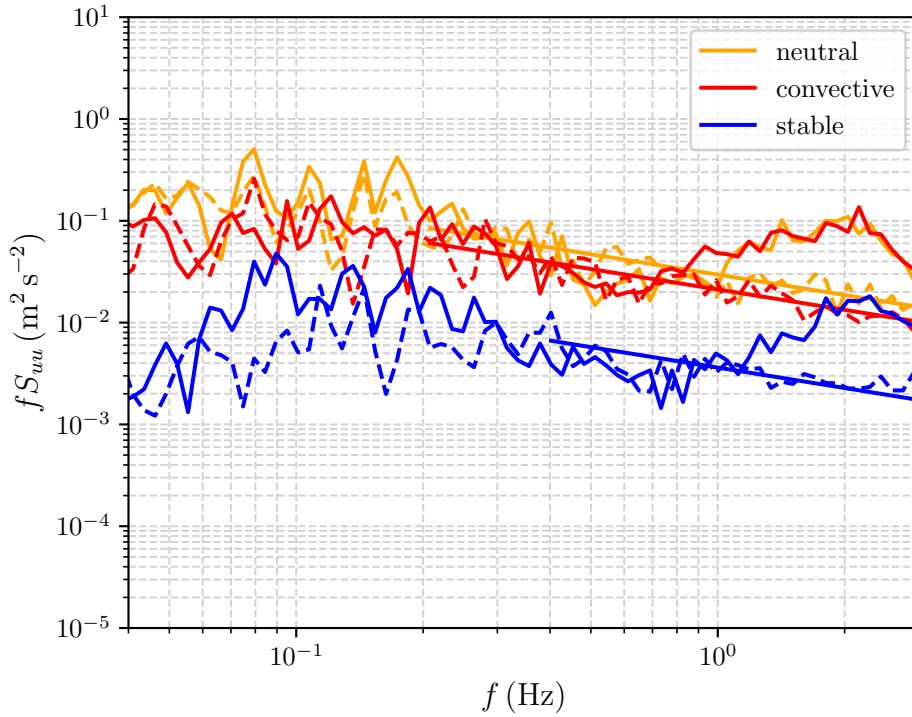


Figure 5.1: Unfiltered power spectral densities multiplied by frequency of streamwise velocity for the neutral, convective and stable case. Solid lines corresponds to UAV #11 and dotted lines to sonic anemometer measures. Further, Kolomogorov's law (eq. (2.9)) is indicated for the three cases.

5.2 Determining Correlation and Coherence with the Horizontal Pattern

The orientation of the horizontal measurement pattern along the mean wind direction was intended to mimic the usual decomposition of the turbulent wind field into streamwise and lateral directions already in the experimental setup. With the help of the spatially distributed UAVs in the streamwise direction, the development of a turbulent structure during advection can be tracked. Further, analysis as a function of different spatial separations is possible due to varying distances between

neighbouring UAVs. One of the main objectives within this thesis was to investigate cross-correlation and coherence in the streamwise direction and thereby examine the Taylor hypothesis. Although not addressed in this work, this measurement setup could also be used to directly calculate structure functions or turbulence length scales without the need to convert temporal differences into spatial distances (eq. (2.10)) under the assumption of Taylor's hypothesis.

In principle, this setup is well suited for investigating spatial correlations and coherences (sec. 4.2.4, 4.3.4 and 4.4.4). Yet there is a main limitation mentioned several times in chapter 4: Since the mean wind direction during the flight cannot be determined in advance and can only be estimated from previous measurements, misalignments occurred that have a crucial influence on the results. E.g., for pattern misalignments on the order of 15° , which were present for the convective and stable case, the displacement after equation (3.18) is around 50 m for $\Delta x = 200$ m. That this displacement has a significant impact can be seen, e.g., in Figure B.5b. For $\Delta x = 75$ m and a very small total displacement of approx. 1 m, the cross-correlation is 0.68, whereas for a total displacement of approx. 54 m it is only 0.21. Apart from this example, as pointed out in section 4.2.4, there is no general approach to deduce values for correlation and coherence for a theoretically perfect alignment from the measurements with displacement. Thus, this uncertainty persists in the results and one has to think about improvements of the measurement strategy in future campaigns (chap. 6).

5.3 Spatial Correlation and Coherence for Different Atmospheric Conditions

The idea of totally frozen turbulence transported by the mean wind does not reflect the true nature of turbulent flows. In fact, turbulence is dissipative and energy is transferred from larger to smaller eddies (sec. 2.3). Thus eddies evolve and change their shape during the advection time.

Deviations from unity of the coherence and consequently of the cross-correlation in streamwise direction have already been studied earlier by Pielke and Panofsky (1970), Panofsky and Mizuno (1975) and Schlez and Infield (1998). They suggested an exponential decay of longitudinal coherence with the semi-empirical formula

$$\gamma^2 = \exp\left(-\alpha \frac{\sigma_u}{\bar{u}} \frac{f \Delta x}{\bar{u}}\right) = \exp\left(-\alpha \frac{\sigma_u}{\bar{u}} \frac{\Delta x}{\lambda}\right) . \quad (5.1)$$

Here, α is called a decay constant and it accounts for eddy decay during the advection time. For neutral stratification a value of $\alpha = 30 \pm 10$ is suggested (Schlez and Infield 1998). According to equation (5.1), loss of coherence depends on the constant α ,

turbulence intensity σ_u/\bar{u} , separation distance Δx and eddy scale λ .

Strictly, equation (5.1) was suggested for the coherence along a Lagrangian trajectory (Panofsky and Mizuno 1975). When considering the loss of coherence along the mean wind direction instead of along the actual trajectory, lateral diffusion caused by wind direction fluctuations should be included as an additional term in the exponential decay. This diffusion has more impact on stable conditions (Panofsky and Mizuno 1975).

The semi-empirical formula (eq. (5.1)) reflects the findings in the sections 4.2.4 and 4.3.4: Coherence decreases with decreasing scale and/or increasing distance. The small eddies evolve faster and are mainly responsible for the decrease in cross-correlation for small separation distances. With increasing distance, the evolution of larger eddies more and more contribute to this decay.

After equation (5.1), the coherence value should be the same for cases with fixed turbulence intensity, separation distance and wavelength if the constant α is universal, i.e., independent of other conditions such as stability or measurement height. To investigate if α is universal, the coherence curves for a separation distance of $\Delta x = 5$ m are reconciled in Figure 5.2 as a function of wavelength. The distance of 5 m was chosen so that the displacement should not have a significant influence. Since the turbulence intensities for the neutral and convective case are comparable (0.16 and 0.18), the corresponding coherence curves should look similar for a universal α . However, the curve for the convective case falls more rapidly than for the neutral case. Accordingly, fits after equation (5.1) yield a decay constant $\alpha_{\text{neut}} = 15$ for the neutral and $\alpha_{\text{conv}} = 29$ for the convective case. These two values are within or close to the value range $\alpha = 30 \pm 10$.

The different decay constants may hint that coherence in convective boundary layers might generally be lower than in neutral boundary layers. Buoyancy-driven turbulence might lead to a more considerable mixing, resulting in lower coherence values. In addition, the measurement height possibly also has an influence. For the convective case, the pattern was at 50 m, while for the neutral case it was at 90 m. Closer to the ground, the eddies become smaller, which, as shown, generally have lower coherence values. In particular, the results also indicate that the applicability of the Taylor hypothesis might not only depend on the turbulence intensity as the simple rule of thumb suggests (eq. (2.12)).

The decay constant $\alpha_{\text{stab}} = 763$ for the stable case is much larger than for the other two cases. One reason for this is that equation (5.1) is not directly applicable for stable stratifications (Panofsky and Mizuno 1975). Furthermore, the significant measurement noise for low turbulence conditions plays a role, which is somehow included in the constant. Moreover, it is questionable how meaningful the coherence values are for the depicted larger scales since the largest energy-carrying eddies are

relatively small for the stable case (sec. 4.4.3).

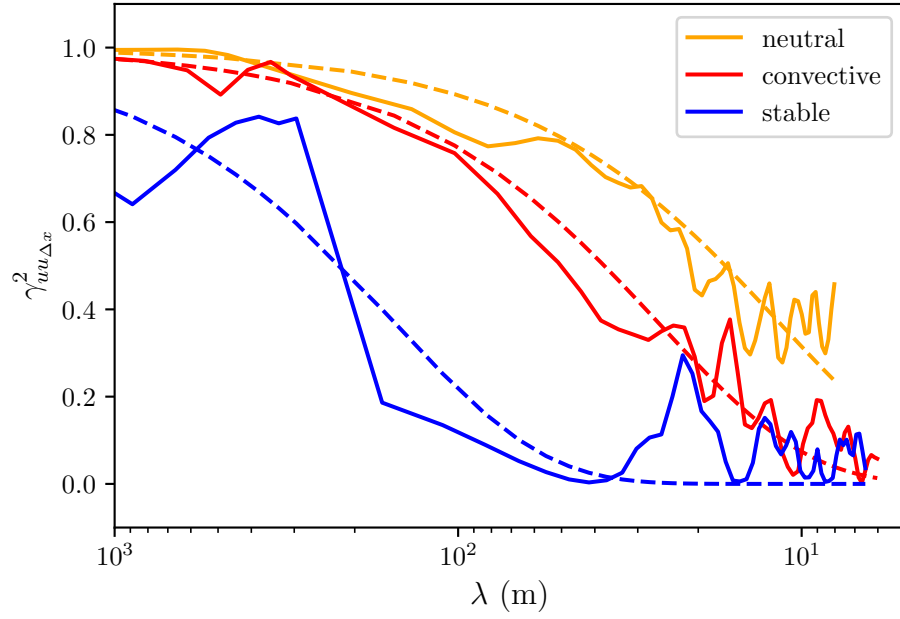


Figure 5.2: Measured coherence of streamwise velocity as function of wavelength λ for the neutral, convective and stable case (solid lines) with fixed separation distance $\Delta x = 5$ m. Dotted lines are fits after equation (5.1) with $\alpha_{\text{neut}} = 15$, $\alpha_{\text{conv}} = 29$ and $\alpha_{\text{stab}} = 763$.

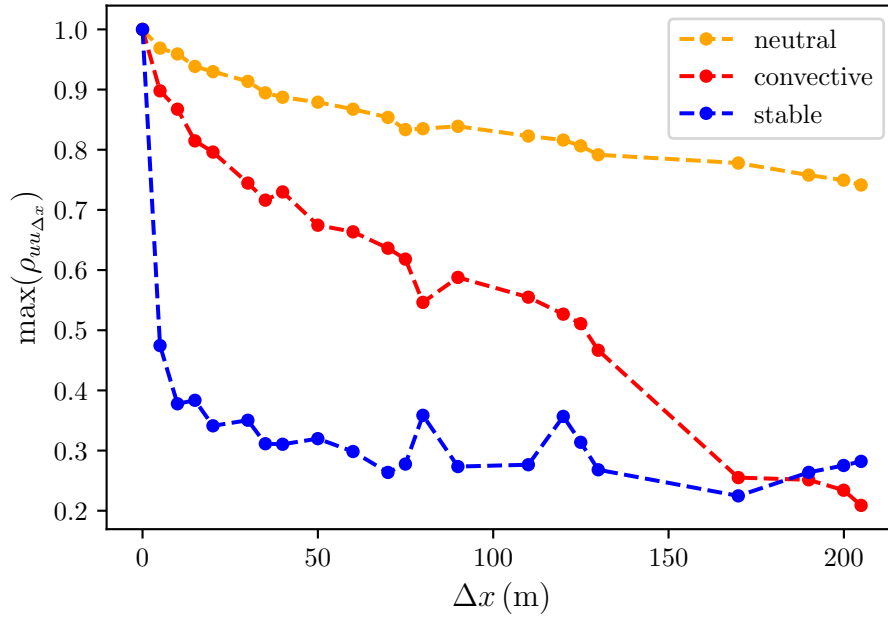


Figure 5.3: Maxima of cross-correlation function of streamwise velocity as function of distance Δx for the neutral, convective and stable case.

The different decreasing coherences also directly affect the cross-correlations (Fig. 5.3). It should be noted, however, that in addition to the measurement noise, the increasing displacement also contributes significantly to the decay for large separation distances in this plot. In particular, the strong drop of the last four values of the convective case might be attributed to this displacement.

When inferring information on the spatial structure of turbulence with a single measurement device using Taylor’s frozen turbulence hypothesis, the eddies have to maintain their shape to a certain degree while passing the sensor. Here, different time scales are required for eddies of different sizes. Obviously, smaller eddies have to retain their shape for a shorter time than larger ones in order to be resolved by a single sensor.

This means that for an eddy of size λ , which equals a separation distance of two sensors $\Delta x (= \bar{u}\Delta t)$, the calculated coherence $\gamma_{uu\Delta x}^2(\lambda)$ measures the persistence during the advection. Following this idea, Higgins et al. (2012) used Raman lidar data and wavelet decompositions to investigate the dependency of Taylor’s hypothesis on the different scales. For calculated autocorrelations along the Lagrangian path for different wavelet composites, they set an arbitrary persistence threshold of 20% for which they accepted the applicability of the Taylor Hypothesis.

Using the same threshold of 20% as Higgins et al. (2012) for the calculated coherences, this is hardly fulfilled for the conditions $\lambda = \Delta x$ (Fig. 4.9, B.6 and C.5). However, the measurement uncertainties and lateral displacement already mentioned several times must be taken into account, which are partly responsible for the decline of coherence. Further the chosen threshold is arbitrary and it is application dependent, how severe restrictions have to be made about the persistence of a turbulent structure during its passage past a single sensor.

5.4 Homogeneity in the Microscale

Surface heterogeneities of the relatively flat terrain around GM Falkenberg have been extensively investigated during the LITFASS experiments (e.g., Beyrich et al. 2002; Platis et al. 2017). Significant differences in turbulent fluxes were found dependent on the main land use classes (Beyrich et al. 2002). However, the dimensions studied were much larger than the ones explored here, e.g., during the LITFASS-98 experiment a mesoscale area of around 20 km \times 20 km was considered (Beyrich et al. 2002).

In this work, the homogeneity assumption is investigated on the microscale with a maximum separation of 205 m between two vehicles. For a quantitative analysis, a homogeneity test was proposed. It should be mentioned again that the suggested threshold of 30%, below which homogeneity is assumed, was set arbitrarily. If this

limit is appropriate has to be further investigated in the future.

Taking this threshold and considering the measurement accuracy, it was argued that there is no significant sign for the violation of the homogeneity assumption in the microscale. Only the measures of UAV #7 for the convective case (sec. 4.3.2) show deviations from the other vehicles for all examined variables. Of course this can be caused by general issues of the vehicle. The few calibration flights available for this vehicle, however, do not show significant deviations from the other vehicles except for the wind direction, which is systematically underestimated (Fig. 4.1b). This underestimation has been observed also for the near neutral case (Fig. 4.4c). All other quantities seem to be consistent with the other vehicles. Thus a general problem of UAV #7 does not appear to be present and therefore the deviation might possibly have physical reasons.

UAV #7 is located on the edge, where the surface changes from corn- to grass-land (Fig. B.2a). Changes in the roughness length or in the thermal properties of the underlying surface can cause the formation of Internal Boundary Layers (Foken 2016) downstream of the transition. However, as vehicle #7 is directly located at the transition, the measurement at 50 m should be only influenced by the upstream conditions. Therefore it could be that UAV #7 has a different footprint than the other vehicles due to its location in the pattern. Though, estimated footprints and corresponding landcover classifications after Kljun et al. (2015) for the different positions in the pattern do not show considerable differences due to the small scale of the measurement pattern compared to the length and width (Fig. 5.4) of the footprints. Furthermore, the recorded temperature values of the vehicles aligned in the y -direction of the pattern show no significant deviations of vehicle #7 (Fig. 5.5). If the underlying surface had an influence, one might expect that this would be reflected not only in the wind measurements but also in the temperature data.

This means that it remains rather an unresolved question what explains the observed deviations of vehicle #7 and further investigations would be needed for drawing significant conclusions. Still, the considerations presented here can serve as a guideline for such studies in the future.

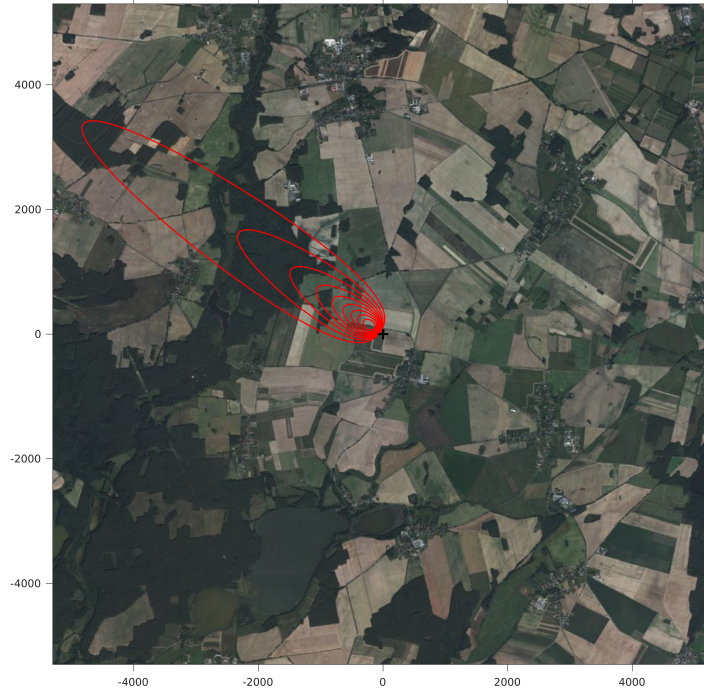


Figure 5.4: Estimated footprint after Kljun et al. (2015) for the sonic anemometer for the convective case on 2021-07-02 calculated with the measurement height $z_m = 50$ m, the zero-displacement height $d = 0.1$ m, the mean wind speed $\bar{u} = 6 \text{ m s}^{-1}$, Obukhov length $L = -40$ m, standard deviation of lateral velocity fluctuations $\sigma_v = 1.1 \text{ m s}^{-1}$, friction velocity $u_* = 0.38 \text{ m s}^{-1}$ and mean wind direction $dd = 305^\circ$. Shown are contour lines in steps of 10%. Units of the axis labels are in meters.

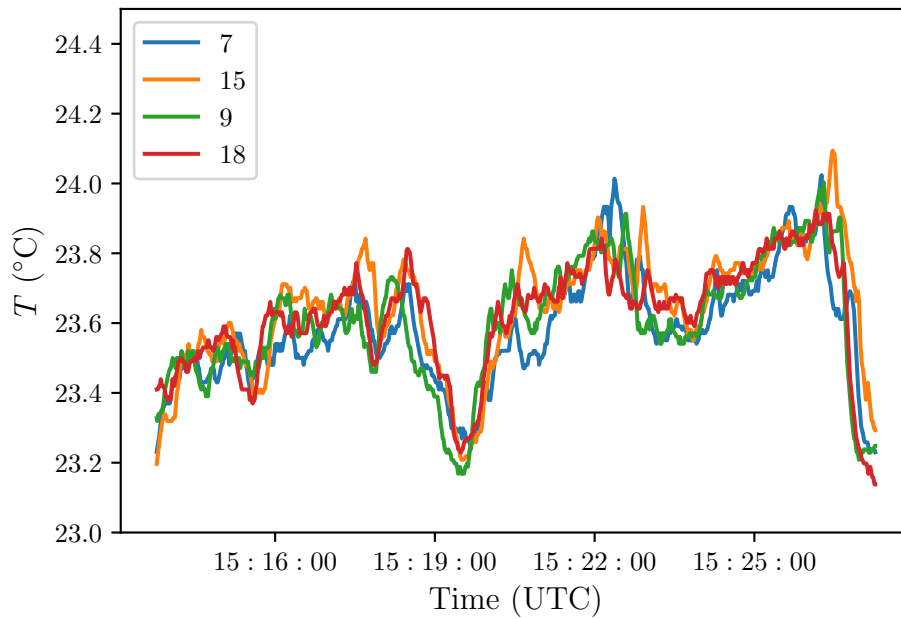


Figure 5.5: Measured temperatures of the UAVs aligned in the y -direction of the horizontal pattern for the convective case on 2021-07-02.

Chapter 6

Conclusions and Outlook

Internal sensor noise of the UAVs prevents capturing of low turbulence flows associated with stable boundary layers (sec. 4.4). Two selected examples showed that the UAVs can reasonably resolve the turbulence up to a resolution of 1 Hz for moderate turbulence intensities with the algorithm used within this work (sec. 4.2.3 and 4.3.3).

Within the measurement accuracy, there was no significant sign evident that the homogeneity assumption is violated in a relatively flat terrain for the microscale between 5 m and 205 m (sec. 4.2.2, 4.3.2, 4.4.2 and 5.4). The same studies could be conducted for larger distances in such terrains in the future. The UAV fleet might help to detect possible surface heterogeneities that are noticeable only on larger scales. The measures of the fleet might then reflect the turbulent wind field more realistically than a single point measurement. This also holds for complex terrain, where the UAVs can provide a relatively easy access for spatially distributed measurements.

Furthermore, it became apparent that the fleet is well suited for studying cross-correlation and coherence. Decreases of cross-correlations and coherences (sec. 4.2.4, 4.3.4 and 4.4.4) indicated the limited applicability of Taylor’s frozen turbulence hypothesis. The discussion in section 5.3 leads to the idea of investigating the decreases in cross-correlations and coherences as a function of different turbulence intensities and stabilities in more detail in future studies. Moreover, such coherence studies could be performed not only for basic atmospheric boundary layer research but also for applied research. An example of this would be the study of wake vortices of wind turbines.

It turned out that, apart from the measurement noise, the main limitation was the misalignment of the horizontal pattern with the mean wind direction. Therefore, in future studies, one could arrange the UAVs not only in one line according to the last measured wind direction but in several lines with slightly different orientations or in a grid-like pattern. In these setups, it should be ensured that there is always

a line along which the displacements are small. Moreover, as an other idea, more complex flight plans could be created allowing the UAVs to adapt the pattern to the wind direction during the flight.

It was shown that the averaging time of around 14 min is sufficient for the dimension of the horizontal measurement pattern for investigating cross-correlation and coherence (sec. 4.2.4). However, resolving larger scales in possible future campaigns would need also longer averaging times. This has already been realised in the field by exchanging the UAVs.

The wind algorithm was further developed during the writing of this thesis and now includes acceleration terms as a correction for deviations from the hover state, which offers a meaningful turbulence resolution up to 2 Hz ([Wetz and Wildmann 2022](#)). The algorithm will be extended to include the vertical wind component as a future goal. Then, also turbulent vertical fluxes can be obtained at spatially separated points.

Appendix A

Near Neutral

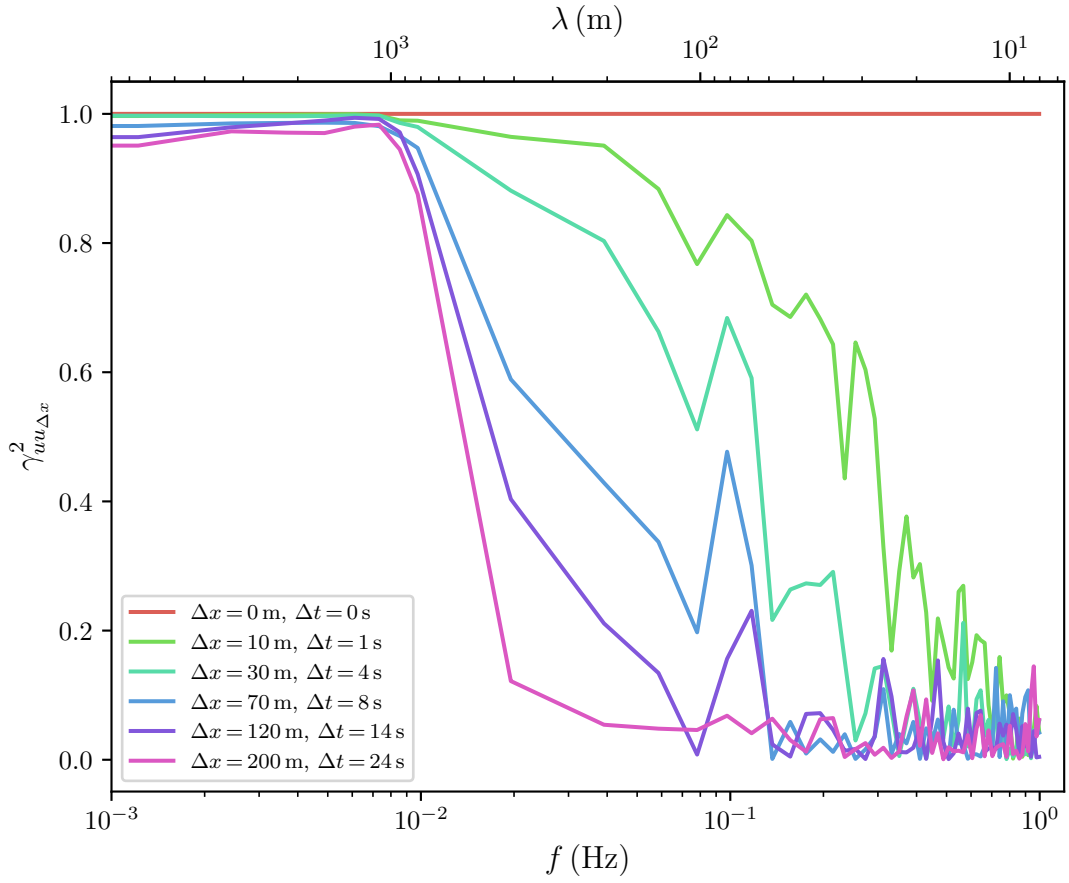
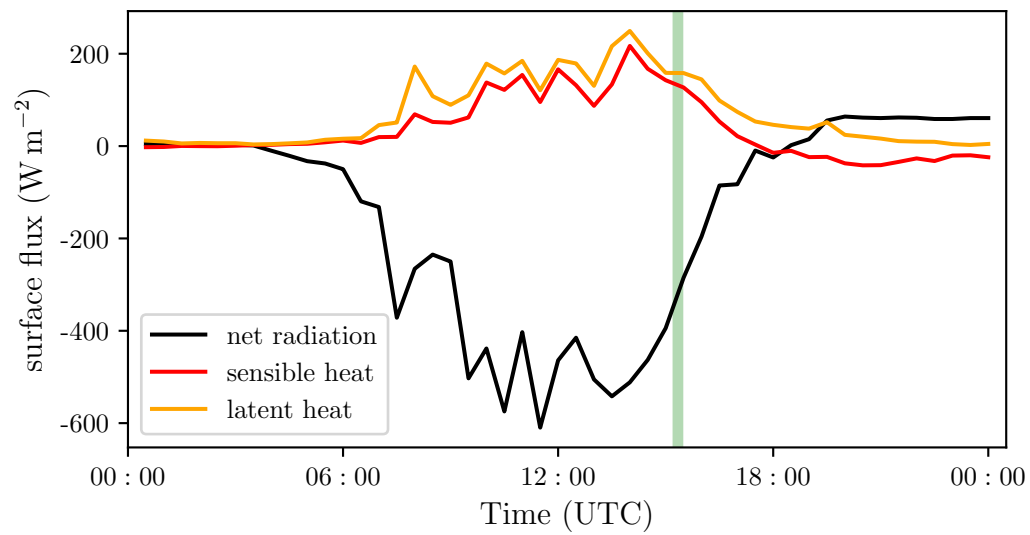


Figure A.1: Coherence of streamwise velocity for different spatial distances Δx or equivalent evolution time Δt (eq. (3.19)) for the near neutral case on 2021-06-30. Here, x is the fixed position of the combined vehicles #12.22. Frequencies have been converted to wavelengths after equation (2.11) (top axis).

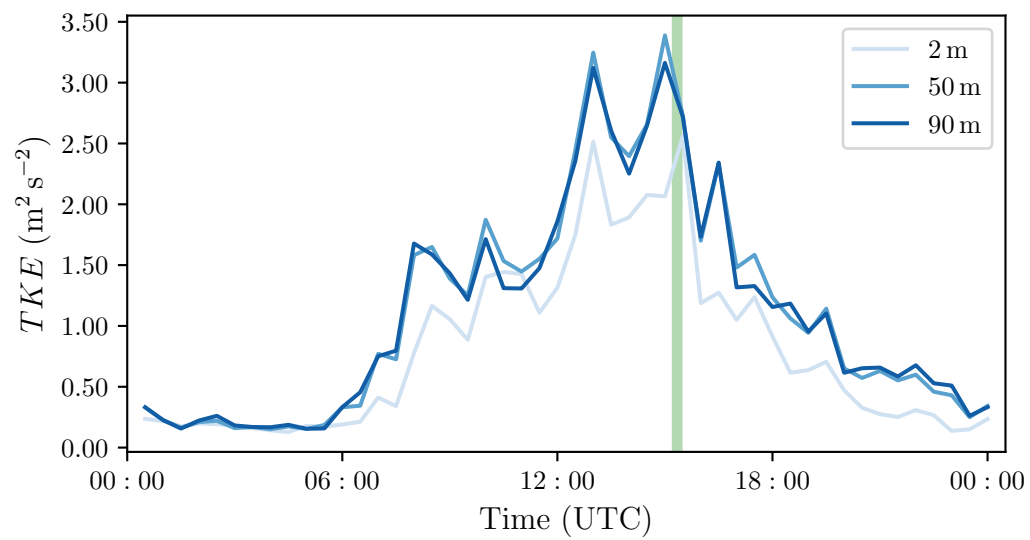
Appendix B

Convective

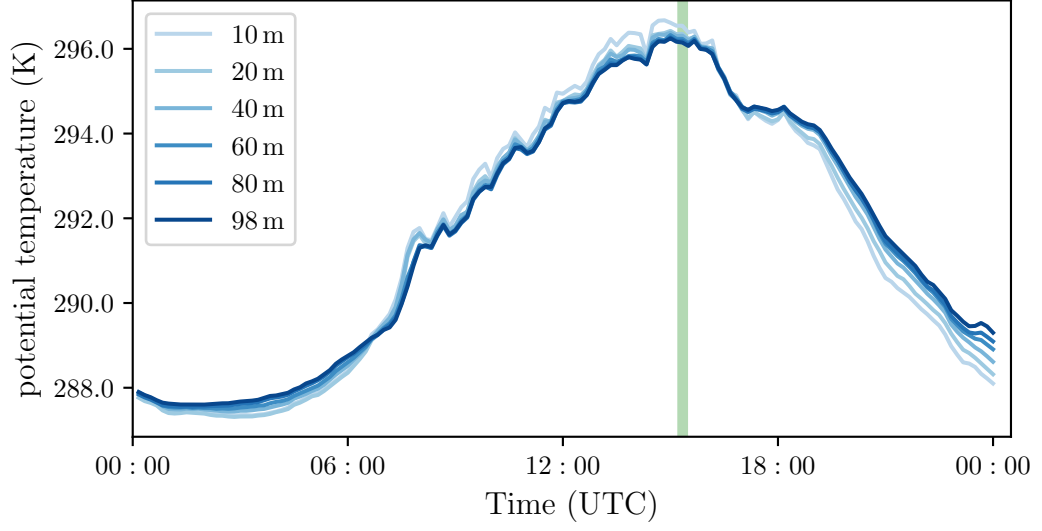
(a)



(b)



(c)



(d)

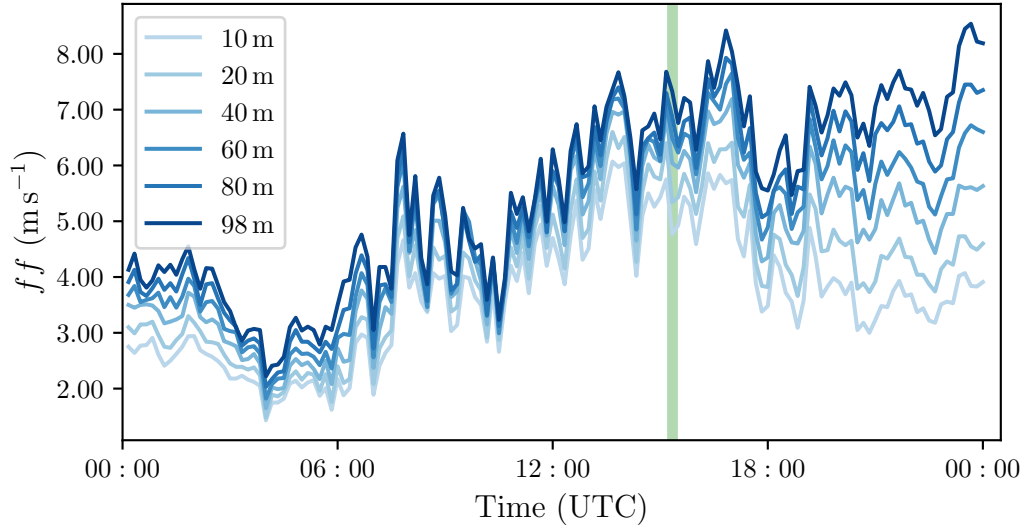
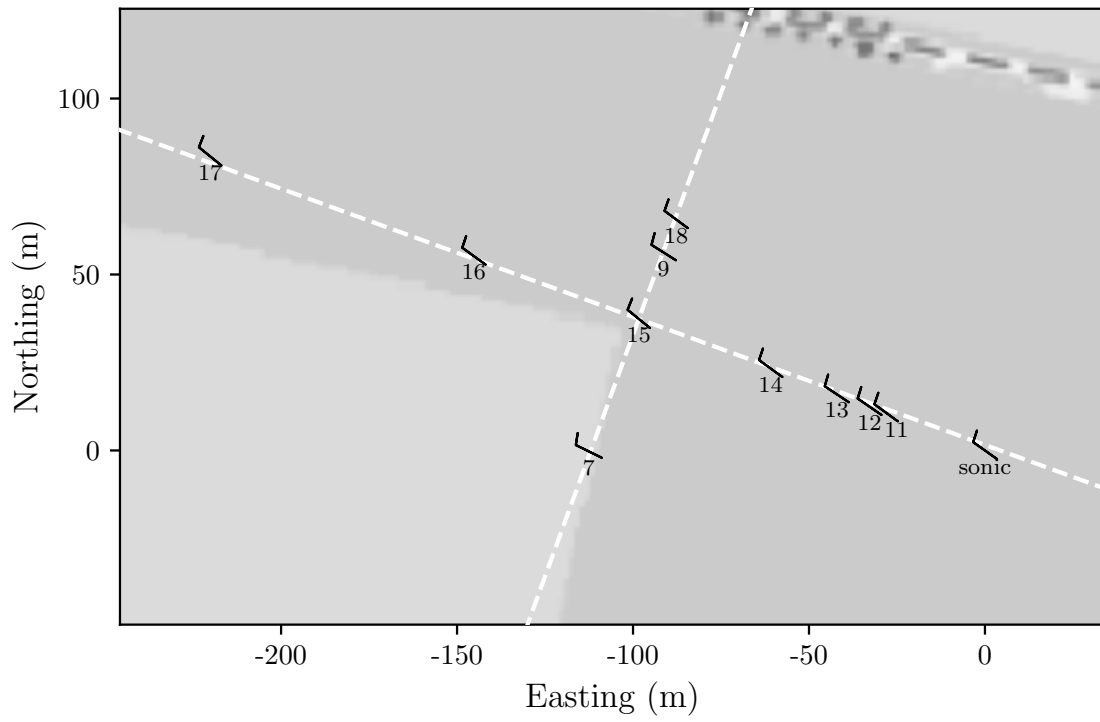
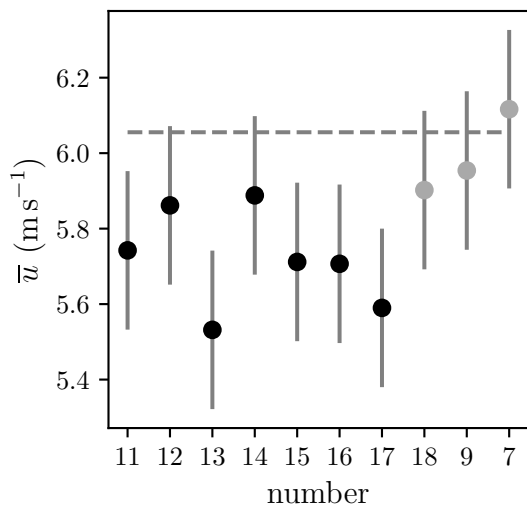


Figure B.1: Tower measurements of daily cycle of (a) surface fluxes, (b) turbulent kinetic energy at different heights, (c) potential temperature at various levels, (d) wind speed at several heights for the convective case on 2021-07-02. The surface fluxes and turbulent kinetic energy have been processed with an averaging time of 30 min, the temperature and wind speed values are 10 min averages. The time labels are at the end of the averaging interval. The green rectangle indicates the time of the horizontal flight pattern.

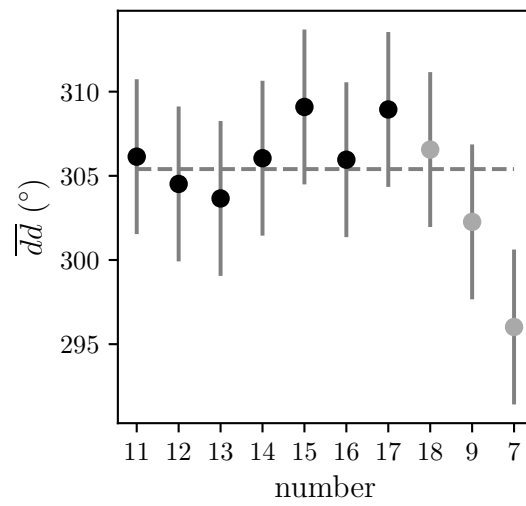
(a)



(b)



(c)



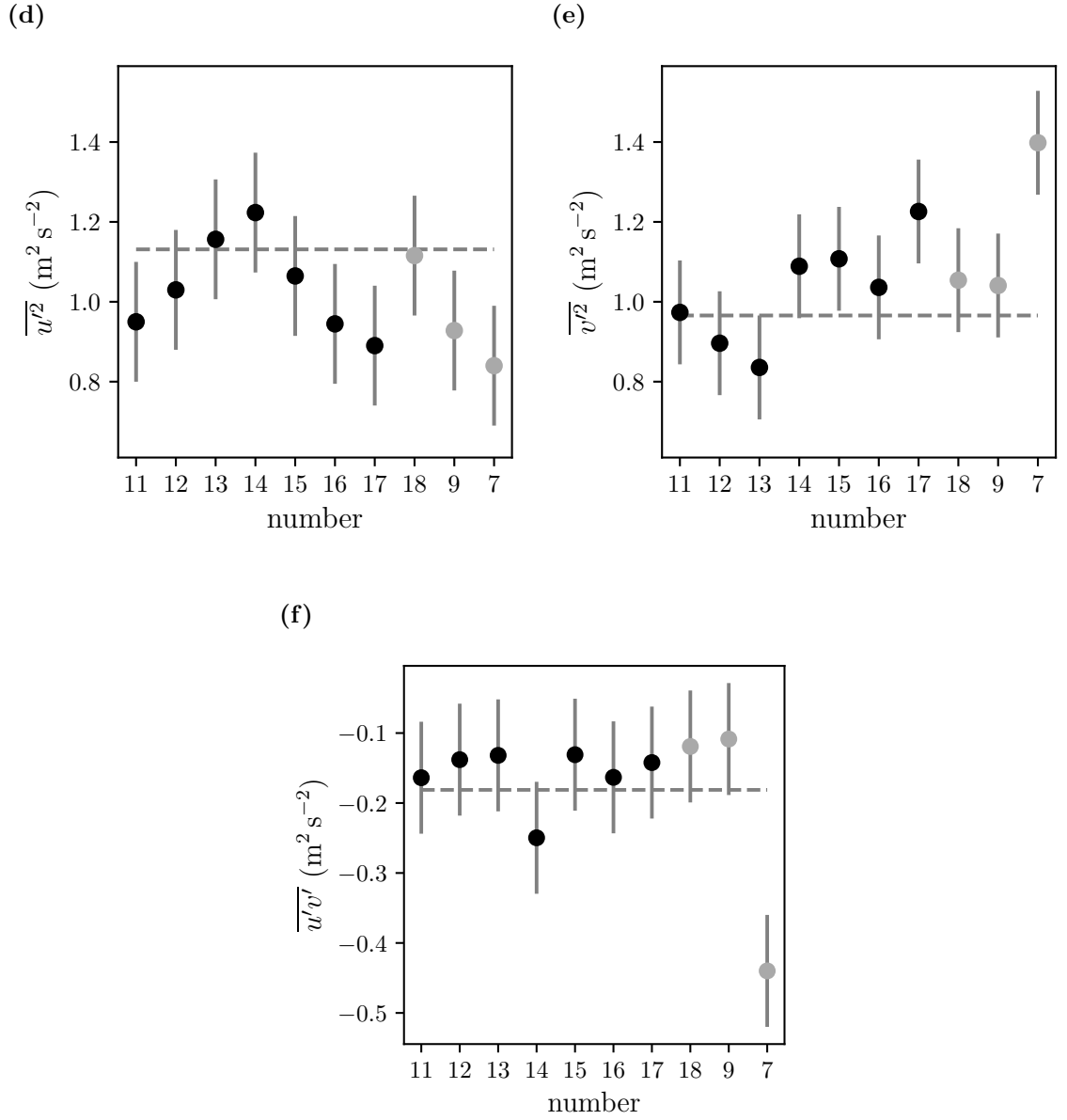


Figure B.2: (a) Horizontal pattern with wind barbs in knots and UAV labelling for the convective case on 2021-07-02. The light gray in the background indicates corn field and the dark gray grassland. Spatially distributed measurements of (b) mean wind speed, (c) mean wind direction, (d) variance of streamwise velocity, (e) variance of lateral velocity and (f) covariance of horizontal velocity components. Black dots are measurements of quadrotors in x -direction of the flight pattern and gray dots are measurements of quadrotors in y -direction. The gray dotted lines are sonic measurements. The root mean square errors after Table 4.1 are shown as error bars.

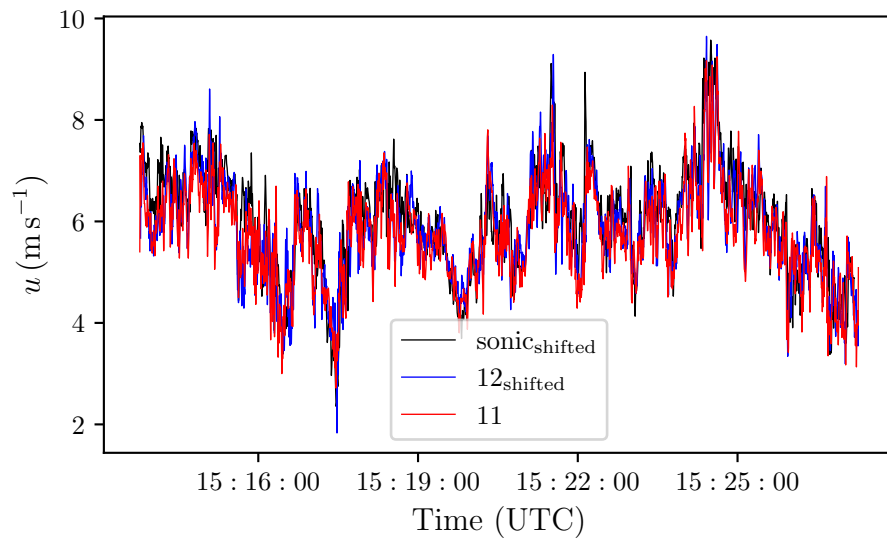
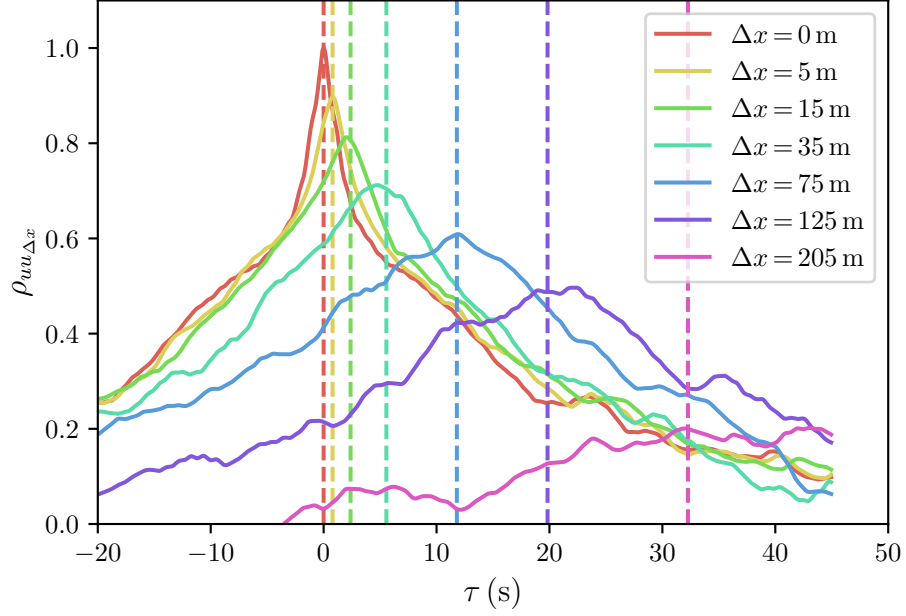


Figure B.3: Time series of streamwise velocity for the convective case on 2021-07-02. Shown are series for the sonic and the two nearest UAVs #11 and #12. The timeseries for the sonic and UAV #12 are shifted according to equation (3.19).

(a)



(b)

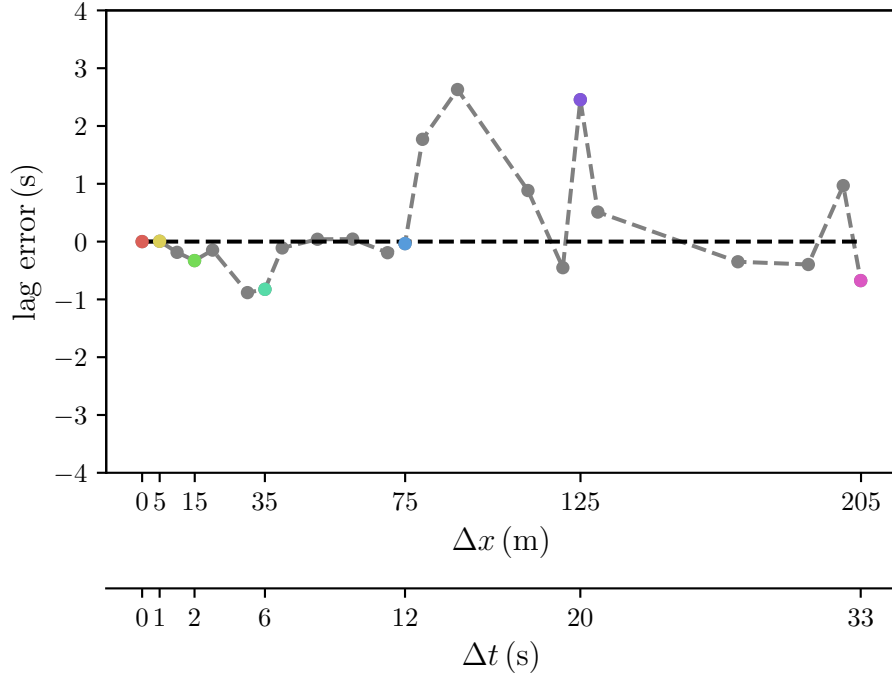
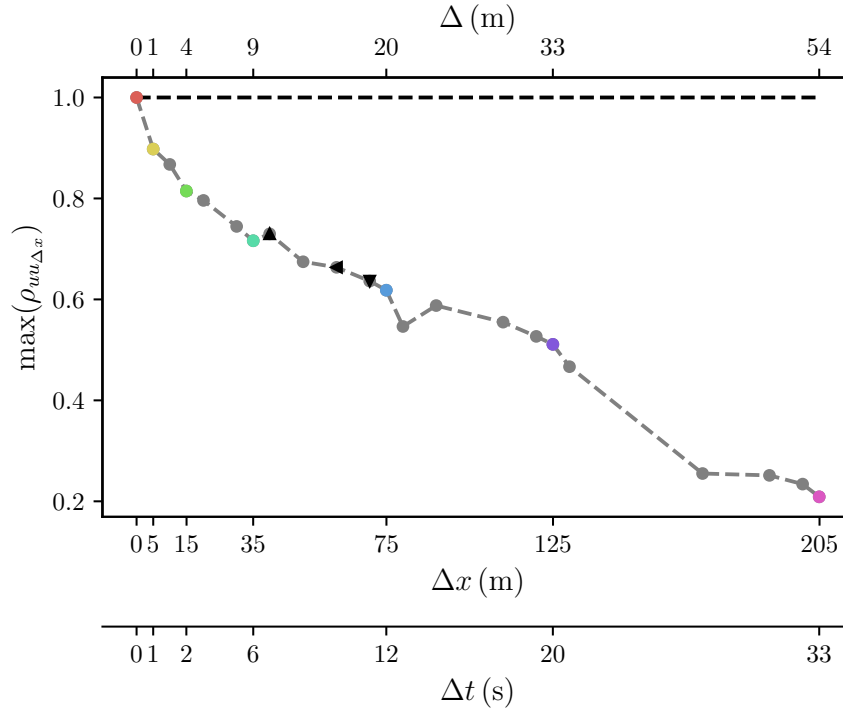


Figure B.4: (a) Cross-correlation function of streamwise velocity for different Δx as function of time lag τ for the convective case on 2021-07-02. Here, x is the fixed position of vehicle #11. The vertical lines show the theoretically expected locations of the peaks according to equation (3.19). (b) Difference between the locations of the maxima and the theoretical ones (lag error). In contrast to (a) x is not fixed, instead all possible combinations of the vehicles are shown, with the coloured dots matching the combinations in (a). A second axis has been added where the distances Δx have been converted to time differences Δt after equation (3.19).

(a)



(b)

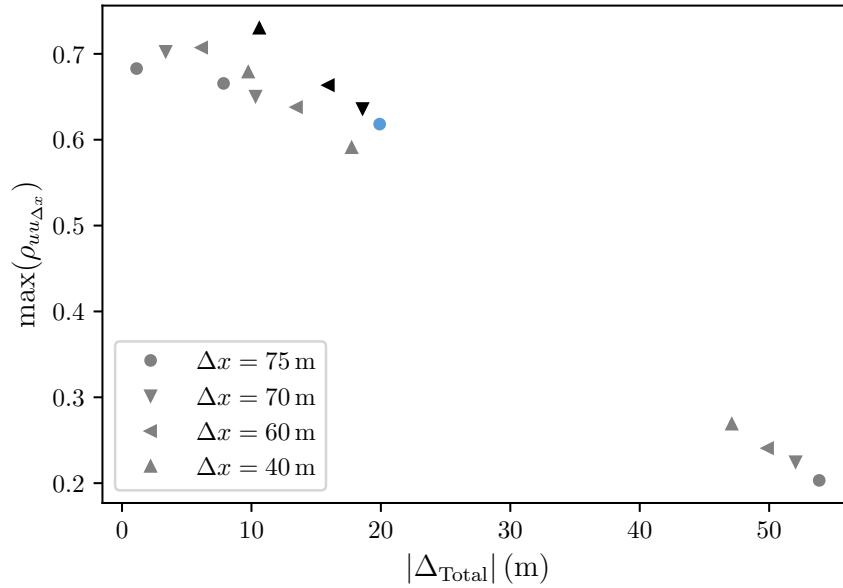


Figure B.5: (a) Maxima of cross-correlation function of streamwise velocity depending on distance Δx . In contrast to Figure B.4a, x is not fixed, instead all possible combinations of the vehicles in x -direction are considered. Coloured values correspond to the peaks in Figure B.4a. The axis on the top is the displacement after equation (3.18). A second axis has been added on the bottom where the distances Δx have been converted to time differences Δt after equation (3.19). (b) Maxima of cross-correlation functions as a function of total displacement (eq. (3.20)). For that, UAVs in x -direction has been combined with vehicles in y -direction. The values depicted with black triangles and the blue dot are also shown in (a).

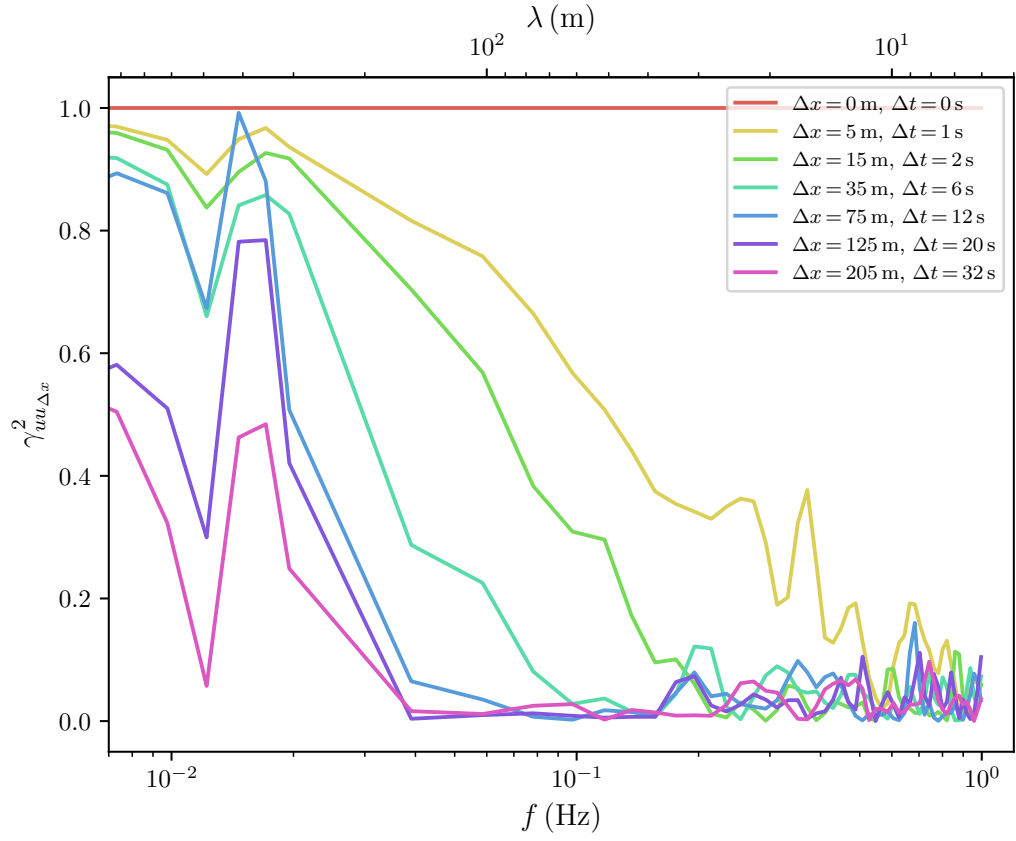
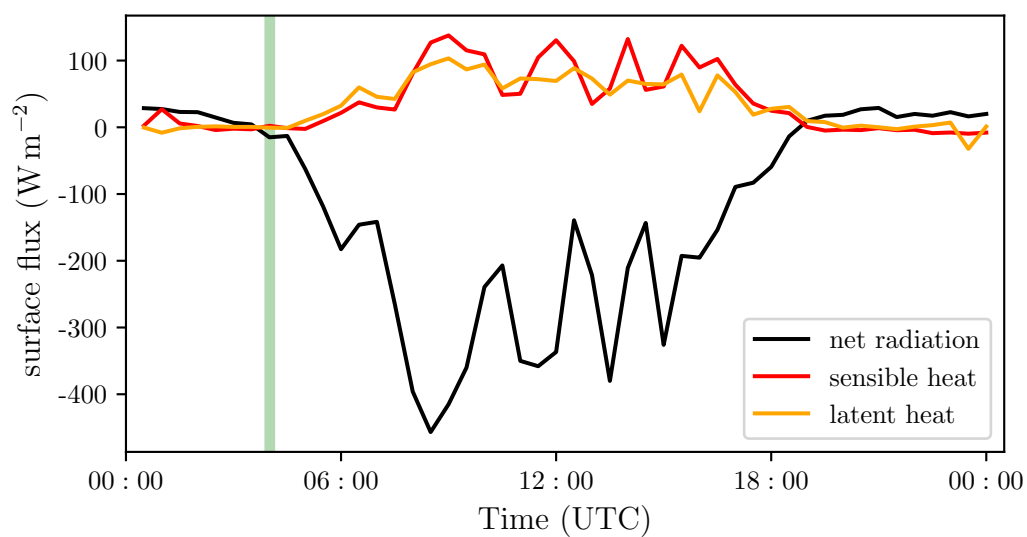


Figure B.6: Coherence of streamwise velocity for different spatial distances Δx or equivalent evolution time Δt (eq. (3.19)) for the convective case on 2021-07-02. Here, x is the fixed position of vehicle #11. Frequencies have been converted to wavelengths after equation (2.11) (top axis).

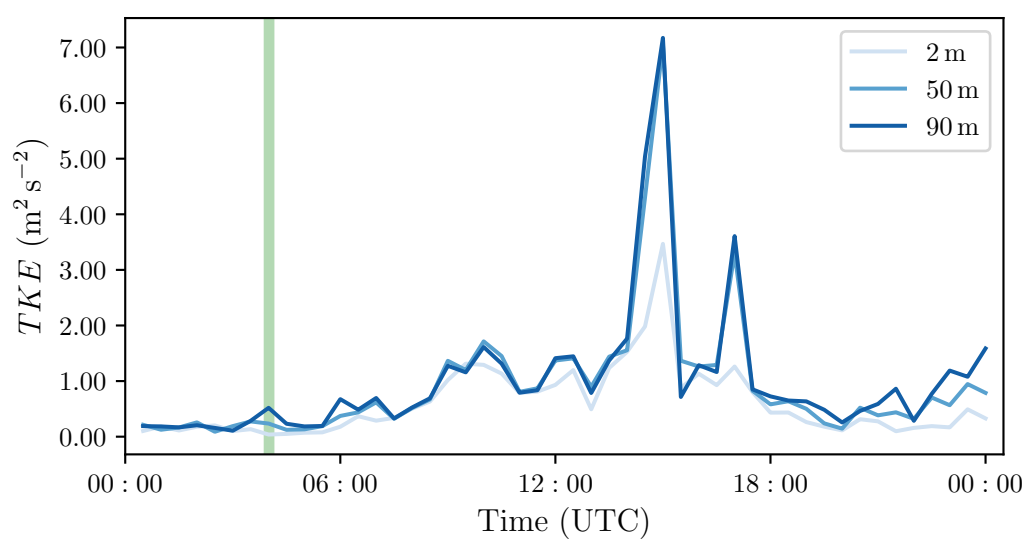
Appendix C

Stable

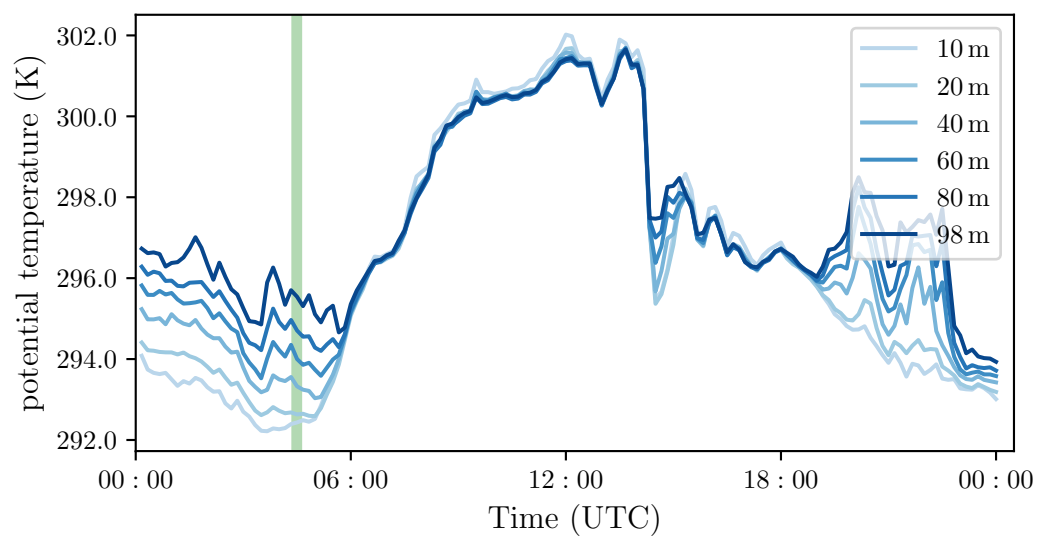
(a)



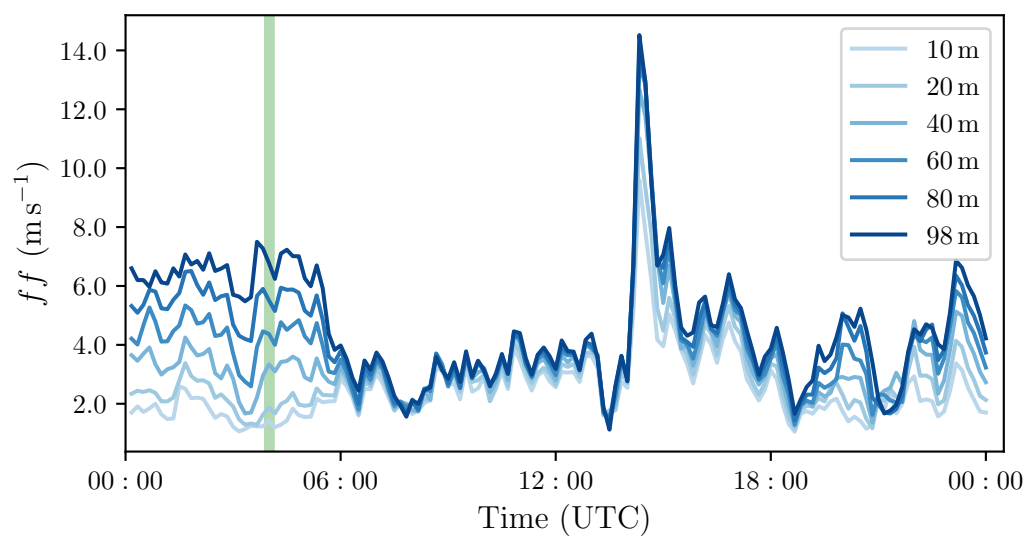
(b)



(c)



(d)



(e)

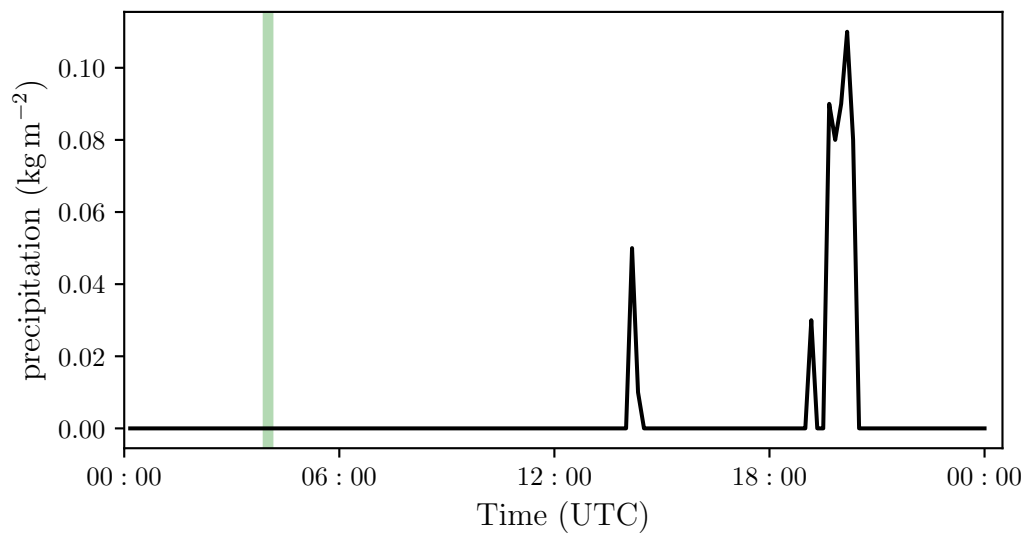
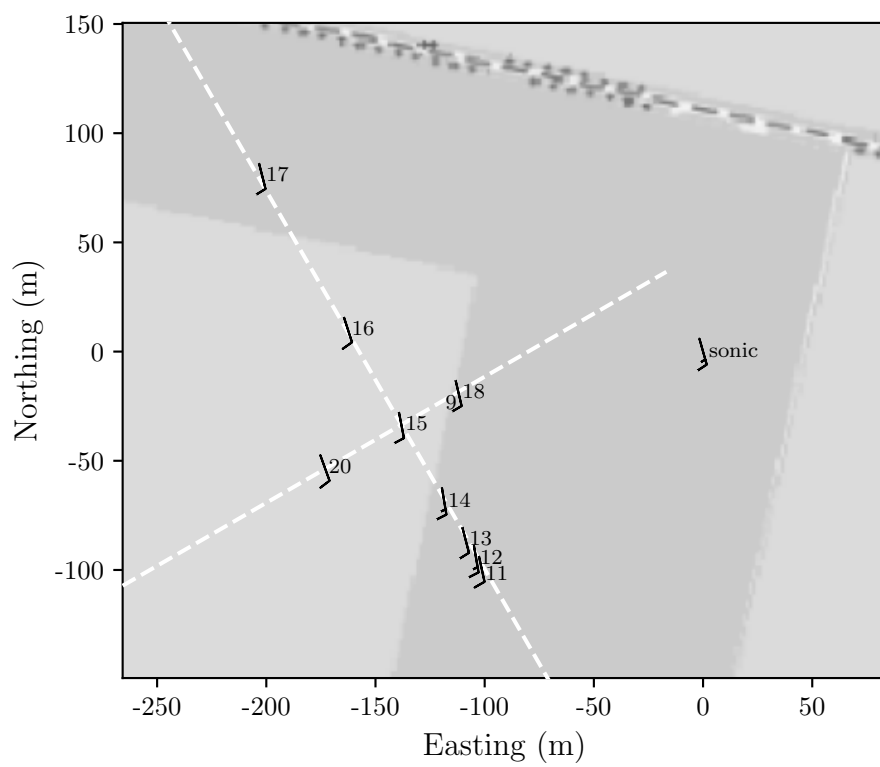
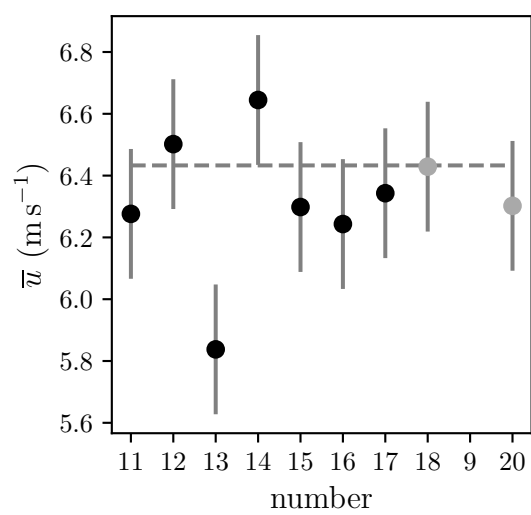


Figure C.1: Tower measurements of daily cycle of (a) surface fluxes, (b) turbulent kinetic energy at different heights, (c) potential temperature at various levels, (d) wind speed at several heights and (e) precipitation for the stable case on 2021-06-29. The surface fluxes and turbulent kinetic energy have been processed with an averaging time of 30 min, the temperature and wind speed values are 10 min averages, and the precipitation is the sum over 10 min. The time labels are at the end of the averaging interval. The green rectangle indicates the time of the horizontal flight pattern.

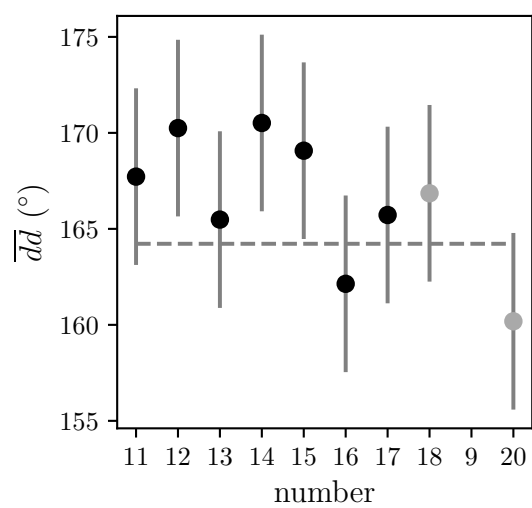
(a)



(b)



(c)



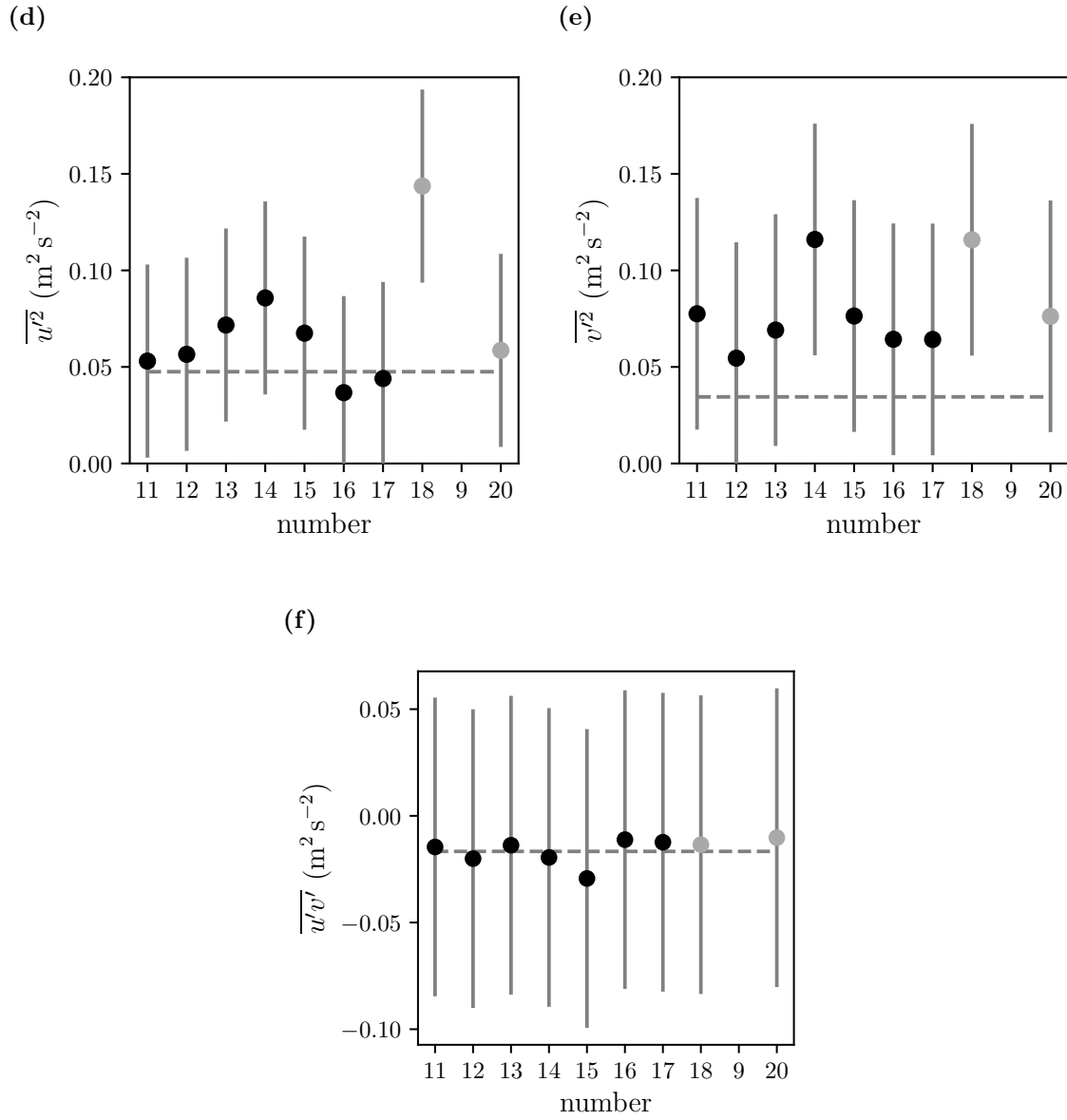


Figure C.2: (a) Horizontal pattern with wind barbs in knots and UAV labelling for the stable case on 2021-06-29. The light gray in the background indicates corn field and the dark gray grassland. Spatially distributed measurements of (b) mean wind speed, (c) mean wind direction, (d) variance of streamwise velocity, (e) variance of lateral velocity and (f) covariance of horizontal velocity components. Black dots are measurements of quadrotors in x -direction of the flight pattern and gray dots are measurements of quadrotors in y -direction. The gray dotted lines are sonic measurements. The shown error bars are the root mean square errors after Table 4.1 for the mean wind speed and direction and after Table 4.7 for the (co-)variances.

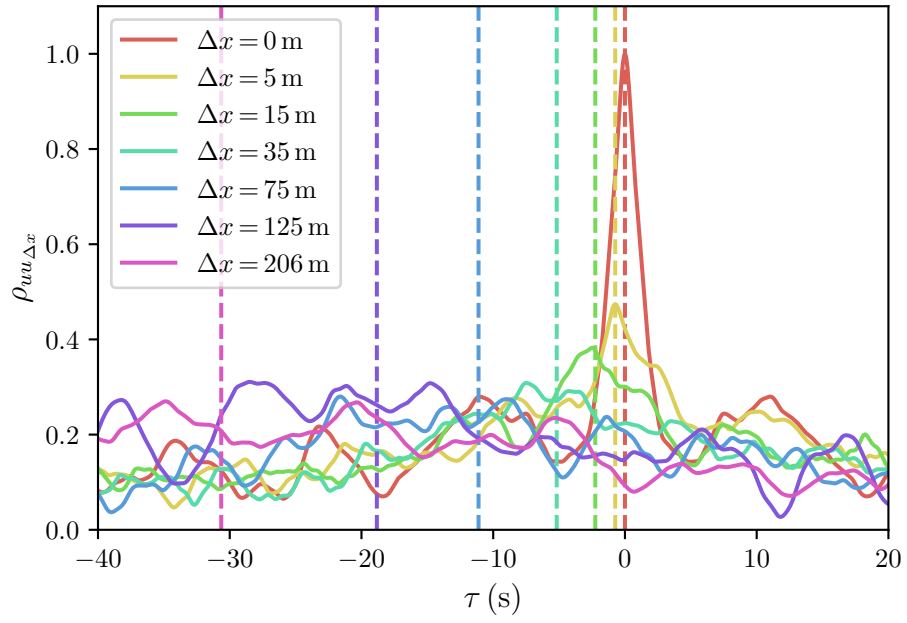
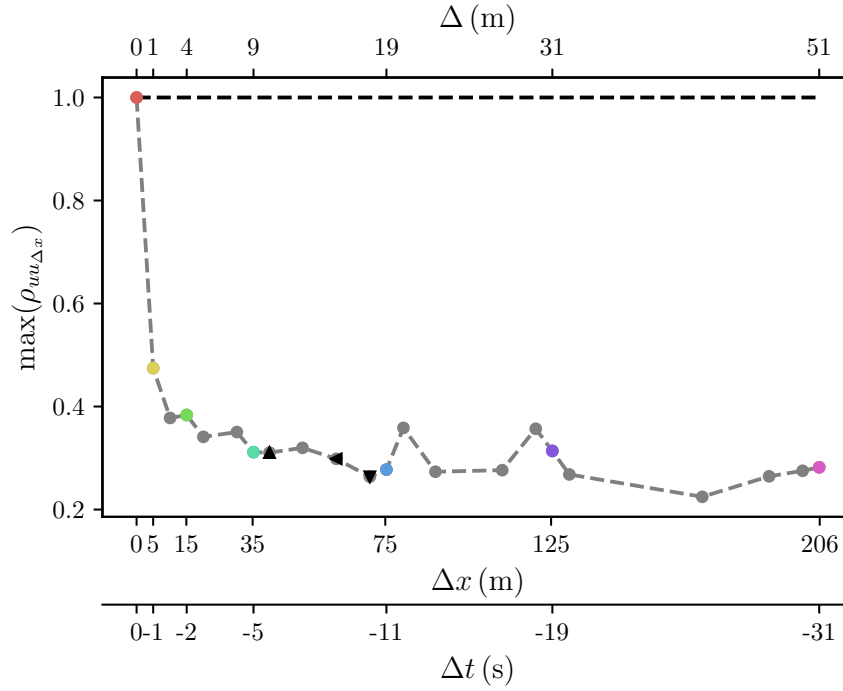


Figure C.3: Cross-correlation function of streamwise velocity for different Δx as function of time lag τ for the stable case on 2021-06-29. Here, x is the fixed position of vehicle #11. The vertical lines show the theoretically expected locations of the peaks according to equation (3.19).

(a)



(b)

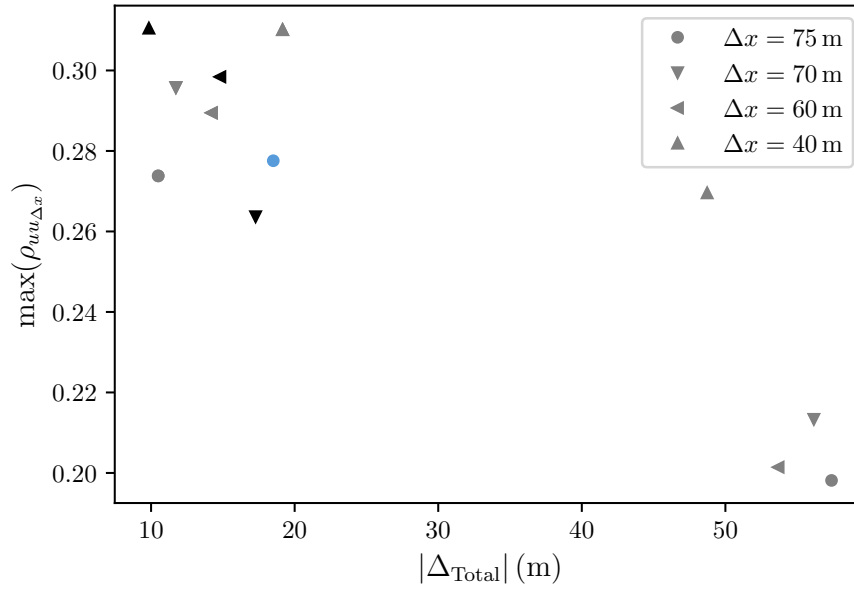


Figure C.4: (a) Maxima of cross-correlation function of streamwise velocity depending on distance Δx . In contrast to Figure C.3, x is not fixed, instead all possible combinations of the vehicles in x -direction are considered. Coloured values correspond to the maxima in Figure C.3 determined with the approach presented in section 4.4.4. The axis on the top is the displacement after equation (3.18). A second axis has been added on the bottom where the distances Δx have been converted to time differences Δt after equation (3.19). (b) Maxima of cross correlation functions as a function of total displacement (eq. (3.20)). For that, UAVs in x -direction has been combined with vehicles in y -direction. The values depicted with black triangles and the blue dot are also shown in (a).

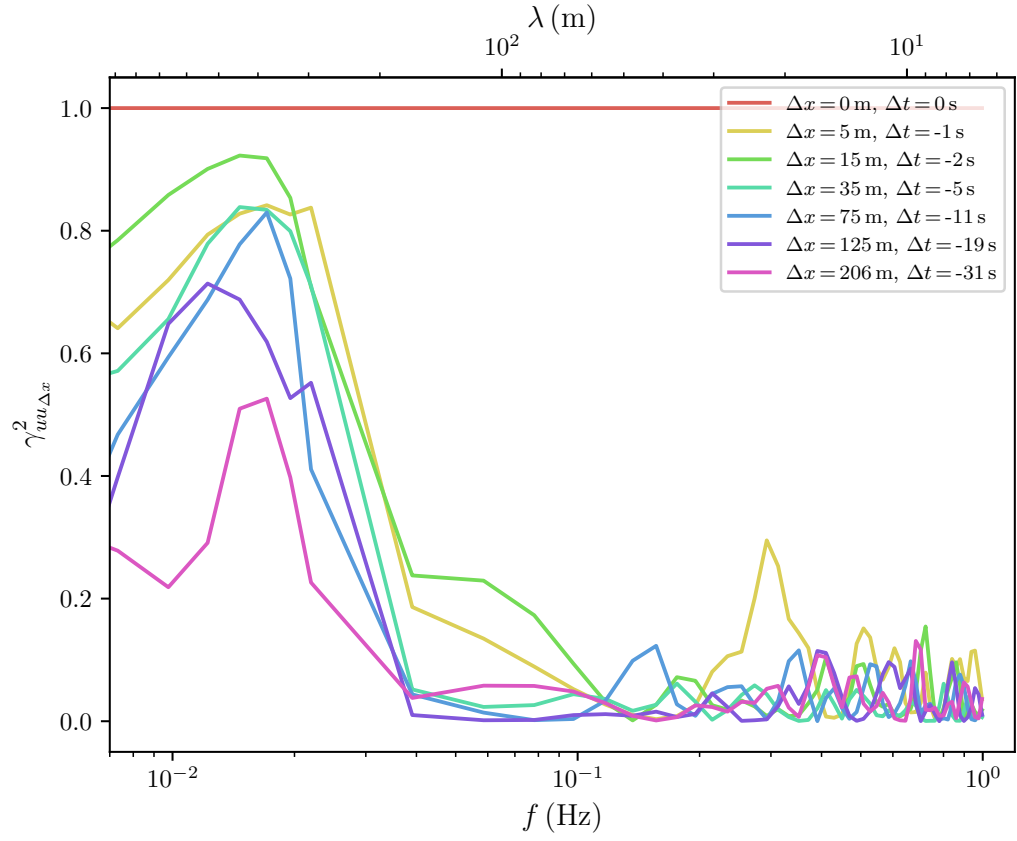


Figure C.5: Coherence of streamwise velocity for different spatial distances Δx or equivalent evolution time Δt (eq. (3.19)) for the stable case on 2021-06-29. Here, x is the fixed position of vehicle #11. Frequencies have been converted to wavelengths after equation (2.11) (top axis).

Bibliography

- Bahraminasab, A., M. D. Niray, J. Davoudi, M. R. R. Tabar, A. A. Masoudi, and K. R. Sreenivasan, 2008: Taylor’s frozen-flow hypothesis in burgers turbulence. *Physical Review E*, **77** (6), doi:10.1103/physreve.77.065302.
- Bell, T. M., B. R. Greene, P. M. Klein, M. Carney, and P. B. Chilson, 2020: Confronting the boundary layer data gap: evaluating new and existing methodologies of probing the lower atmosphere. *Atmospheric Measurement Techniques*, **13** (7), 3855–3872, doi:10.5194/amt-13-3855-2020.
- Beyrich, F., et al., 2002: Experimental determination of turbulent fluxes over the heterogeneous LITFASS area: Selected results from the LITFASS-98 experiment. *Theoretical and Applied Climatology*, **73** (1-2), 19–34, doi:10.1007/s00704-002-0691-7.
- Broisy, C., K. Krampf, M. Zeeman, B. Wolf, W. Junkermann, K. Schäfer, S. Emeis, and H. Kunstmann, 2017: Simultaneous multicopter-based air sampling and sensing of meteorological variables. *Atmospheric Measurement Techniques*, **10** (8), 2773–2784, doi:10.5194/amt-10-2773-2017.
- Cuxart, J., B. Wrenger, B. Matjacic, and L. Mahrt, 2019: Spatial variability of the lower atmospheric boundary layer over hilly terrain as observed with an RPAS. *Atmosphere*, **10** (11), 715, doi:10.3390/atmos10110715.
- Dosio, A., J. V. G. de Arellano, A. A. M. Holtslag, and P. J. H. Builtjes, 2005: Relating eulerian and lagrangian statistics for the turbulent dispersion in the atmospheric convective boundary layer. *Journal of the Atmospheric Sciences*, **62** (4), 1175–1191, doi:10.1175/jas3393.1.
- Foken, T., 2016: *Angewandte Meteorologie*. Springer Berlin Heidelberg, 420 pp.
- Foken, T. and B. Wichura, 1996: Tools for quality assessment of surface-based flux measurements. *Agricultural and Forest Meteorology*, **78** (1-2), 83–105, doi:10.1016/0168-1923(95)02248-1.

- Gagne, D., et al., 2020: mavlink/qgroundcontrol v4.0.9. Zenodo, doi:10.5281/ZENODO.3937530.
- Golzio, A., I. M. Bollati, and S. Ferrarese, 2019: An assessment of coordinate rotation methods in sonic anemometer measurements of turbulent fluxes over complex mountainous terrain. *Atmosphere*, **10** (6), 324, doi:10.3390/atmos10060324.
- Higgins, C. W., M. Froidevaux, V. Simeonov, N. Vercauteren, C. Barry, and M. B. Parlange, 2012: The effect of scale on the applicability of Taylor’s frozen turbulence hypothesis in the atmospheric boundary layer. *Boundary-Layer Meteorology*, **143** (2), 379–391, doi:10.1007/s10546-012-9701-1.
- Horst, T. W., J. Kleissl, D. H. Lenschow, C. Meneveau, C.-H. Moeng, M. B. Parlange, P. P. Sullivan, and J. C. Weil, 2004: HATS: Field observations to obtain spatially filtered turbulence fields from crosswind arrays of sonic anemometers in the atmospheric surface layer. *Journal of the Atmospheric Sciences*, **61** (13), 1566–1581, doi:10.1175/1520-0469(2004)061<1566:hfotos>2.0.co;2.
- Kljun, N., P. Calanca, M. W. Rotach, and H. P. Schmid, 2015: A simple two-dimensional parameterisation for flux footprint prediction (FFP). *Geoscientific Model Development*, **8** (11), 3695–3713, doi:10.5194/gmd-8-3695-2015.
- Kolmogorov, A. N., 1941b: The local structure of turbulence in incompressible viscous fluid for very large reynolds numbers. *Dokl. Akad. Nauk. SSSR*, **30**, 299–303.
- Kral, S. T., et al., 2021: The innovative strategies for observations in the arctic atmospheric boundary layer project (ISOBAR): Unique finescale observations under stable and very stable conditions. *Bulletin of the American Meteorological Society*, **102** (2), E218–E243, doi:10.1175/bams-d-19-0212.1.
- Krishnamurthy, R., R. Calhoun, B. Billings, and J. Doyle, 2011: Wind turbulence estimates in a valley by coherent doppler lidar. *Meteorological Applications*, **18** (3), 361–371, doi:10.1002/met.263.
- Lumley, J. L., 1965: Interpretation of time spectra measured in high-intensity shear flows. *Physics of Fluids*, **8** (6), 1056, doi:10.1063/1.1761355.
- Lumley, J. L. and H. A. Panofsky, 1964: *The Structure of Atmospheric Turbulence*. NewYork: Interscience., 239 pp.
- Margairaz, F., E. R. Pardyjak, and M. Calaf, 2020: Surface thermal heterogeneities and the atmospheric boundary layer: The relevance of dispersive fluxes. *Boundary-Layer Meteorology*, **175** (3), 369–395, doi:10.1007/s10546-020-00509-w.

- Markowski, P. and Y. Richardson, 2010: *Mesoscale Meteorology in Midlatitudes*. John Wiley & Sons, Ltd, 407 pp., doi:10.1002/9780470682104.
- Mauder, M., T. Foken, and J. Cuxart, 2020: Surface-energy-balance closure over land: A review. *Boundary-Layer Meteorology*, **177** (2-3), 395–426, doi:10.1007/s10546-020-00529-6.
- Molter, C. and P. W. Cheng, 2020: ANDroMeDA - a novel flying wind measurement system. *Journal of Physics: Conference Series*, **1618**, 32–49, doi:10.1088/1742-6596/1618/3/032049.
- Nolan, P., et al., 2018: Coordinated unmanned aircraft system (UAS) and ground-based weather measurements to predict lagrangian coherent structures (LCSs). *Sensors*, **18** (12), 4448, doi:10.3390/s18124448.
- O'Connor, E. J., A. J. Illingworth, I. M. Brooks, C. D. Westbrook, R. J. Hogan, F. Davies, and B. J. Brooks, 2010: A method for estimating the turbulent kinetic energy dissipation rate from a vertically pointing doppler lidar, and independent evaluation from balloon-borne in situ measurements. *Journal of Atmospheric and Oceanic Technology*, **27** (10), 1652–1664, doi:10.1175/2010jtecha1455.1.
- Palomaki, R. T., N. T. Rose, M. van den Bossche, T. J. Sherman, and S. F. J. D. Wekker, 2017: Wind estimation in the lower atmosphere using multirotor aircraft. *Journal of Atmospheric and Oceanic Technology*, **34** (5), 1183–1191, doi:10.1175/jtech-d-16-0177.1.
- Panofsky, H. A. and T. Mizuno, 1975: Horizontal coherence and pasquill's beta. *Boundary-Layer Meteorology*, **9** (3), 247–256, doi:10.1007/bf00230769.
- Pielke, R. A. and H. A. Panofsky, 1970: Turbulence characteristics along several towers. *Boundary-Layer Meteorology*, **1** (2), 115–130, doi:10.1007/bf00185733.
- Platis, A., A. F. Moene, D. M. Villagrasa, F. Beyrich, D. Tupman, and J. Bange, 2017: Observations of the temperature and humidity structure parameter over heterogeneous terrain by airborne measurements during the LITFASS-2003 campaign. *Boundary-Layer Meteorology*, **165** (3), 447–473, doi:10.1007/s10546-017-0290-x.
- Pope, S. B., 2000: *Turbulent Flows*. Cambridge University Press, 806 pp.
- Reuter, M., et al., 2020: Development of a small unmanned aircraft system to derive CO2 emissions of anthropogenic point sources. doi:10.5194/amt-2020-234.

- Reynolds, O., 1895: IV. on the dynamical theory of incompressible viscous fluids and the determination of the criterion. *Philosophical Transactions of the Royal Society of London. (A.)*, **186**, 123–164, doi:10.1098/rsta.1895.0004.
- Richardson, L. F., 1922: *Weather prediction by numerical process*. Cambridge University Press, 236 pp.
- Schlez, W. and D. Infield, 1998: Horizontal, two point coherence for separations greater than the measurement height. *Boundary-Layer Meteorology*, **87** (3), 459–480, doi:10.1023/a:1000997610233.
- Schlipf, D., et al., 2011: Testing of frozen turbulence hypothesis for wind turbine applications with a scanning lidar system. Universität Stuttgart, doi:10.18419/OPUS-3915.
- Shimura, T., M. Inoue, H. Tsujimoto, K. Sasaki, and M. Iguchi, 2018: Estimation of wind vector profile using a hexarotor unmanned aerial vehicle and its application to meteorological observation up to 1000 m above surface. *Journal of Atmospheric and Oceanic Technology*, **35** (8), 1621–1631, doi:10.1175/jtech-d-17-0186.1.
- Smalikho, I. N. and V. A. Banakh, 2017: Measurements of wind turbulence parameters by a conically scanning coherent doppler lidar in the atmospheric boundary layer. *Atmospheric Measurement Techniques*, **10** (11), 4191–4208, doi:10.5194/amt-10-4191-2017.
- Stull, R., 2017: *Practical Meteorology: An Algebra-based Survey of Atmospheric Science*. Univ. of British Columbia, 940 pp.
- Stull, R. B., 1988: *An Introduction to Boundary Layer Meteorology*. Springer Netherlands, 688 pp.
- Taylor, G. I., 1938: The spectrum of turbulence. *Proceedings of the Royal Society A: Mathematical, Physical and Engineering Sciences*, **164** (919), 476–490, doi:10.1098/rspa.1938.0032.
- Thielicke, W., W. Hübert, and U. Müller, 2020: Towards accurate and practical drone-based wind measurements with an ultrasonic anemometer. doi:10.5194/amt-2020-258.
- Wang, J.-Y., B. Luo, M. Zeng, and Q.-H. Meng, 2018: A wind estimation method with an unmanned rotorcraft for environmental monitoring tasks. *Sensors*, **18** (12), 4504, doi:10.3390/s18124504.

- Welch, P., 1967: The use of fast fourier transform for the estimation of power spectra: A method based on time averaging over short, modified periodograms. *IEEE Transactions on Audio and Electroacoustics*, **15** (2), 70–73, doi:10.1109/tau.1967.1161901.
- Wetz, T. and N. Wildmann, 2022: Spatially distributed and simultaneous wind measurements with a fleet of small quadrotor UAS. **In preparation.**
- Wetz, T., N. Wildmann, and F. Beyrich, 2021: Distributed wind measurements with multiple quadrotor unmanned aerial vehicles in the atmospheric boundary layer. *Atmospheric Measurement Techniques*, **14** (5), 3795–3814, doi:10.5194/amt-14-3795-2021.
- Wildmann, N., N. Bodini, J. K. Lundquist, L. Bariteau, and J. Wagner, 2019: Estimation of turbulence dissipation rate from doppler wind lidars and in situ instrumentation for the Perdigão 2017 campaign. *Atmospheric Measurement Techniques*, **12** (12), 6401–6423, doi:10.5194/amt-12-6401-2019.
- Wildmann, N., G. A. Rau, and J. Bange, 2015: Observations of the early morning boundary-layer transition with small remotely-piloted aircraft. *Boundary-Layer Meteorology*, **157** (3), 345–373, doi:10.1007/s10546-015-0059-z.
- Wildmann, N., N. Vasiljevic, and T. Gerz, 2018: Wind turbine wake measurements with automatically adjusting scanning trajectories in a multi-doppler lidar setup. *Atmospheric Measurement Techniques*, **11** (6), 3801–3814, doi:10.5194/amt-11-3801-2018.
- Willis, G. E. and J. W. Deardorff, 1976: On the use of Taylor’s translation hypothesis for diffusion in the mixed layer. *Quarterly Journal of the Royal Meteorological Society*, **102** (434), 817–822, doi:10.1002/qj.49710243411.
- Wyngaard, J. C., 2009: *Turbulence in the Atmosphere*. Cambridge University Press, doi:10.1017/cbo9780511840524.
- Wyngaard, J. C. and S. F. Clifford, 1977: Taylor’s hypothesis and high-frequency turbulence spectra. *Journal of the Atmospheric Sciences*, **34** (6), 922–929, doi:10.1175/1520-0469(1977)034<0922:thahts>2.0.co;2.

Acknowledgments

First of all, I would like to thank my two colleagues Norman Wildmann and Tamino Wetz from DLR Oberpfaffenhofen for the excellent teamwork in the project SWUF-3D. Thank you very much for all the advices and help regarding the thesis. Many thanks also for the nice conversations away from work.

Further, I would like to thank May Bohmann for her support during the field campaign.

I would also like to thank my supervisor Manuela Lehner for the helpful conversations and discussions during the regular online sessions. Her ideas and suggestions have enriched the work immensely.

Many thanks to DWD-Lindenberg Observatory for providing the necessary reference data.

Eidesstattliche Erklärung

Ich erkläre hiermit an Eides statt durch meine eigenhändige Unterschrift, dass ich die vorliegende Arbeit selbständig verfasst und keine anderen als die angegebenen Quellen und Hilfsmittel verwendet habe. Alle Stellen, die wörtlich oder inhaltlich den angegebenen Quellen entnommen wurden, sind als solche kenntlich gemacht.

Die vorliegende Arbeit wurde bisher in gleicher oder ähnlicher Form noch nicht als Magister-/Master-/Diplomarbeit/Dissertation eingereicht.

Datum

Unterschrift